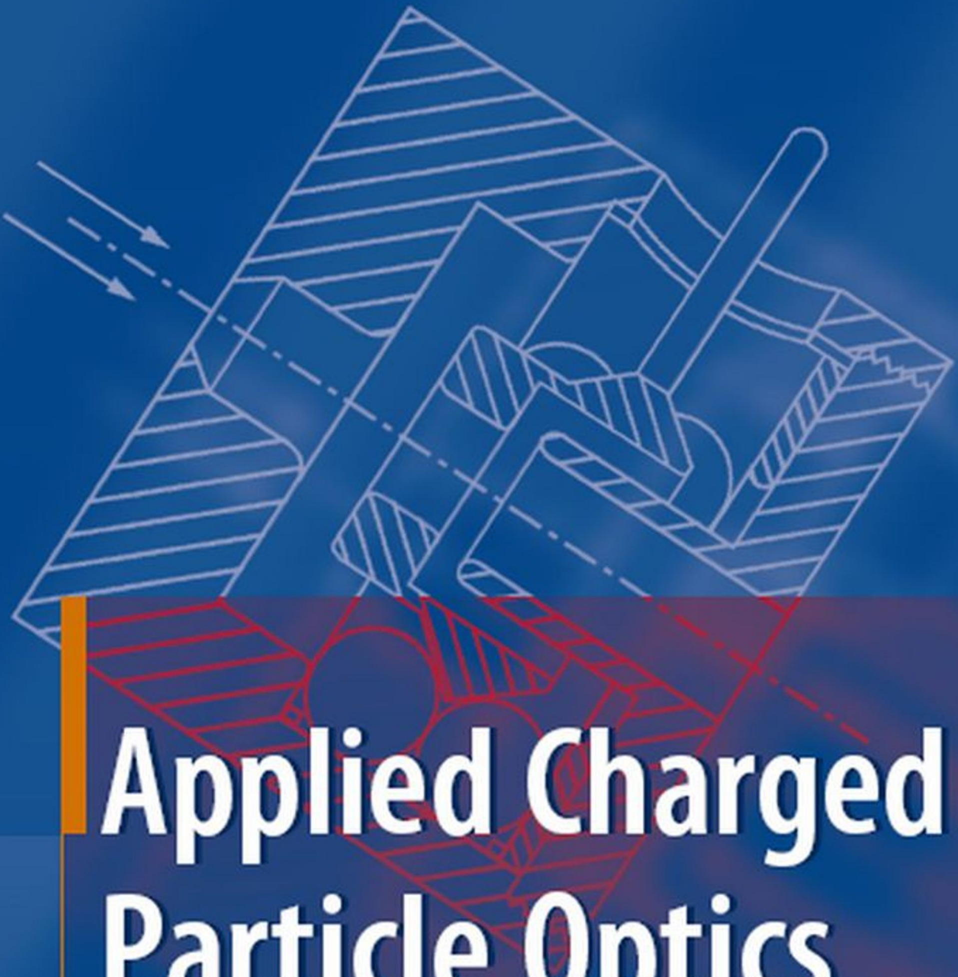

Applied Charged Particle Optics

Helmut Liebl

Springer

Applied Charged Particle Optics

Helmut Liebl

Applied Charged Particle Optics

With 124 Figures

Springer

Dr. Helmut Liebl
Hartstr. 17
85386 Eching
Germany

Library of Congress Control Number: 2007932728

ISBN 978-3-540-71924-3 Springer Berlin Heidelberg New York

Springer is a part of Springer Science+Business Media.

springer.com

Typesetting: Data prepared by the Author and by SPI Kolam
Cover: eStudio Calamar Steinen

Printed on acid-free paper SPIN 11903109 57/3180/SPI 5 4 3 2 1 0

To my dear wife Elfie,
and our children
Bernhard, Wolfgang, Regina, Christina, Martin,
and our grandchildren.

Preface

This booklet is essentially an extended English version of a course I taught at the Max Planck Institute for Plasma Physics in Garching/ Munich for physicists and graduate students working at the Institute and for the nearby Physics Department of the Technical University.

It covers mostly applications of particle optics which I have designed, built and worked with myself during my career, such as mass spectrometry, focusing of ion beams, emission microscopy, ion and electron beam systems, in an energy range of less than 20 keV.

It is intended to help physicists who have to design their own apparatus or to help them to better understand instruments they have to work with.

Some of the subjects described date back quite some time, the oldest references as far back as the thirties in the last century. And I am old enough to have met some of those authors personally. But the booklet also contains some material from my own file which has not been published previously.

I should like to thank Dr. Dietmar Wagner for his invaluable help with the manuscript.

Eching, August 2007 *Helmut Liebl*

Contents

1

Lenses: Basic Optics

Summary. Basic optical formulae are derived, the transfer matrix method is explained, the lens action of apertures is shown, and emission, immersion and einzel lenses are treated.

A lens is characterized by the property that it imparts to a ray (particle trajectory) passing through it a deflection ($\Delta r'$) which is proportional to the distance r_1 from the axis, at which the ray passes, but which is independent of the original slope r'_1. For thin lenses this deflection may be assumed to be a sharp kink, occurring at the single principal plane P. If the entrance side – left of P – is designated by the index 1, and the exit side – right of P – by the index 2, one can write that the exit distance r_2 equals the entrance distance r_1 (Fig. 1.1):

$$r_1 = r_2 \ , \tag{1.1}$$

and the exit slope r'_2 equals the entrance slope r'_1 plus the (negative) change of slope $\Delta r'$:

$$r'_2 = r'_1 + \Delta r' \ . \tag{1.2}$$

As stated above, $-\Delta r' = c r_1$, where c is the proportionality constant. It can be derived from the special case that the exit ray is parallel to the axis:

$$r'_2 = 0, \qquad r'_1 = -\Delta r' = c r_1, \tag{1.3}$$

$$c = \frac{-\Delta r'}{r_1} = \frac{1}{f_1}. \tag{1.4}$$

In this case (Fig. 1.2) the entrance ray crosses the axis at the distance f_1 from P; f_1 is the entrance focal length of the lens, F_1 the entrance focal plane. Equation (1.2) can now be written as

$$r'_2 = r'_1 - \frac{r_1}{f_1}. \tag{1.5}$$

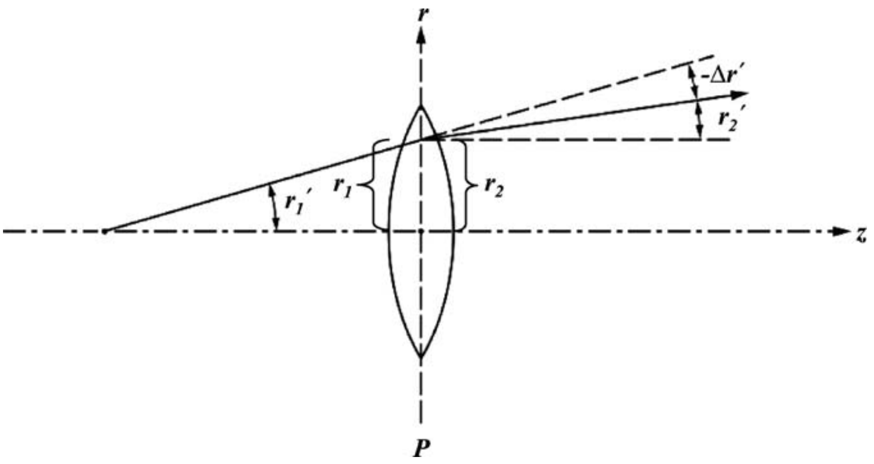

Fig. 1.1. Principle of a lens: A trajectory crossing the lens at distance r_1 from the z-axis is deflected by an angle $\Delta r'$ which is proportional to r_1

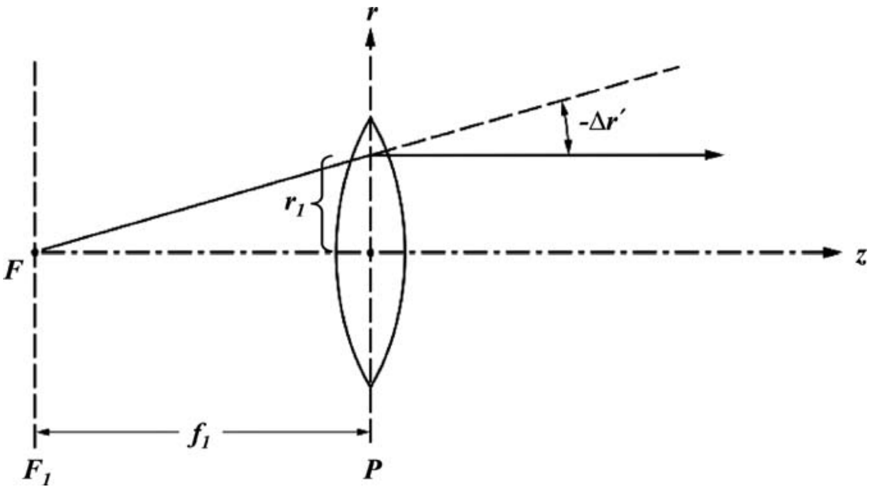

Fig. 1.2. Trajectories starting from the axis point F – the focal point – leave the lens parallel to the z-axis. The distance of the focal plane F_1 to the lens plane P is the focal length f_1

Equations (1.1) and (1.5) can be written in matrix form

$$\begin{pmatrix} r \\ r' \end{pmatrix}_2 = \begin{pmatrix} 1 & 0 \\ -\frac{1}{f_1} & 1 \end{pmatrix} \begin{pmatrix} r \\ r' \end{pmatrix}_1 = M_{\mathrm{L}} \begin{pmatrix} r \\ r' \end{pmatrix}_1 , \tag{1.6}$$

M_L is called the transfer matrix of the lens.

The transfer matrix is

$$M_{\mathrm{L}} = \begin{pmatrix} a_{11} & a_{12} \\ a_{21} & a_{22} \end{pmatrix}$$

with the coefficients

$$\begin{aligned} a_{11} &= 1, \\ a_{12} &= 0, \\ a_{21} &= -1/f_1, \\ a_{22} &= 1. \end{aligned}$$

In explicit form one has

$$\begin{aligned} r_2 &= a_{11} r_1 + a_{12} r_1', \\ r_2' &= a_{21} r_1 + a_{22} r_1'. \end{aligned}$$

This, with the above coefficients for a lens, yields (1.1) and (1.5).

Another way of describing the action of a lens is in the form of the exit equation of the ray in the z–r coordinate system (Fig. 1.3):

$$r = a r_1' + z r_2' = a r_1' + z \left(r_1' - \frac{r_1}{f_1} \right),$$

where a is the distance of the object point A from P. With $r_1 = a r_1'$ we have

$$r = \left[a + z \left(1 - \frac{a}{f_1} \right) \right] r_1'. \tag{1.7}$$

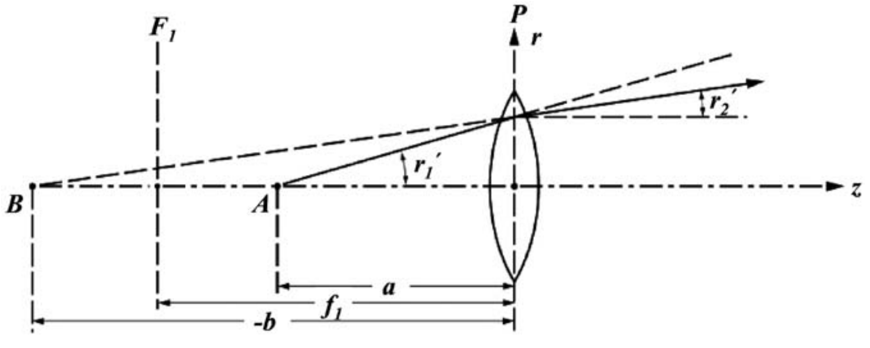

Fig. 1.3. The object point A is imaged to a virtual image point B if $a < f_1$

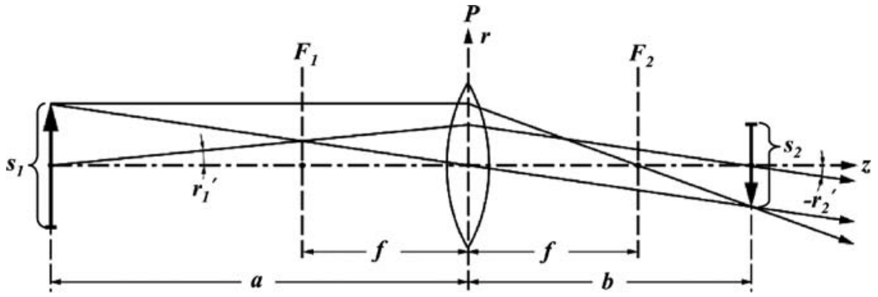

Fig. 1.4. Imaging of an extended object through a lens to a real image

The distance of the image point B – the point where the exit ray crosses the axis – from P, i.e. the image distance b, is obtained from (1.7) with $r = 0$:

$$a + b\left(1 - \frac{a}{f_1}\right) = 0.$$

By dividing it by ab, this yields the familiar lens equation

$$\frac{1}{a} + \frac{1}{b} = \frac{1}{f_1}. \tag{1.8}$$

For $a < f_1$, as in Fig. 1.3, the image distance b is negative, i.e. the image is virtual.

For lenses, where the particle energy is the same on both the entrance and exit side, the focal lengths are also the same on both sides:

$$f_2 = f_1 = f. \tag{1.9}$$

For the imaging of an extended object (Fig. 1.4) the same rules apply as in light optics:

$$\text{lateral magnification: } M = \frac{s_2}{s_1} = \frac{b}{a}, \tag{1.10}$$

$$\text{angular magnification: } \frac{r_2'}{r_1'} = \frac{1}{M}. \tag{1.11}$$

Electrostatic lenses are generally thick lenses which have two principal planes P_1 and P_2, and these are usually interchanged as shown in Fig. 1.5.

1.1 Simple Transfer Matrices

The transfer matrix of a lens has been introduced above. Transfer matrices become very useful when composite optical systems consisting

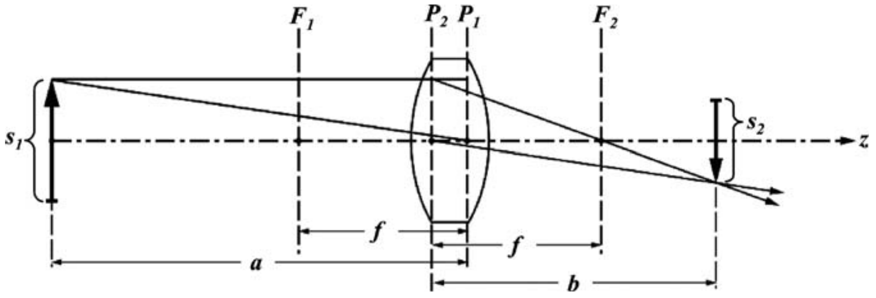

Fig. 1.5. Schematic of electrostatic lens with interchanged principal planes P_1 and P_2

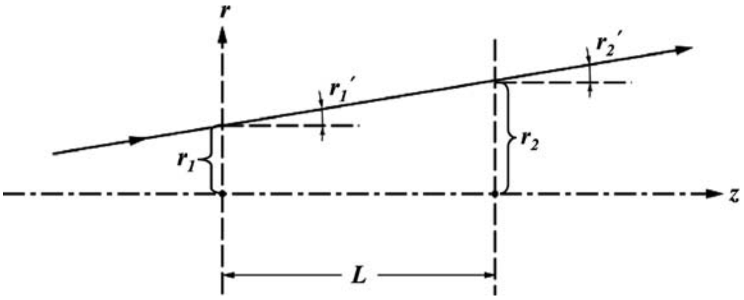

Fig. 1.6. Drift space without deflection

of several elements in tandem are to be treated. Frequently, just one property of the composite system is of interest, e.g. the magnification, and therefore only one of the matrix coefficients needs to be calculated, which can often be done very quickly with the aid of a hand calculator. The simplest transfer matrix is that of a drift space (Fig. 1.6).

From the figure one can see immediately that

$$r_2 = r_1 + L\,r_1', \tag{1.12}$$

$$r_2' = r_1', \tag{1.13}$$

or in transfer matrix form

$$\begin{pmatrix} r \\ r' \end{pmatrix}_2 = \begin{pmatrix} 1 & L \\ 0 & 1 \end{pmatrix} \begin{pmatrix} r \\ r' \end{pmatrix}_1 = M_{\mathrm{D}} \begin{pmatrix} r \\ r' \end{pmatrix}_1 . \tag{1.14}$$

When two optical elements are combined in tandem, their respective transfer matrices have to be multiplied. For the combination of a lens

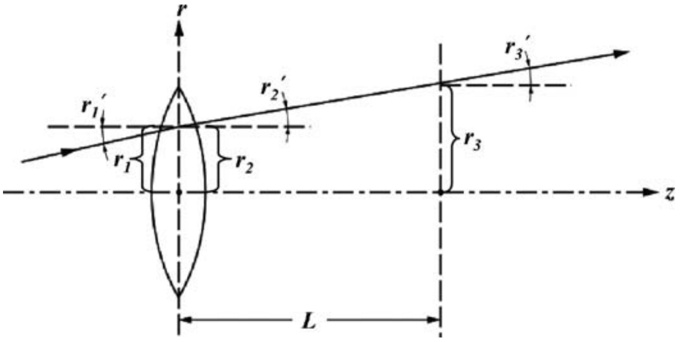

Fig. 1.7. Combination of einzel lens with drift space

and a drift space (Fig. 1.7) one has therefore to multiply the transfer matrices of the lens and the drift space:

$$\begin{pmatrix} r \\ r' \end{pmatrix}_3 = \underbrace{\begin{pmatrix} b_{11} & b_{12} \\ b_{21} & b_{22} \end{pmatrix}}_{\text{drift space}} \begin{pmatrix} r \\ r' \end{pmatrix}_2 = \underbrace{\begin{pmatrix} b_{11} & b_{12} \\ b_{21} & b_{22} \end{pmatrix}}_{\text{drift space}} \underbrace{\begin{pmatrix} a_{11} & a_{12} \\ a_{21} & a_{22} \end{pmatrix}}_{\text{lens}} \begin{pmatrix} r \\ r' \end{pmatrix}_1 ,$$

$$\begin{pmatrix} r \\ r' \end{pmatrix}_3 = \begin{pmatrix} c_{11} & c_{12} \\ c_{21} & c_{22} \end{pmatrix} \begin{pmatrix} r \\ r' \end{pmatrix}_1 . \tag{1.15}$$

The coefficients c_{ik} are found according to the scheme

$$c_{ik} = \sum_{s=1}^{2} b_{is} a_{sk}, \qquad i, k = 1, 2,$$

or explicitely

$$\begin{aligned} c_{11} &= b_{11}a_{11} + b_{12}a_{21}, \\ c_{12} &= b_{11}a_{12} + b_{12}a_{22}, \\ c_{21} &= b_{21}a_{11} + b_{22}a_{21}, \\ c_{22} &= b_{21}a_{12} + b_{22}a_{22}. \end{aligned}$$

In our example, we have with (1.14),

$$\begin{aligned} b_{11} &= 1, \quad b_{12} = L, \\ b_{21} &= 0, \quad b_{22} = 1. \end{aligned}$$

With these and the coefficients of the lens transfer matrix, one then obtains

$$c_{11} = 1 - \frac{L}{f}, \quad c_{12} = L,$$
$$c_{21} = -\frac{1}{f}, \quad c_{22} = 1.$$

Explicitly, this reads

$$r_2 = r_1 + L\left(r_1' - \frac{r_1}{f}\right),$$
$$r_2' = r_1' - \frac{r_1}{f}.$$

When the sequence of the two elements is reversed, i.e. drift space followed by lens, the $a_{ik}s$ and $b_{ik}s$ are interchanged. This yields

$$\begin{aligned}
c^*_{11} &= a_{11}b_{11} + a_{12}b_{21},\\
c^*_{12} &= a_{11}b_{12} + a_{12}b_{22},\\
c^*_{21} &= a_{21}b_{11} + a_{22}b_{21},\\
c^*_{22} &= a_{21}b_{12} + a_{22}b_{22},\\
c^*_{11} &= 1, \qquad c^*_{12} = L,\\
c^*_{21} &= -\frac{1}{f}, \qquad c^*_{22} = 1 - \frac{L}{f}.
\end{aligned}$$

1.2 Passage of Charged Particles Through a Uniform Electrostatic Field

Figure 1.8 shows the important case where a charged particle is accelerated through a uniform field between the equipotential planes denoted P_1 and P_2. The spaces to the left of P_1 and right of P_2 are field free and have the potentials V_1 and V_2. The potentials are counted from where the charged particles have zero energy so that their kinetic energy in flight direction at any point in space with the potential V_i is eV_i.

In this simple case the differential equations of motion can be straightforwardly integrated and yield the motion of the particle in the z–r-coordinate system as a function of time t:

$$m\ddot{r} = 0, \quad m\ddot{z} = eE, \quad z_1 = r_1 = 0,$$
$$\dot{z}_1 = v_1 \cos\alpha_1, \quad \dot{r}_1 = v_1 \sin\alpha_1, \; v_1 = \sqrt{2e\frac{V_1}{m}}$$

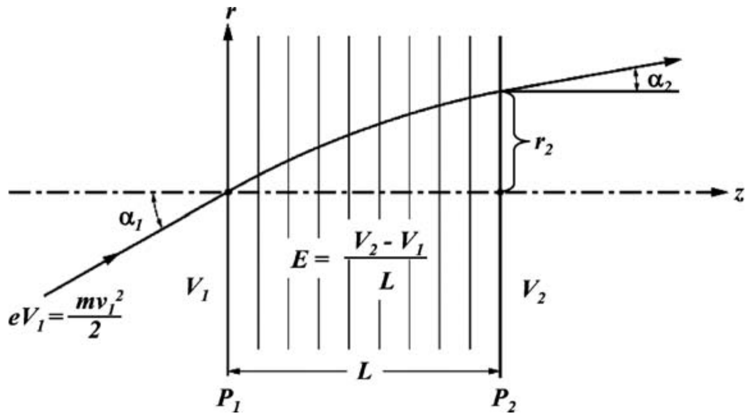

Fig. 1.8. Acceleration of charged particle through a uniform field

(v_1 is the velocity of the particle at energy eV_1, m its mass).

$$\dot{z} = \frac{eE}{m}t + v_1 \cos\alpha_1, \quad z = \frac{eE}{2m}t^2 + v_1 \cos\alpha_1 \cdot t, \tag{1.16}$$

$$\dot{r} = \dot{r}_1 = v_1 \sin\alpha_1, \quad r = v_1 \sin\alpha_1 \cdot t. \tag{1.17}$$

By eliminating the time t one obtains the trajectory:

$$\frac{eE}{2mv_1}t^2 + \cos\alpha_1 \cdot t - \frac{z}{v_1} = 0,$$

$$t = \frac{mv_1}{eE}\left(\sqrt{\cos^2\alpha_1 + \frac{2eE}{mv_1^2}z} - \cos\alpha_1\right),$$

$$r = \frac{2V_1}{E}\sin\alpha_1\left(\sqrt{\frac{E}{V_1}z + \cos^2\alpha_1} - \cos\alpha_1\right). \tag{1.18}$$

This is the equation of the trajectory within the field. At the end of the field where $z = L$, the distance from the z-axis is obtained with

$$\frac{E}{V_1} = \frac{1}{L}\left(\frac{V_2}{V_1} - 1\right)$$

as

$$r_2 = \frac{2L\sin\alpha_1}{\frac{V_2}{V_1} - 1}\left(\sqrt{\frac{V_2}{V_1} - \sin^2\alpha_1} - \cos\alpha_1\right) \tag{1.19}$$

The slope of the trajectory at P_2 is found by differentiating (1.18) with respect to z and setting $z = L$:

$$
\begin{aligned}
r' = \frac{\mathrm{d}r}{\mathrm{d}z} &= \sin\alpha_1 \left(\frac{E}{V_1} z + \cos^2\alpha_1\right)^{-1/2} \\
r_2' &= \sin\alpha_1 \left(\frac{V_2}{V_1} - \sin^2\alpha_1\right)^{-1/2} . \qquad (1.20)
\end{aligned}
$$

From (1.20) the refractive index for charged particles can be derived: rewriting r_2' one obtains

$$
r_2' = \tan\alpha_2 = \frac{\sin\alpha_2}{\sqrt{1-\sin^2\alpha_2}},
$$

and putting this into (1.20) yields

$$
\begin{aligned}
&\frac{\sin\alpha_2}{\sqrt{1-\sin^2\alpha_2}} = \frac{\sin\alpha_1}{\sqrt{\frac{V_2}{V_1}-\sin^2\alpha_1}}, \\
&\frac{V_2}{V_1} - \sin^2\alpha_1 = \frac{\sin^2\alpha_1}{\sin^2\alpha_2}\left(1-\sin^2\alpha_2\right) = \frac{\sin^2\alpha_1}{\sin^2\alpha_2} - \sin^2\alpha_1,
\end{aligned}
$$

and finally

$$
\frac{\sin\alpha_2}{\sin\alpha_1} = \sqrt{\frac{V_1}{V_2}}. \qquad (1.21)
$$

Note that the distance L does not appear in (1.21).

If one could compress the field to an infinitely narrow double-layer with the potentials V_1 and V_2 on either side, one would have the exact analogue to the refraction of light at the interface between two media with the refractive indices n_1 and n_2 (Fig. 1.9), where the familiar law of refraction is valid. Comparing this with (1.21) reveals that in electrostatic optics the square root of the potential plays the role of the refractive index n, the difference being that in light optics sharp interfaces are the rule, while in particle optics one has gradual transitions of the refractive index. (An example in light optics would be radially graded fibers in fiber optics.) Another difference of practical significance is that in electrostatic optics the particle energy and with its square root the refractive index can vary over many orders of magnitude, while the variation of the refractive index of transparent substances stays within half an order of magnitude.

The above equations are valid not only for acceleration ($V_2 > V_1$), but also for deceleration ($V_2 < V_1$). In the latter case, the expression

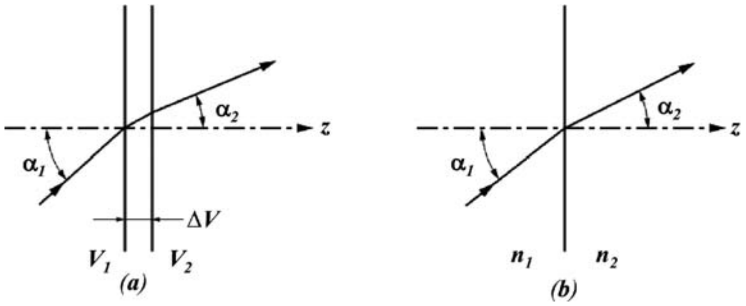

Fig. 1.9. Refraction of charged particle trajectories (**a**) compared to that of light (**b**)

under the square root of (1.19) and (1.20) may become negative, when $V_2/V_1 < \sin^2\alpha_1$, and the exit ordinate r_2 becomes imaginary. The physical meaning of this is that the particle does not reach the exit plane P_2 but is reflected before it. This case can be treated by expressing the abscissa z of the flying particle as a function of the ordinate r; i.e. by reversing (1.18).

One can obtain this directly by substituting the time t in (1.16) by t from (1.17). The result is

$$z = \frac{E}{4V_1}\frac{r^2}{\sin^2\alpha_1} + \frac{r}{\tan\alpha_1}. \tag{1.22}$$

This is the equation of the parabolic trajectory shown in Fig. 1.10 of the particle reflected in the decelerating field. Differentiating this equation with respect to r yields the slope against the r-ordinate:

$$\frac{\mathrm{d}z}{\mathrm{d}r} = \frac{E}{2V_1}\frac{r}{\sin^2\alpha_1} + \frac{1}{\tan\alpha_1}. \tag{1.23}$$

The turning point of the parabola $(z_{\mathrm{max}}, r_{\mathrm{m}})$ is found by setting (1.23) equal to zero:

$$r_{\mathrm{m}} = -2\frac{V_1}{E}\sin\alpha_1\cos\alpha_1, \tag{1.24}$$

$$z_{\mathrm{max}} = \frac{E}{4V_1}\frac{r_{\mathrm{m}}^2}{\sin^2\alpha_1} + \frac{r_{\mathrm{m}}}{\tan\alpha_1} = -\frac{V_1}{E}\cos^2\alpha_1. \tag{1.25}$$

(The minus sign of these expressions is cancelled by the negative E, see Fig. 1.10.)

For symmetry reasons, the distance of the point where the particle leaves the field again is $2r_{\mathrm{m}}$ apart from the point of entrance.

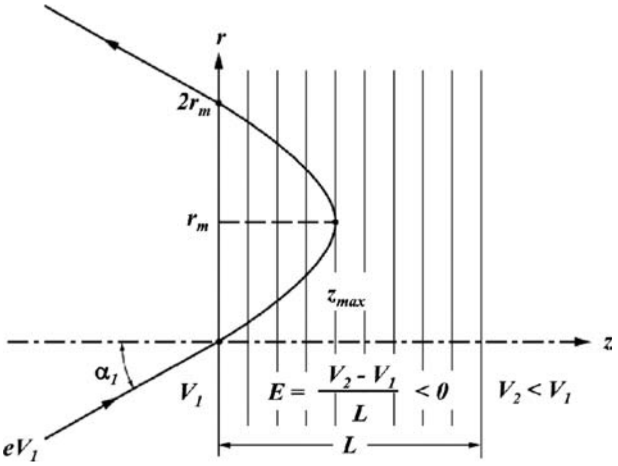

Fig. 1.10. Reflection of charged particle by a decelerating field

In the special case $\alpha_1 = 45°$ one obtains

$$r_\mathrm{m} = -\frac{V_1}{E}, \quad z_\mathrm{max} = -\frac{V_1}{2E} = \frac{r_\mathrm{m}}{2}.$$

The point of exit in this case is four times z_max apart from the point of entrance ($2r_\mathrm{m} = 4z_\mathrm{max}$).

It so happens that in this special case, $\alpha_1 = 45°, r_\mathrm{m}$ and therefore $2r_\mathrm{m}$ have a maximum. This is derived easily by differentiating r_m with respect to α_1 and setting the result equal to zero:

$$\frac{\partial r_\mathrm{m}}{\partial \alpha_1} = -2\frac{V_1}{E}\left(\cos^2\alpha_1 - \sin^2\alpha_1\right) = 0, \quad \alpha_1 = 45°.$$

This means also that the trajectories which have slightly different entrance angle variations $\Delta\alpha_1$ around $\alpha_1 = 45°$ (Fig. 1.11) cross each other and the trajectory with $\alpha_1 = 45°$ at the distance $2r_\mathrm{m}$. In other words, the retarding field has focusing properties.

It forms a first-order image of the entrance point at the exit point. This happens of course only two-dimensionally, viz. in the drawing plane. The abscissa of the turning point is found by differentiating z_max, (1.25), with respect to α_1:

$$\frac{\partial z_\mathrm{max}}{\partial \alpha_1} = 2\frac{V_1}{E}\sin\alpha_1\cos\alpha_1, \text{ and with } \alpha_1 = 45°, \Delta z_\mathrm{max} = \frac{V_1}{E}\Delta\alpha_1.$$

Another property of the electrostatic field can be demonstrated here, i.e. energy dispersion. When r_m is differentiated with respect to the

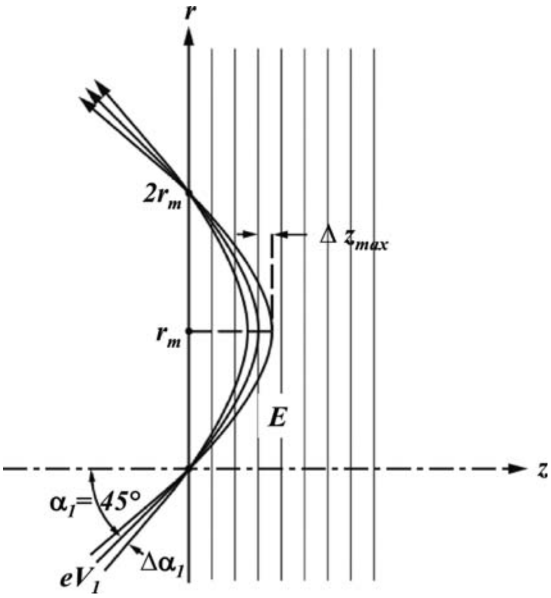

Fig. 1.11. Focusing properties of decelerating field

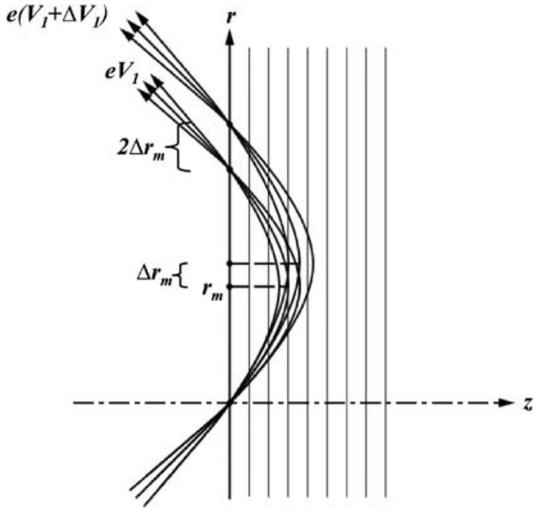

Fig. 1.12. Energy dispersion of decelerating field

particle energy eV_1 one obtains from (1.24) (Fig. 1.12)

$$\frac{\partial r_{\mathrm{m}}}{\partial V_1} = -\frac{2}{E}\sin\alpha_1\cos\alpha_1,\ \text{and with}\ \alpha_1 = 45^\circ,\ 2\Delta r_{\mathrm{m}} = -\frac{2}{E}\Delta V_1. \tag{1.26}$$

The variation of $z_{\max}$ is found by differentiating it with respect to V_1 (1.25):

$$\frac{\partial z_{\max}}{\partial V_1} = -\frac{\cos^2\alpha_1}{E}, \text{ and with } \alpha_1 = 45^\circ, \Delta z_{\max} = -\frac{1}{2E}\Delta V_1 = \frac{\Delta r_{\mathrm{m}}}{2}.$$

The uniform electrostatic field is a simple yet instructive example to demonstrate the focusing and dispersive properties of an electrostatic field, which can be derived in a few lines from first principles. In the examples to follow the derivation will not be presented but was found by the same means.

1.3 Transfer Matrix of the Uniform Field

Equations (1.19) and (1.20) represent a rigorous description of the trajectory's exit ordinate and slope after passage through a uniform field. When considering the paraxial case ($\alpha_1 \ll 1$, Fig. 1.13) one obtains the simpler expressions, with $\sin\alpha_1 \approx r_1', \cos\alpha_1 \approx 1, r_1' \ll V_2/V_1$,

$$r_2 \approx \frac{2Lr_1'}{\frac{V_2}{V_1} - 1}\left(\sqrt{\frac{V_2}{V_1}} - 1\right) = \frac{2L}{\sqrt{\frac{V_2}{V_1}} + 1} r_1', \tag{1.27}$$

$$r_2' \approx \sqrt{\frac{V_1}{V_2}} r_1', \tag{1.28}$$

In the general case, with $r_1 \neq 0$, one has therefore

$$r_2 = r_1 + \frac{2L}{\sqrt{\frac{V_2}{V_1}} + 1} r_1',$$

$$r_2' = \sqrt{\frac{V_1}{V_2}} r_1',$$

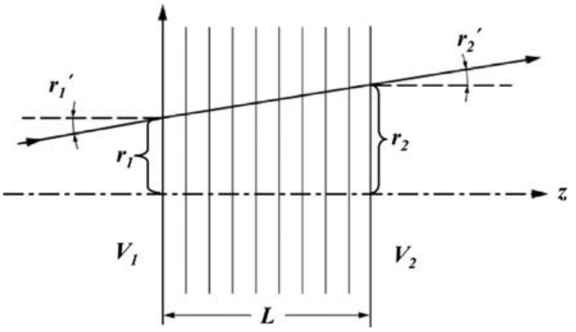

Fig. 1.13. Paraxial case of acceleration of charged particle through a uniform field

or in matrix form

$$\begin{pmatrix} r \\ r' \end{pmatrix}_2 = \begin{pmatrix} 1 & \frac{2L}{\sqrt{V_1/V_2}+1} \\ 0 & \sqrt{V_1/V_2} \end{pmatrix} \begin{pmatrix} r \\ r' \end{pmatrix}_1 = M_F \begin{pmatrix} r \\ r' \end{pmatrix}_1 .$$

The transfer matrix coefficients of the uniform electrostatic field are thus

$$a_{11} = 1, \qquad a_{12} = \frac{2L}{1 + \sqrt{\frac{V_2}{V_1}}},$$

$$a_{21} = 0, \qquad a_{22} = \sqrt{\frac{V_1}{V_2}}.$$

This is valid not only for acceleration ($V_2/V_1 > 1$), but also for deceleration ($V_2/V_1 < 1$). For the case of mere drift ($V_2/V_1 = 1$) the matrix coefficients for a drift space (1.14) result.

1.4 Acceleration of Charged Particles Emitted from a Planar Surface

A special case of practical importance is the acceleration of charged particles emitted or reflected from a planar conducting surface (Fig. 1.14).

When a charged particle leaves the surface with energy eV_1 and is accelerated by the voltage V_a it will leave the uniform acceleration field with energy $e(V_1 + V_\mathrm{a})$. With this definition, (1.19) and (1.20) now read, since $V_2 = V_1 + V_\mathrm{a}$,

$$r_2 = 2L\frac{V_1}{V_\mathrm{a}}\sin\alpha_1 \left(\sqrt{\frac{V_\mathrm{a}}{V_1} + \cos^2\alpha_1} - \cos\alpha_1 \right), \tag{1.29}$$

$$r_2' = \sin\alpha_1 \left(\frac{V_\mathrm{a}}{V_1} + \cos^2\alpha_1 \right)^{-1/2} . \tag{1.30}$$

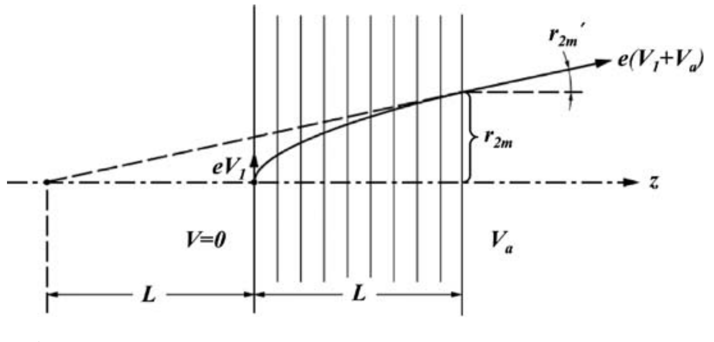

Fig. 1.14. Acceleration of charged particles emitted from planar conducting surface

For particles leaving the surface at a glancing angle ($\alpha_1 = 90°$) the maximum values of r_2 and r_2' are obtained:

$$r_{2\mathrm{m}} = 2L\sqrt{\frac{V_1}{V_\mathrm{a}}}, \tag{1.31}$$

$$r'_{2\mathrm{m}} = \sqrt{\frac{V_1}{V_\mathrm{a}}}. \tag{1.32}$$

The virtual starting point of these particles is located at the distance $r_{2\mathrm{m}}/r'_{2\mathrm{m}} = 2L$ behind the end of the uniform field, i.e. at the distance L behind the surface. This holds exactly for any positive value of V_1/V_a.

In most practical cases the acceleration voltage V_a is large in comparison to the starting voltage V_1. With this condition (1.29) and (1.30) become

$$r_2 \approx 2L\sqrt{\frac{V_1}{V_\mathrm{a}}}\sin\alpha_1, \tag{1.33}$$

$$r_2' \approx \sqrt{\frac{V_1}{V_\mathrm{a}}}\sin\alpha_1. \tag{1.34}$$

The virtual starting point is found as above by forming r_2/r_2'. Since α_1 cancels out, the virtual starting point is now also located at the distance L behind the surface for any starting angle, but only in first approximation for $V_\mathrm{a} \gg V_1$ (Fig. 1.15).

After the acceleration the trajectories are paraxial ($r_2' \ll 1$). An extended emitting surface element of dimension D_1 is imaged to a virtual surface element of dimension $D_2 = D_1$, i.e. the magnification is unity.

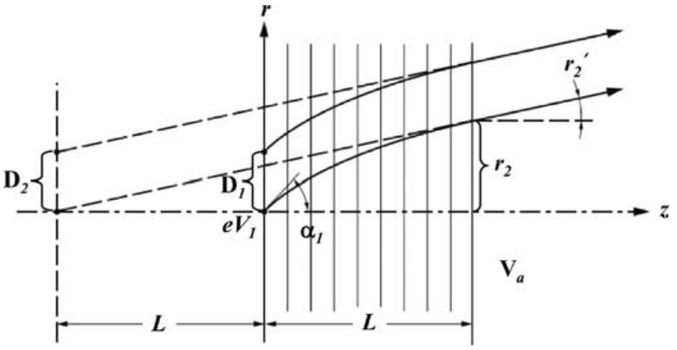

Fig. 1.15. Virtual imaging of surface emitting charged particles by accelerating field

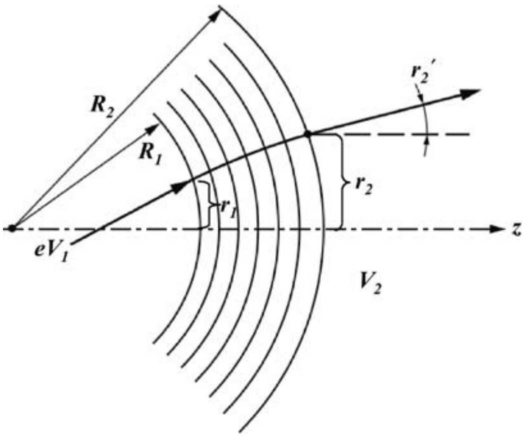

Fig. 1.16. Electrostatic field between concentric spherical equipotential surfaces

1.5 Transfer Matrix of Electrostatic Field Between Spherical Concentric Equipotential Surfaces

The case of charged particles passing through a field between concentric spherical equipotential surfaces with the radii R_1 and R_2 (Fig. 1.16) has also some practical importance, particularly for electron or ion sources [1]. The paraxial transfer matrix is therefore presented here, but without derivation [2]:

$$\begin{pmatrix} r \\ r' \end{pmatrix}_2 = \begin{pmatrix} \frac{R_2}{R_1}(1-k_1) & R_2 k_1 \\ \frac{1}{R_1}(1-k_1-k_2) & k_1+k_2 \end{pmatrix} \begin{pmatrix} r \\ r' \end{pmatrix}_1$$

with the abbreviations

$$k_1 = 2\frac{1-R_1/R_2}{1+\sqrt{V_2/V_1}} \quad \text{and} \quad k_2 = \frac{R_1}{R_2}\sqrt{\frac{V_1}{V_2}}.$$

This is also valid for acceleration ($V_2/V_1 > 1$), drift ($V_2/V_1 = 1$) or deceleration ($V_2/V_1 < 1$). From the above matrix coefficients those of the uniform field can be derived by performing the transitions $R_1, R_2 \to \infty$ and $R_2 - R_1 = L$.

1.6 Acceleration of Charged Particles Emitted from a Spherical Surface

A practical example of acceleration of charged particles from a spherical surface are tip sources of electrons or ions (Fig. 1.17). In these cases

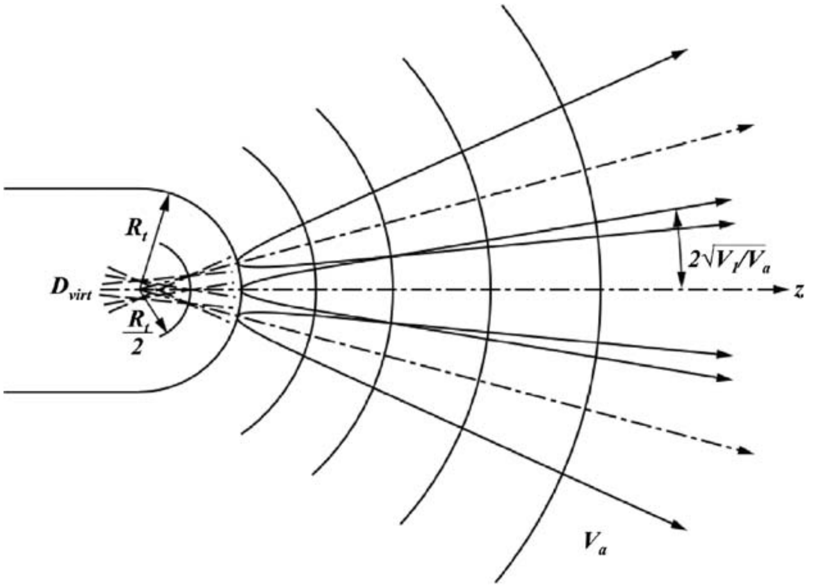

Fig. 1.17. Acceleration of charged particles between concentric spherical emitting and accelerating equipotential surfaces

the acceleration energy eV_a is usually large in comparison to the initial energy eV_1.

Furthermore, the tip radius R_t is small in comparison to the distance of the acceleration electrode, the shape of which is then unimportant because the main acceleration takes place within a distance of a few tip radii in the field determined solely by the tip. Under these conditions, the trajectories of particles starting at a glancing angle from the surface have after acceleration by V_a a slope of $2\sqrt{V_1/V_\mathrm{a}}$ against the surface normal, as compared to $\sqrt{V_1/V_\mathrm{a}}$ in the planar case (comp. (1.32)), and the virtual starting point lies at the distance $R_\mathrm{t}/2$ behind the emitting surface. Thus, the emitting surface is imaged to a virtual surface having the radius $R_\mathrm{t}/2$. But more significant is the fact that all trajectories with maximum slope $2\sqrt{V_1/V_2}$ to the normal of their starting points, when extended backwards to the center of the semi-sphere, have a distance of $\frac{R_\mathrm{t}}{2}2\sqrt{\frac{V_1}{V_\mathrm{a}}} = R_\mathrm{t}\sqrt{\frac{V_1}{V_\mathrm{a}}}$ from the center. Therefore, this appears as the virtual source radius. In this way, microsources can be realized by simple means. For example thermionically emitted particles have initial energies of less than 1 eV, so with an acceleration voltage of 10 kV the virtual source radius is 100 times smaller than the tip radius. All of this is of course valid only when the acceleration voltage is not screened by a Wehnelt electrode, which would drastically alter the field around the tip.

1.7 Passage of Charged Particles Through an Electrode with Round Aperture

In practice, an acceleration field such as shown in Fig. 1.15 is terminated by a planar electrode with an aperture centered to the axis for passage of the accelerated particles (Fig. 1.18). This aperture causes the equipotential surfaces to bulge through it towards the field-free space.

When the field strength is considered near the hole, one sees that a radial component E_r is present acting so as to deflect the particles away from the axis.

It can be shown that this round opening acts as a lens [3]: We place a fictitious cylinder axially through the hole so that its left end protrudes to the region of the undisturbed uniform field, while its right end reaches into the field free space. From the conservation of field line flux we obtain, there being no space charge,

$$r^2\pi E_\mathrm{a} + 2r\pi \int_{-a}^{+b} E_\mathrm{r}\mathrm{d}z = 0\,, \quad rE_\mathrm{a} + 2\int_{-a}^{+b} E_\mathrm{r}\mathrm{d}z = 0. \tag{1.35}$$

A charged particle passing from the left at the distance r from the axis experiences a radial momentum:

$$mv_\mathrm{r} = -\int eE_\mathrm{r}\,\mathrm{d}t = -\frac{e}{v_z}\int_{-a}^{+b} E_\mathrm{r}\,\mathrm{d}z, \tag{1.36}$$

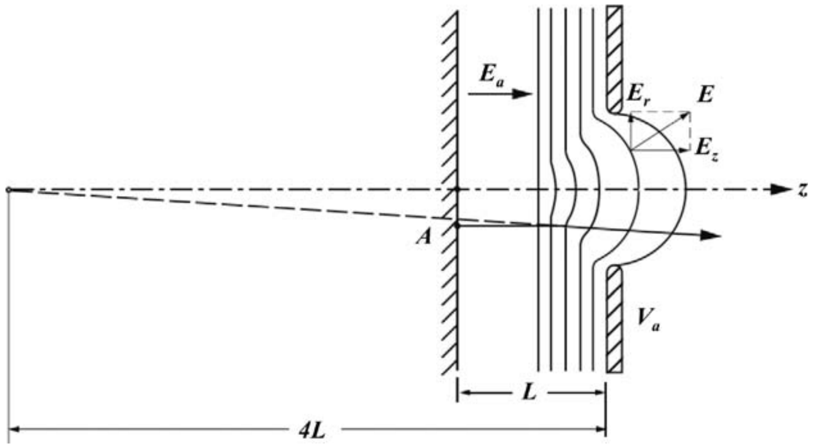

Fig. 1.18. Diverging action of aperture terminating an acceleration field

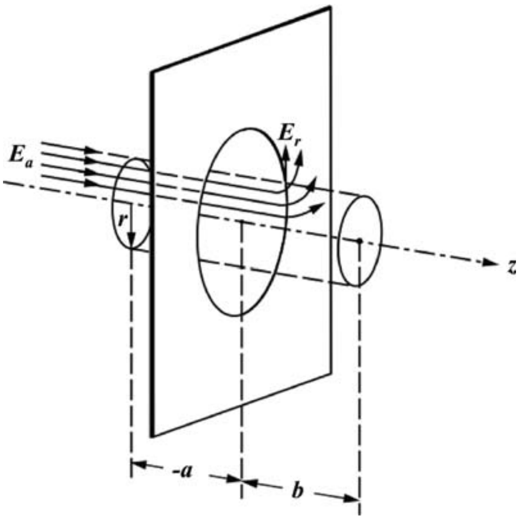

Fig. 1.19. Derivation of lens action of an aperture terminating an acceleration field

whereby $v_z = \mathrm{d}z/\mathrm{d}t, \mathrm{d}t = \mathrm{d}z/v_z$ was substituted. Since the trajectory is paraxial, v_z can be considered constant. Substituting the integral from (1.35) we obtain

$$mv_\mathrm{r} = \frac{er}{2v_z} E_\mathrm{a}. \tag{1.37}$$

The trajectory suffers a kink $\Delta r'$ (Fig. 1.20) given by, with (1.37), $\Delta r' = v_\mathrm{r}/v_z = erE_\mathrm{a}/2mv_z^2$. With $mv_z^2/2 = eV$, the particle energy, we then obtain

$$\Delta r' = \frac{E_\mathrm{a}}{4V} r.$$

The trajectory deflection $\Delta r'$ thus is proportional to the distance from the axis. This is the characterization of a lens. The focal length is given by (comp. (1.4))

$$-f = \frac{r}{\Delta r'} = \frac{4V}{E_\mathrm{a}}. \tag{1.38}$$

As in most practical cases the acceleration energy eV_a is large in comparison with the initial particle energy, one can replace the particle energy at the aperture eV by eV_a, and thus $E_\mathrm{a} = V_\mathrm{a}/L$ (see Fig. 1.18). This yields

$$-f = 4L \tag{1.39}$$

The aperture acts as a diverging lens with the focal length $-4L$ [4].

A particle starting off-axis from point A normal to the surface appears to have started on the axis at a distance of $3L$ behind the emitting surface (Fig. 1.18). The virtual surface located at the distance L

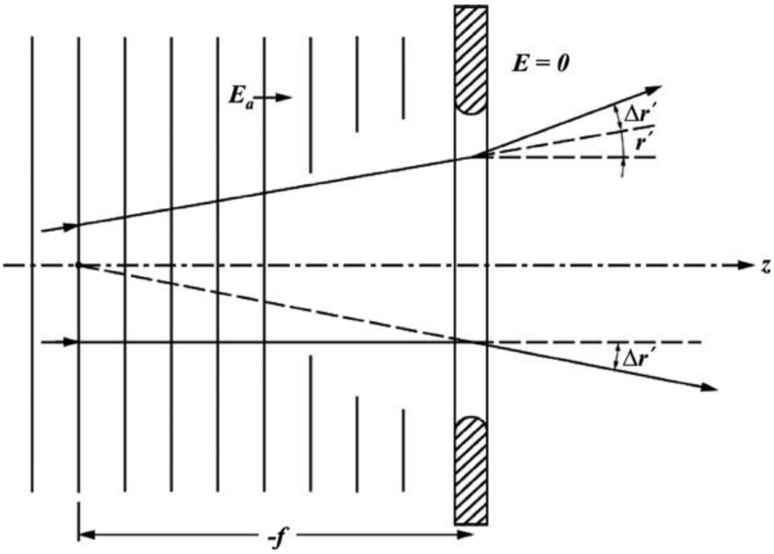

Fig. 1.20. Deflection of trajectories passing through the aperture

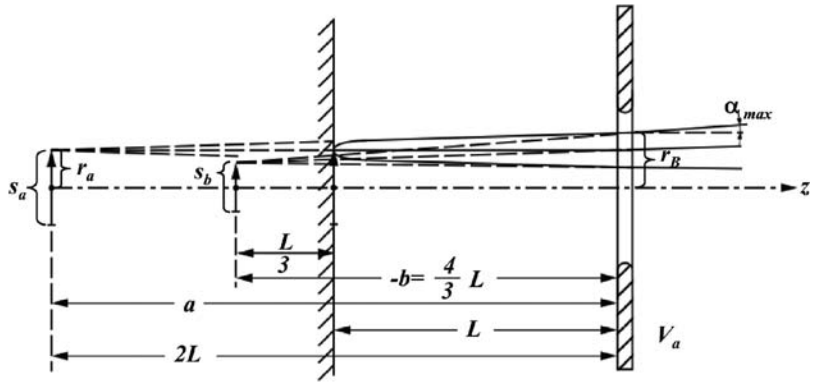

Fig. 1.21. Imaging of emitting surface by accelerating field and aperture

behind the emitting surface (Figs. 1.15 and 1.21) is imaged to a distance of $4/3L$ to the left of the aperture, i.e. to a distance of $L/3$ behind the emitting surface.

This can easily be derived geometrically (see Fig. 1.21) or by calculation with the lens formula (1.8):

$$\frac{1}{b} = -\frac{1}{4L} - \frac{1}{2L} = -\frac{3}{4L} \quad , \quad b = -\frac{4}{3}L .$$

The magnification is $s_\mathrm{b}/s_\mathrm{a} = \frac{4}{3}L/2L = 2/3$.

For particles with initial energy eV_1, the beam radius at the aperture is with (1.31), $r_\mathrm{B} = r_\mathrm{a} + 2L\sqrt{V_1/V_\mathrm{a}}$ and the maximum beam angle α_max after passage through the aperture is, with (1.32) and (1.39),

$$\alpha_\mathrm{max} = \sqrt{\frac{V_1}{V_\mathrm{a}}} + \frac{r_\mathrm{B}}{4L}.$$

These values are important to know when designing acceleration optics without obstructing parts of the beam by electrodes.

The combination: uniform field followed by an aperture, can be treated very simply and conveniently by forming the product of the transfer matrices for the uniform field with that for a lens (1.6):

$$\begin{aligned} M_\mathrm{F} M_\mathrm{L} &\equiv \begin{pmatrix} 1 & \frac{2L}{\sqrt{V_2/V_1}+1} \\ 0 & \sqrt{V_1/V_2} \end{pmatrix} \begin{pmatrix} 1 & 0 \\ -\frac{1}{f_2} & 1 \end{pmatrix} \\ &= \begin{pmatrix} 1 & \frac{2L}{\sqrt{V_2/V_1}+1} \\ -\frac{1}{f_2} & -\frac{1}{f_2}\frac{2L}{\sqrt{V_2/V_1}+1} + \sqrt{\frac{V_1}{V_2}} \end{pmatrix} \equiv M_\mathrm{FL}. \end{aligned}$$

The focal length f_2 is that of the aperture according to (1.39).

1.8 General Aperture

Equation (1.39) is just a special case of the general formula for the lens effect of an aperture separating two regions of different field strengths (Fig. 1.22) [4]:

$$f = \frac{4V_\mathrm{a}}{E_2 - E_1}, \tag{1.40}$$

where V_a is the voltage of the aperture (particle energy = eV_a) measured against the particle source (zero particle energy), and E_1 and E_2 are the field strengths on both sides of the aperture. The signs of the field strengths are defined such that a positive field strength accelerates and a negative field strength decelerates. Thus for $E_1 > E_2$ the focal length is negative, meaning a diverging lens (as in the case above, where $E_2 = 0$), while for $E_1 < E_2$ the aperture acts as a converging lens, f being positive.

Various cases are possible, shown schematically in Fig. 1.23. Cases (a) to (e) are diverging lenses, cases (f) to (k) are converging lenses. Note that all cases, where the curvature of the kink in the potential curve as seen from the zero potential side is concave, are diverging lenses, while those with a convex curvature are converging lenses.

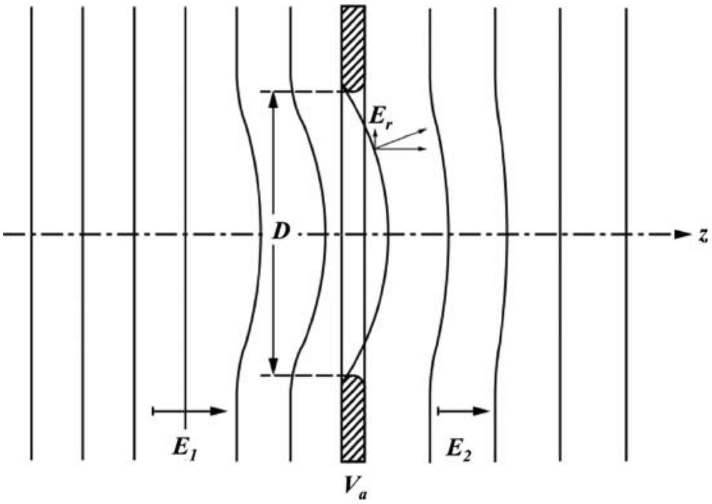

Fig. 1.22. General aperture lens

The transfer matrix of such an aperture is thus (comp. (1.6))

$$\begin{pmatrix} r \\ r' \end{pmatrix}_2 = \begin{pmatrix} 1 & 0 \\ \frac{E_1 - E_2}{4V_\mathrm{a}} & 1 \end{pmatrix} \begin{pmatrix} r \\ r' \end{pmatrix}_1 . \tag{1.41}$$

The properties of lenses composed of more than one aperture can be calculated by transfer matrix multiplication.

The arrangement shown in Fig. 1.24 can be characterized by the matrix product of the transfer matrices: *first aperture* × *uniform field* × *second aperture.* The particles have different energies before and behind the arrangement, viz. eV_1 and eV_2, which is termed an "immersion lens". This notation is chosen in analogy to light optics, where it characterizes a lens with different indices of refraction in front and behind the lens. The arrangement shown in Fig. 1.25 is characterized by the matrix product of five transfer matrices:

first aperture × *first uniform field* × *second aperture* × *second uniform field* × *third aperture.*

It represents a so-called einzel lens when the particle energy is the same before and behind the lens, $eV_3 = eV_1$.

In this way, the lens properties, such as focal lengths and position of principal planes, can be calculated.

When V_3 is different from V_1, one has a three-aperture immersion lens (Fig. 1.25). While with a two-aperture immersion lens the focal lengths are fixed for a given V_2/V_1 ratio, a three-aperture immersion lens opens the

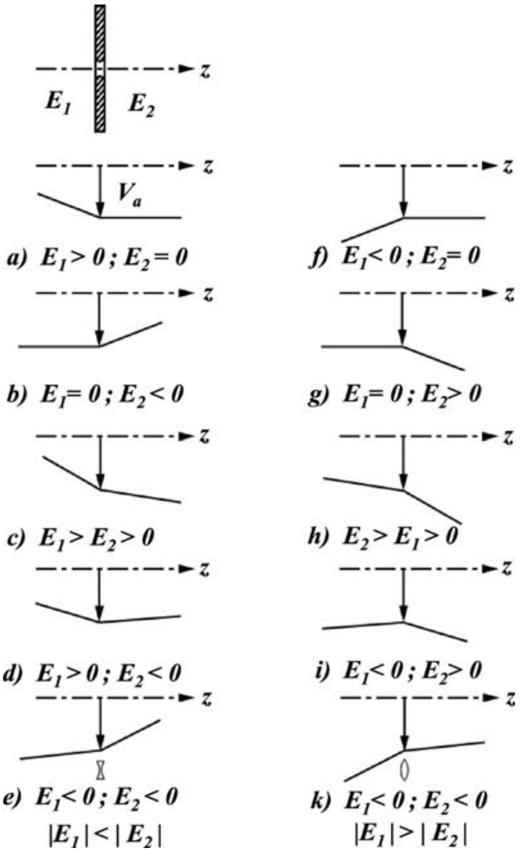

Fig. 1.23. Various cases of aperture lenses: (**a**) to (**e**) diverging lenses, (**f**) to (**k**) converging lenses

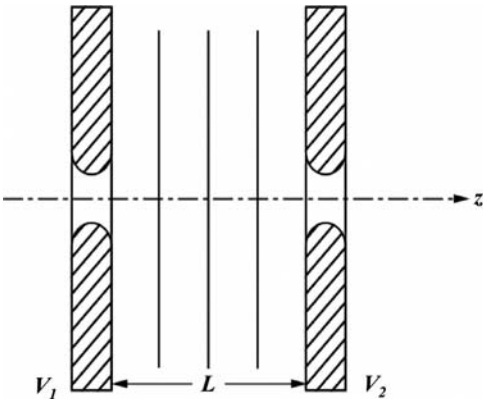

Fig. 1.24. Uniform field between two aperture lenses, constituting an "immersion lens"

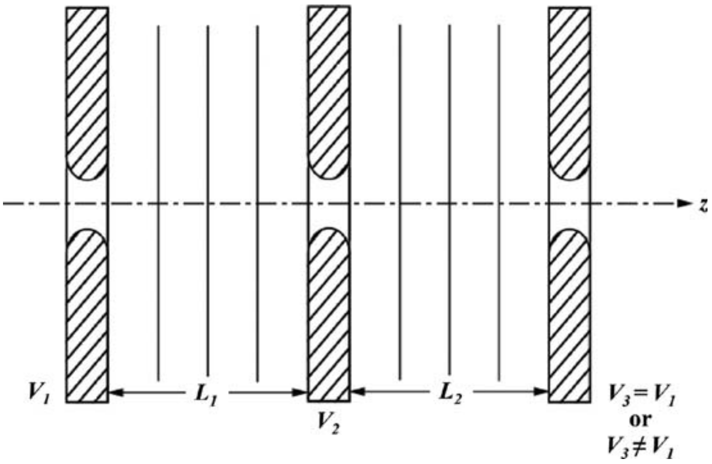

Fig. 1.25. Combination of three apertures and two fields constituting an einzel lens ($V_3 = V_1$) or an immersion lens ($V_3 \neq V_1$)

possibility of adjusting the focusing action for any ratio V_3/V_1 by varying V_2. Such lenses are electrostatic "zoom lenses".

It should be noted that by this simple method of calculating lenses good results are obtained only when the aperture diameters are small in comparison to the distances between the apertures. Otherwise, the fields between the apertures are not uniform and the axial potentials in the aperture differ too much from the potential applied to the aperture electrodes. This restriction for the applicability of (1.40) can be expressed as $L \ll \Delta V/E$, which expression should hold for either side of an aperture where a field exists. ΔV means the potential difference to either next aperture electrode.

When the above condition is not met, i.e. when the aperture diameter is larger, the formula is still applicable with reasonably good results, when for the V_a not the potential of the aperture but for the axis point within the aperture is taken. Because of field penetration these two differ the more the larger the aperture diameter is in relation to the distances of the neighboring apertures. This is the case in particular when V_a has a maximum or a minimum.

1.9 Passage of Charged Particles Through an Electrode with Slotted Aperture

When the aperture in an electrode separating spaces of different field strength is not circular but a slot (Fig. 1.26), such that its width

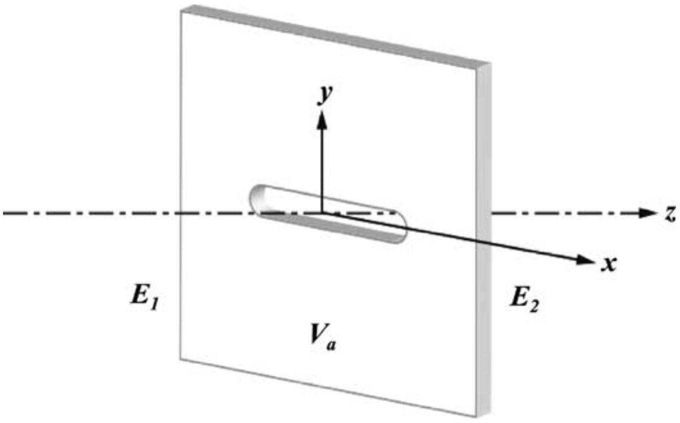

Fig. 1.26. Slotted aperture between different fields

(y-direction) is small in comparison to its length (x-direction), the lens action is only in the y-direction.

The formula for the focal length (comp. (1.40)) is then

$$f = \frac{2V_\mathrm{a}}{E_2 - E_1}. \tag{1.42}$$

The lens action is twice as strong as that of a circular aperture, but occurs only in one azimuthal direction.

In the x-direction no focusing of the trajectories occurs but only a variation of the incremental change of the refractive index. Parallel trajectories continue being parallel (Fig. 1.27).

In case the particles emitted from a planar surface are accelerated through a slotted electrode (Fig. 1.28), the defocusing by the slot has to be taken into account. Its focal length is (for $V_1 \ll V_\mathrm{a}$)

$$-f = \frac{2V_\mathrm{a}}{E} = 2L. \tag{1.43}$$

The virtual subject located at the distance L behind the emitting surface is now imaged to the emitting surface itself with the magnification $r_\mathrm{b}/r_\mathrm{a} = 1/2$.

The beam radius at the aperture is of course the same as with a round aperture

$$r_\mathrm{B} = r_\mathrm{a} + 2L\sqrt{\frac{V_1}{V_\mathrm{a}}},$$

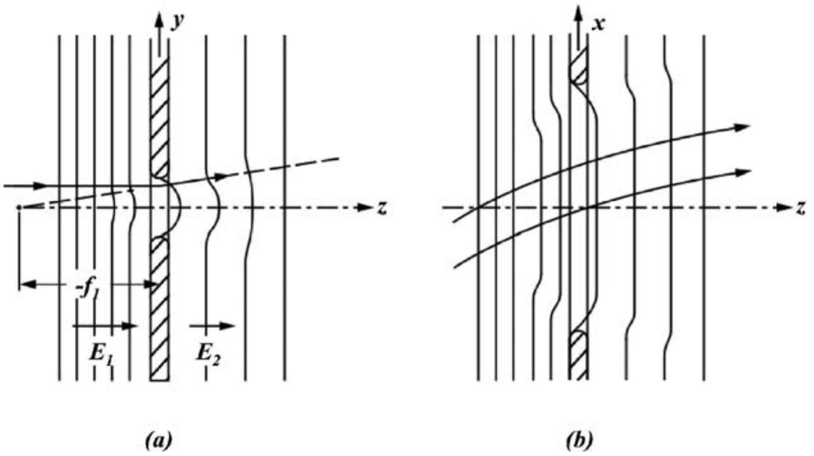

Fig. 1.27. Action of slotted aperture between different fields: (**a**) lens action, (**b**) bending of trajectories

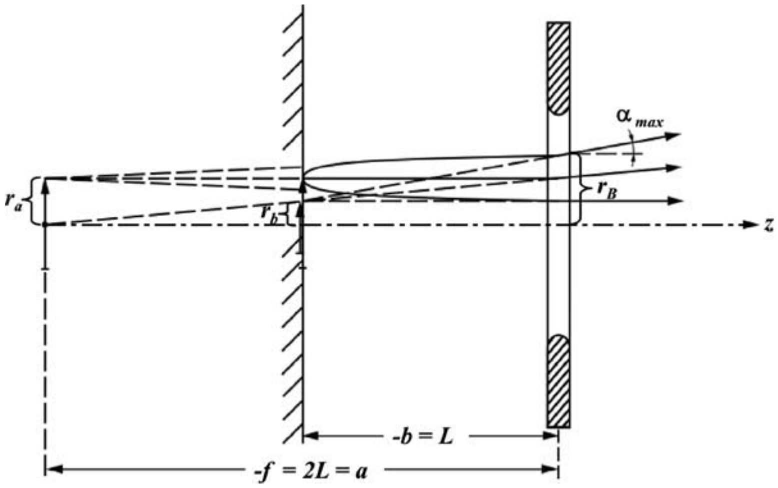

Fig. 1.28. Imaging of emitting surface by acceleration field and slotted aperture

but the maximum beam angle in the direction of the lens action is now

$$\alpha_{\mathrm{max}} = \sqrt{\frac{V_1}{V_{\mathrm{a}}}} + \frac{r_{\mathrm{B}}}{2L}.$$

1.10 Emission Lenses

The usual requirement in dealing with charged particles emitted from a surface is to form them into a beam with a certain energy and shape,

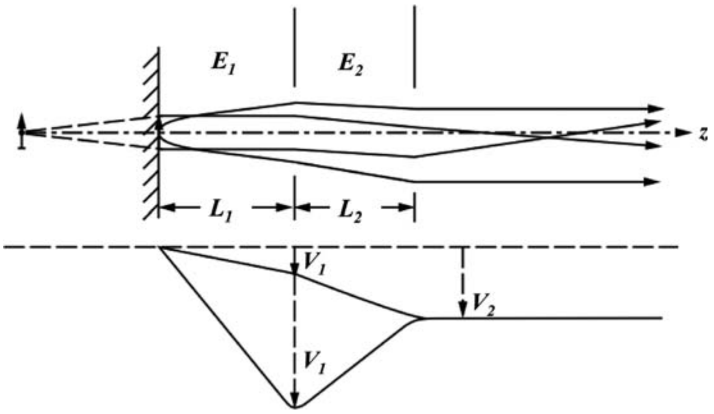

Fig. 1.29. Emission lens with two different modes of operation

or to form an image of the surface with them. This is done with an emission lens (for electrons also called cathode lens).

The simplest emission lens is obtained by adding a second apertured electrode to the acceleration electrode (Fig. 1.29).

The two electrodes with their apertures constitute an immersion lens. Together with the uniform acceleration field they form the emission lens. The lens can be treated by multiplying the matrix for the first aperture lens with that of the combination: field along L_2 plus second aperture lens

$$M = \begin{pmatrix} m_{11} & m_{12} \\ m_{21} & m_{22} \end{pmatrix} = \begin{pmatrix} 1 & 0 \\ -\frac{1}{f_1} & 1 \end{pmatrix} \begin{pmatrix} 1 & \frac{2L_2}{\sqrt{V_2/V_1}+1} \\ -\frac{1}{f_2} & \sqrt{\frac{V_1}{V_2}} - \frac{1}{f_2}\frac{2L_2}{\sqrt{V_2/V_1}+1} \end{pmatrix},$$

where the focal lengths f_1 and f_2 of the two apertures are given by

$$-\frac{1}{f_1} = \frac{E_1 - E_2}{4V_1} = \frac{V_1}{4L_1V_1} - \frac{V_2 - V_1}{4L_2V_1} = \frac{1}{4L_1} - \frac{1}{4L_2}\left(\frac{V_2}{V_1} - 1\right), \tag{1.44}$$

$$-\frac{1}{f_2} = \frac{E_2}{4V_2} = \frac{V_2 - V_1}{4L_2V_2} = \frac{1}{4L_2}\left(1 - \frac{V_1}{V_2}\right). \tag{1.45}$$

We obtain

$$r_2 = m_{11}r_1 + m_{12}r_1', \tag{1.46}$$

$$r_2' = m_{21}r_1 + m_{22}r_1'. \tag{1.47}$$

The matrix coefficients are found to be

$$
\begin{aligned}
m_{11} &= 1 - \frac{1}{f_1}\frac{2L_2}{\sqrt{V_2/V_1}+1} = 1 - \frac{m_{12}}{f_1}, \\
m_{12} &= \frac{2L_2}{\sqrt{V_2/V_1}+1}, \\
m_{21} &= -\frac{1}{f_2} - \frac{1}{f_1}\left(\sqrt{\frac{V_1}{V_2}} - \frac{1}{f_2}\frac{2L_2}{\sqrt{V_2/V_1}+1}\right) = -\frac{1}{f_2} - \frac{m_{22}}{f_1}, \\
m_{22} &= \sqrt{\frac{V_1}{V_2}} - \frac{1}{f_2}\frac{2L_2}{\sqrt{V_2/V_1}+1} = \sqrt{\frac{V_1}{V_2}} - \frac{m_{12}}{f_2}.
\end{aligned}
$$

Several options are open to shape the beam for given distances L_1 and L_2 by variation of the voltage ratio V_1/V_2. The value eV_2 is the energy of the beam after passing through the lens.

An important case for beam sources is telescopic imaging (Fig. 1.30), i.e. particles starting from the surface from different points on parallel trajectories travel again on parallel trajectories after acceleration through the emission lens. In particular, particle trajectories starting parallel to the axis are also parallel to the axis after the lens. The angular spread is then entirely due to the initial energy.

The condition for telescopic imaging is that r_2' be independent of r_1, or in particular that for $r_1' = 0$ also $r_2' = 0$. This is the case for

$$m_{21} = 0. \tag{1.48}$$

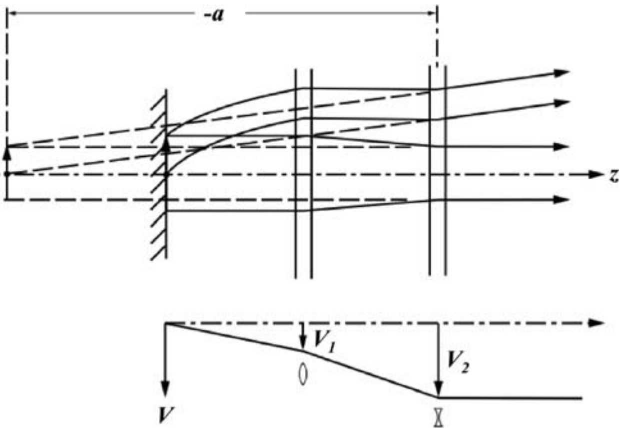

Fig. 1.30. Telescopic imaging through emission lens by converging–diverging apertures

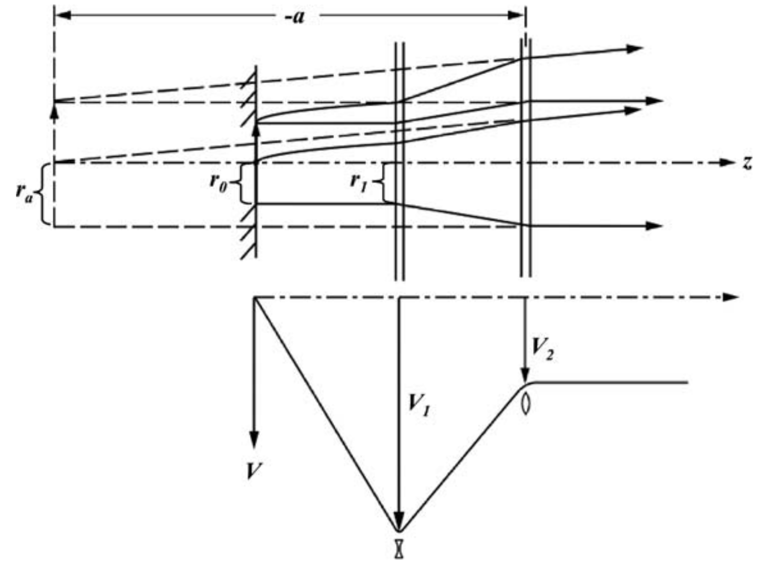

Fig. 1.31. Telescopic imaging through emission lens by diverging–converging apertures

The emission lens thus has the focal length

$$f = -1/m_{21} = \infty.$$

There are the two solutions, shown in Figs. 1.30 and 1.31, which can easily be found (with a pocket calculator). For example, with $L_1 = L_2 = L$, (1.48) yields $V_1/V_2 = 0.34$ and $V_1/V_2 = 2.8$. The first solution corresponds to Fig. 1.30, where the first aperture acts as a focusing and the second as a defocusing lens. In the second solution (Fig. 1.31) the first aperture is a defocusing lens and the second a focusing one. This is called an accel–decel arrangement because the particles are accelerated in L_1 and decelerated in L_2. Comparing the two solutions one sees that, for a given final beam energy eV_2, the field strength in L_1 is much higher in case Fig. 1.31. This can be important when space charge limitations play a role at the emitting surface. There, a higher field strength allows a higher emission current density. On the other hand, for a given beam energy eV_2, the voltage V_1 required in case Fig. 1.31 may become prohibitively high causing breakdown problems.

Other beam parameters have also to be considered: the position of the virtual emitting surface is found with

$$-a = \left(\frac{r_2}{r_2'}\right)_{r_1=2L_1r_1'} = \frac{2L_1m_{11} + m_{12}}{m_{22}}. \tag{1.49}$$

Table 1.1. Telescopic imaging with emission lens after acceleration field ($L_1 = L_2 = L$)

V_1/V_2	m_{11}	m_{12}/L	$m_{21}L$	m_{22}	L/f_1	L/f_2	f/L	$-a/L$
0.34	0.82	0.74	0	0.70	0.24	−0.17	∞	3.4
2.8	1.51	1.25	0	1.11	−0.41	0.45	∞	3.8

Note: These are calculated values for the condition that the aperture diameters are small compared to the aperture distances. This is rarely the case in practice, but by making V_1 adjustable the condition $f = \infty$ can be met

The virtual object radius r_a is found (Fig. 1.31) from $r_1 = r_0$, $r_1' = 0$ for $r_0' = 0$:

$$r_\mathrm{a} = (r_2)_{r_1'=0} = m_{11} r_1, \quad \frac{r_\mathrm{a}}{r_0} = m_{11}. \tag{1.50}$$

The maximum beam diameter and aperture angle are obtained with (1.46) and (1.47) by inserting $r_{1\mathrm{m}}' = \sqrt{V_0/V_1}$ (comp. (1.32)), $r_1 = r_0 + 2L_1 r_{1\mathrm{m}}'$:

$$r_{2\mathrm{m}} = m_{11} r_0 + (2L_1 m_{11} + m_{12})\sqrt{V_0/V_1}, \tag{1.51}$$

$$r_{2\mathrm{m}}' = m_{22}\sqrt{V_0/V_1}, \tag{1.52}$$

where r_0 is the radius of the emitting area on the surface.

With the above relations the properties of the emission lens with telescopic imaging are completely described.

The values of the example $L_1 = L_2 = L$ are compiled in Table 1.1.

Another important application of an emission lens with two apertured electrodes is emission microscopy, where a magnified image of the surface is formed by the emitted particles. The condition for imaging the surface into infinity, in practice to a distance large in comparison with L_1, L_2 is that the trajectories starting from the axis point, $r_0 = 0$, be parallel to the axis after the emission lens. This yields, with $r_1 = 2L_1 r_1'$,

$$\begin{aligned}(r_2')_{r_0=0} &= m_{21} r_1 + m_{22} r_1' \\ &= 2L_1 m_{21} r_1' + m_{22} r_1' = 0, \quad 2L_1 m_{21} + m_{22} = 0.\end{aligned} \tag{1.53}$$

Again, there are, for any ratio L_1/L_2, two solutions V_1/V_2 meeting the above condition (Figs. 1.32 and 1.33). With the same example as above $L_1 = L_2 = L$, these solutions are $V_1/V_2 = 0.18$ and $V_1/V_2 = 4.5$ [5].

Again, as in telescopic imaging, the second solution represents a large accel–decel voltage ratio, and the same applies as above.

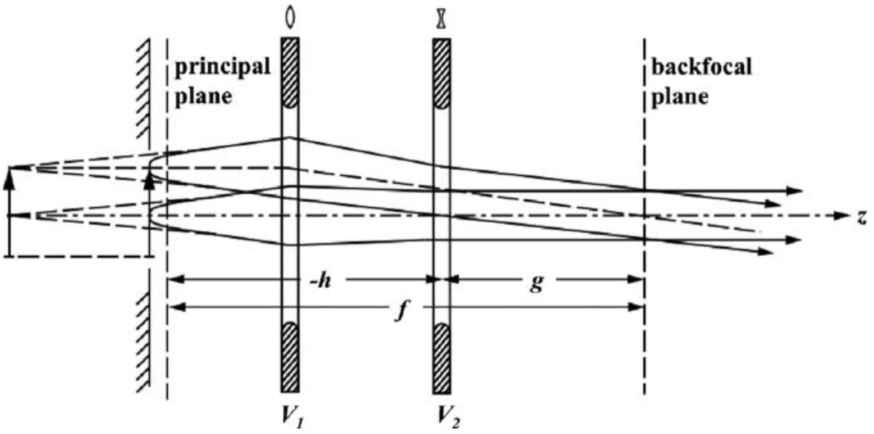

Fig. 1.32. Emission microscopy: Imaging of surface to infinity by converging–diverging apertures

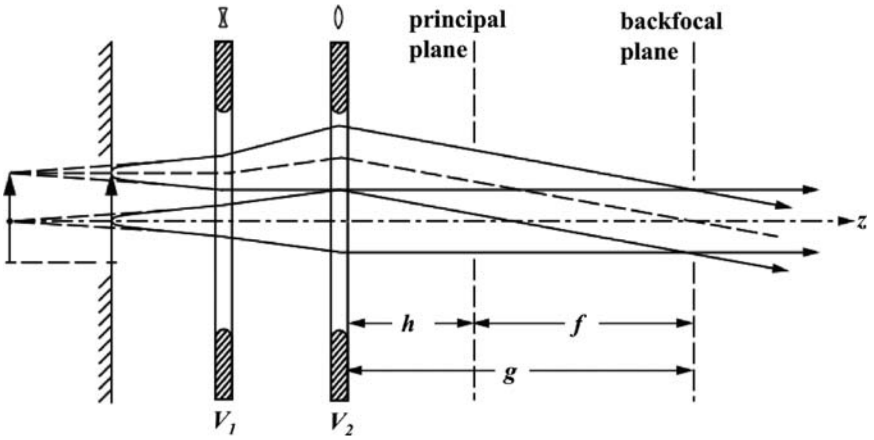

Fig. 1.33. Emission microscopy: Imaging of surface to infinity by diverging–converging apertures

The focal length of the emission lens is found from the relation (with $r_1 = r_0$, $r_1' = r_0' = 0$).

$$f = \frac{r_0}{r_2'} = -\frac{1}{m_{21}}. \tag{1.54}$$

The backfocal plane is where a trajectory starting with $r_0 \neq 0$, $r_0' = 0$ crosses the axis. Its distance from the second electrode of the emission lens is found from (with $r_1 = r_0$, $r_1' = r_0' = 0$)

$$g = \left(\frac{r_2}{-r_2'}\right)_{r_0'=0} = \frac{m_{11} r_0}{-m_{21} r_0} = -\frac{m_{11}}{m_{21}}. \tag{1.55}$$

Table 1.2. Imaging of a planar surface to infinity with a two-aperture emission lens after the acceleration field ($L_1 = L_2 = L$)

V_1/V_2	m_{11}	m_{12}/L	$m_{21}L$	m_{22}	L/f_1	L/f_2	f/L	g/L	h/L
0.18	0.47	0.60	−0.28	0.55	0.89	−0.21	3.6	1.7	−1.9
4.5	1.60	1.36	−0.47	0.93	−0.44	0.88	2.1	3.4	1.3

The distance of the principal plane from the second electrode of the emission lens is $h = g - f$.

In the backfocal plane all beamlets starting from the individual points on the surface cross the axis. Therefore, the total beam has a waist there, the radius of which is given by

$$r_{2\,\mathrm{max}} = 2L_1 m_{11} r'_{1\mathrm{m}} + m_{12} r'_{1\mathrm{m}} = (2L_1 m_{11} + m_{12}) \sqrt{\frac{V_0}{V_1}}. \qquad (1.56)$$

It is proportional to $\sqrt{V_0}$. When an aperture stop is placed in the backfocal plane eliminating a peripheral part of the beam waist, particles with higher initial energies are discriminated against, viz. those with large initial angles α_1 (see Fig. 1.15). This is generally applied in emission microscopy to improve the lateral resolution, which depends on V_0.

In practice, the image of the surface is to be formed not in infinity but at some distance b ($\gg L_1, L_2$). This can be done by making the focal length f slightly shorter, achievable by adjusting V_1/V_2, in case Fig. 1.32 to a slightly smaller, in case Fig. 1.33 to a slightly larger value. The magnification is given by the ratio $M = b/f$.

Values for the example $L_1 = L_2 = L$ are listed in Table 1.2.

When a two-electrode emission lens is used for either of the two applications outlined above, the ratio V_1/V_2 is fixed for a given beam energy and given distances L_1 and L_2. With it also the field strength at the emitting surface, $E_1 = V_1/L_1$, is fixed. More flexibility in the operation of an emission lens is obtained when a third aperture electrode is added (Fig. 1.34). This has the advantage that the field strength at the emitting surface can be adjusted to any desired value, within certain limits, and the beam can be accelerated to any final energy eV_3 with adjustable focusing conditions by adjusting the potential V_2 of the second electrode.

The system can be treated as the one above with a transfer matrix. This is obtained by forming the product of the matrix for the lens of Fig. 1.29 with that for Fig. 1.21 and proceeding as outlined above for the two-electrode system. Again, there are in general two solutions, as

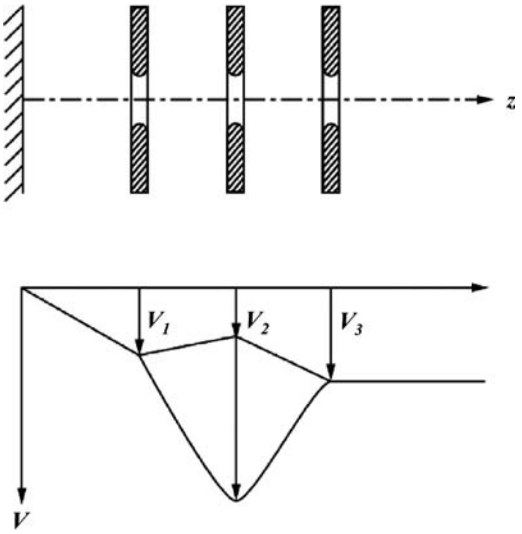

Fig. 1.34. Emission lens with three apertures, two operating modes

indicated in Fig. 1.34. When $V_1 = V_3$, the three electrodes act as an einzel lens (see below).

The treatment of an optical system with the transfer matrices of uniform fields and aperture lenses is fairly accurate only when the electrodes are planar and parallel and the aperture diameters are small in comparison with electrode distances. In practice this is frequently not the case: The electrodes may have to be conical in order to accommodate some primary radiation (see Fig. 1.35b), and the bores may be larger to reduce lens aberrations. This would correspond to a transition from Fig. 1.35a to b. The axial potential distribution which in Fig. 1.35a is made up of straight portions and sharp kinks, is in Fig. 1.35b a smooth curve with only short near-straight portions and gradual bends. Thus, the lens actions are not sharply localized at the apertures but more widely distributed along the curvatures of the potential curve.

The first-order optical properties of a system are completely determined by the axial potential distribution. This is a consequence of the Laplace equation, $\operatorname{div} V = 0$ $\left(\nabla^2 V = 0\right)$, which for rotationally symmetric systems can be written as

$$\frac{\partial^2 V}{\partial r^2} + \frac{1}{r}\frac{\partial V}{\partial r} + \frac{\partial^2 V}{\partial z^2} = 0. \qquad (1.57)$$

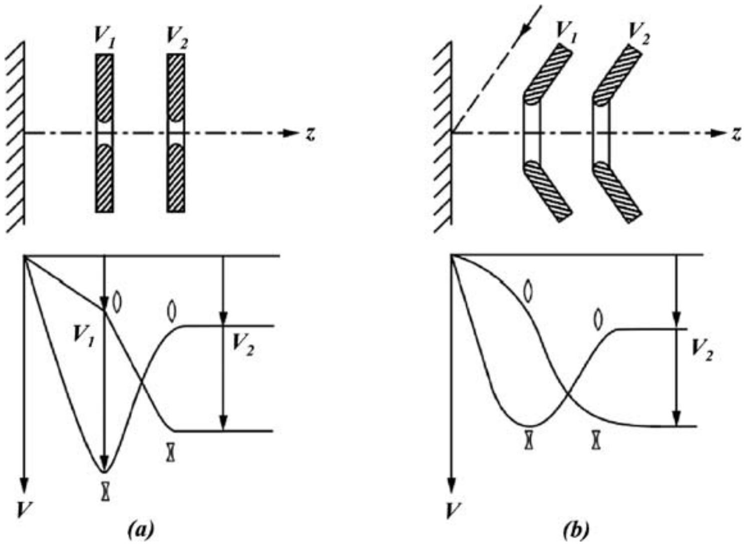

Fig. 1.35. Axial potential distributions of two emission lenses with similar optical properties (comp. Fig. 1.23)

When the axial potential distribution $V(z)_{r=0}$ is given, the paraxial potential distribution is also fixed through (1.57), and with it the paraxial (first order) focusing properties of the system.

Thus, even if the electrodes differ considerably, if the axial potential distribution is similar, so also will be the optical properties of two systems. A great advantage of particle optics compared to light optics is the possibility of continuous variation of optical properties by simple potential variations.

In a triode system such as sketched in Fig. 1.35b with large apertures, the potential V_1 in the case $V_1 < V_2$ may be adjusted to a very low or even negative value. It is then frequently called "Wehnelt" electrode. The acceleration from the surface is effected mainly by field penetration from the second electrode (V_2). This causes a very strong focusing action near the surface such that the beam waist (crossover) occurs within the acceleration field. In such a "gun" the beam crossover serves as a source for further imaging and the "Wehnelt" can be used to control the beam intensity.

1.11 Immersion Lenses

The transfer matrix of an immersion lens composed of two planar apertured electrodes has been given already. In the general case there is no

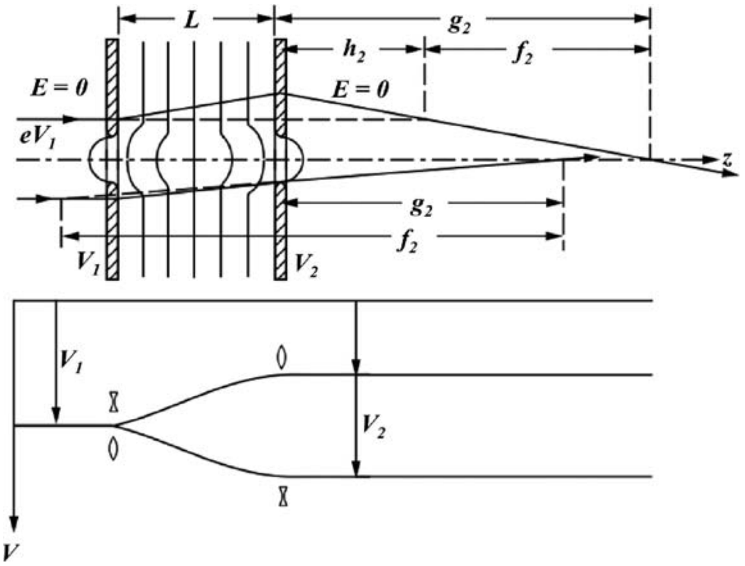

Fig. 1.36. Immersion lens with acceleration ($V_2 > V_1$) or deceleration ($V_2 < V_1$)

field before the first electrode (Fig. 1.36). The focal length of the first aperture is given by

$$\frac{1}{f_1} = \frac{1}{4L}\left(\frac{V_2}{V_1} - 1\right). \tag{1.58}$$

The matrix coefficients are the same as given earlier except that $1/f_1$ is different here.

The two possible cases with acceleration ($V_2/V_1 > 1$) and deceleration ($V_2/V_1 < 1$) are shown in Fig. 1.36. For $V_2/V_1 = 1$ the matrix coefficients become those for a drift space of length L.

Focal length f_2 and distance g_2 of the focal plane in the V_2 space are given by

$$f_2 = -1/m_{21}, \tag{1.59}$$

$$g_2 = -m_{11}/m_{21}. \tag{1.60}$$

The distance of the principal plane from the second electrode is

$$h_2 = g_2 - f_2 = \frac{1 - m_{11}}{m_{21}} = \frac{m_{12}}{m_{21} f_1}. \tag{1.61}$$

When (1.59) is carried out, it simplifies to

$$\frac{f_2}{L} = \frac{4\left(\sqrt{V_2/V_1} + 1\right)}{V_1/V_2 + V_2/V_1 - 2}. \tag{1.62}$$

Since both V_1 and V_2 have to be positive to let particles pass through the apertures, the focal length f is always positive for any ratio V_1/V_2 (except the trivial case $V_2 = V_1$). This can be easily verified by inserting some values of V_1/V_2 into (1.62) for either $V_1/V_2 < 1$ or $V_1/V_2 > 1$. Thus, it is not possible to operate such a lens with telescopic imaging as the emission lens shown in Fig. 1.30 (acceleration field plus immersion lens). This means that any change of beam energy is linked with focusing of the beam by the accelerating or decelerating field.

An immersion lens has different focal lengths on the entrance and exit sides. Since in electrostatic optics particle trajectories are reversible, the optical parameters on the entrance side, f_1, g_1 and h_1 can be found simply by applying (1.59)–(1.61) with the inverse values of V_1/V_2. For f_1 follows from (1.62)

$$\frac{f_1}{L} = \frac{4\left(\sqrt{V_1/V_2}+1\right)}{V_2/V_1 + V_1/V_2 - 2}. \tag{1.63}$$

When we form the ratio f_2/f_1 we find with (1.62) and (1.63)

$$\frac{f_2}{f_1} = \sqrt{\frac{V_2}{V_1}}. \tag{1.64}$$

This is a general property of all immersion lenses. It is analogous to immersion lenses in light optics, where $f_2/f_1 = n_2/n_1$, the ratio of the refractive indices on both sides.

In practice, immersion lenses are frequently constructed with tubular electrodes (Fig. 1.37). This has the advantage that in comparison with an immersion lens as described above, the lens diameter is smaller for a given beam diameter. Furthermore, as a consequence of the smoother axial potential distribution, the spherical image aberration (aperture aberration) is smaller. The field penetration into the tubes drops to a negligible value at a depth of about the inner tube diameter. Thus, this depth must be kept clear of any constructional elements, which could disturb the field distribution.

The lens properties are determined experimentally or by computation. A variety of lenses with different geometries have been published in tabulated form [6–9].

As is shown in Fig. 1.37, the principal planes are always located on the "slower" side from the end of the lens field. Frequently, particularly with tubular lenses such as shown in Fig. 1.37, they are also interchanged, meaning that the trajectories cross P_2 before P_1.

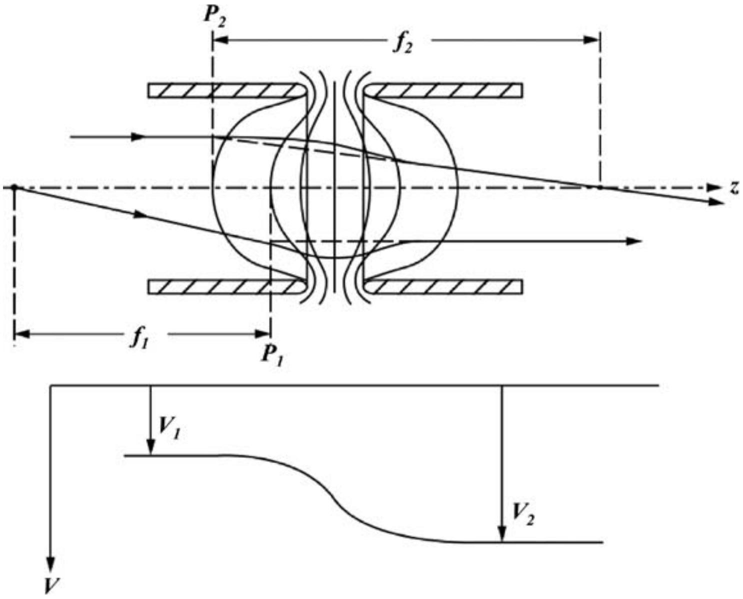

Fig. 1.37. Immersion lens with tubular electrodes

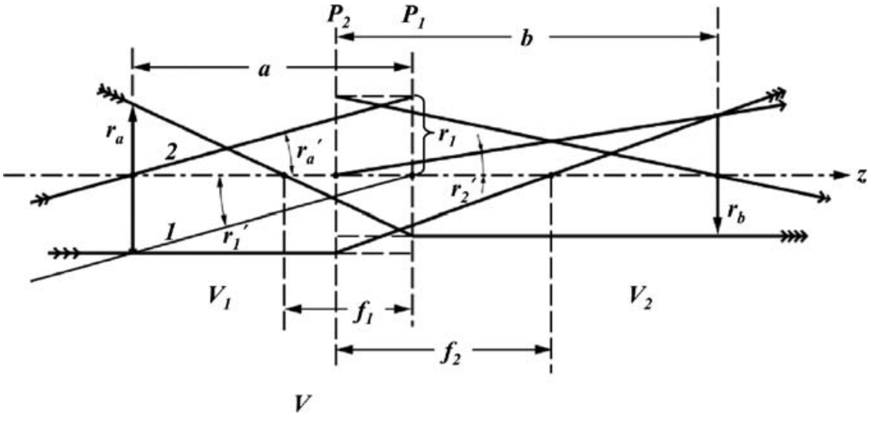

Fig. 1.38. Graphic construction of imaging through immersion lens

When the focal lengths and principal planes are known for a given ratio V_1/V_2 – their position depends on V_1/V_2 – then the imaging properties can be easily found (Fig. 1.38).

Trajectory 1, going through the axis points of P_1 and P_2, is only refracted: $r_2' = r_1'\sqrt{V_1/V_2}$ (comp. (1.21)). For trajectory 2, passing through the lens at some distance r_1 from the axis, we have

$$r'_2 = r'_1\sqrt{\frac{V_1}{V_1}} - \frac{r_1}{f_2}, \tag{1.65}$$

where the first term denotes the refraction and the second the focusing. The equation of trajectory 1 in the r–z coordinate system (V_2-space) is thus

$$r\left(V_2\right) = r_1 + zr'_2 = r_1 + z\left(r'_1\sqrt{\frac{V_1}{V_2}} - \frac{r_1}{f_2}\right), \tag{1.66}$$

and with $r_1 = ar'_1$ ($a =$ object distance) and $f_1/f_2 = \sqrt{V_1/V_2}$

$$r\left(V_2\right) = r'_1\left[a + z\sqrt{\frac{V_1}{V_2}}\left(1 - \frac{a}{f_1}\right)\right]. \tag{1.67}$$

Trajectory 1 crosses the axis ($r\left(V_2\right) = 0$) at the distance $z = b$. This inserted in (1.67) yields the imaging equation for immersion lenses

$$\frac{1}{b} + \sqrt{\frac{V_1}{V_2}}\left(\frac{1}{a} - \frac{1}{f_1}\right) = 0. \tag{1.68}$$

The inverse image distance is thus found to be

$$\frac{1}{b} = \sqrt{\frac{V_1}{V_1}}\left(\frac{1}{f_1} - \frac{1}{a}\right) = \frac{1}{f_2} - \frac{1}{a}\sqrt{\frac{V_1}{V_2}}. \tag{1.69}$$

The magnification is found to be (see Fig. 1.38)

$$M = \left|\frac{r_{\mathrm{b}}}{r_{\mathrm{a}}}\right| = \frac{r'_2 b}{r'_1 a} = \frac{b}{a}\sqrt{\frac{V_1}{V_2}}. \tag{1.70}$$

From the figure one can extract the relations

$$\frac{r_{\mathrm{a}}}{a - f_1} = \frac{r_{\mathrm{b}}}{f_1}; \quad \frac{r_{\mathrm{b}}}{b - f_2} = \frac{r_{\mathrm{a}}}{f_2}.$$

This yields

$$\frac{r_{\mathrm{a}}}{r_{\mathrm{b}}} = \frac{a - f_1}{f_1} = \frac{f_2}{b - f_2}$$

and

$$\left(a - f_1\right)\left(b - f_2\right) = f_1 f_2. \tag{1.71}$$

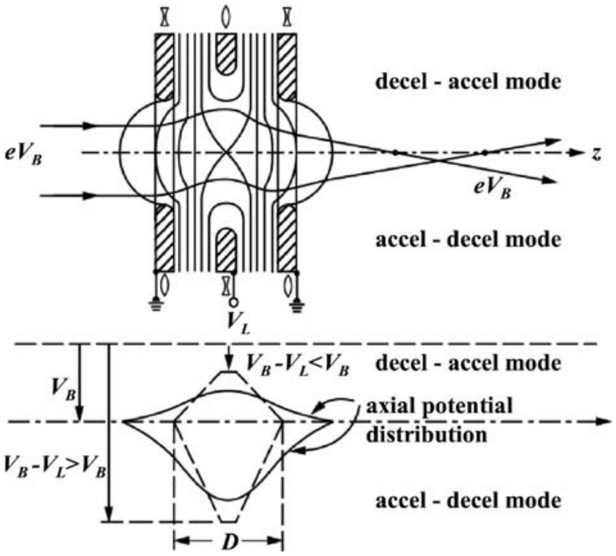

Fig. 1.39. Einzel lens built of three planar apertured electrodes

This is another form of the imaging equation. In light optics it is called Newton's imaging equation. It is equivalent to (1.68) and (1.69).

The above equations are valid not only for two-electrode immersion lenses, but for all lenses with different axial potentials in front and behind. The number of electrodes is arbitrary. Very frequently three-electrode immersion lenses are used. They provide more flexibility because energy change and focusing of the beam can be adjusted independently, within certain limits. They are constructed like einzel lenses (see Fig. 1.39), with the only difference that the first and last electrodes lie on different potentials.

1.12 Einzel Lenses

The notation "einzel lenses" (einzel=single) is commonly used for three-electrode lenses, where the first and third electrodes are at the same potential. Just as immersion lenses, einzel lenses are always focusing lenses. Fig. 1.39 shows an example of a symmetric einzel lens constructed of apertured electrodes. The potential distribution resembles a saddle surface when the equipotential lines are considered as topographic level lines. Two modes of lens operation are possible: decel–accel and accel–decel, represented by the axial potential distribution shown in the figure. The "lens strength" D/f of the lens (Fig. 1.40)

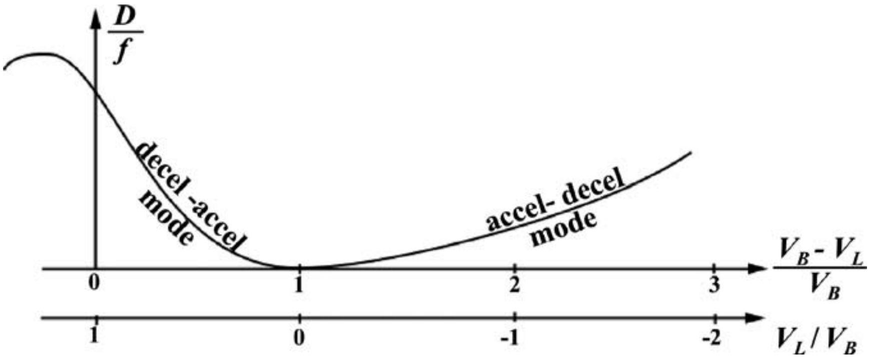

Fig. 1.40. Typical dependency of refractive power of einzel lens on the potential of the middle electrode V_L for a beam energy eV_B

has two branches for the two modes. The decel–accel mode is the one used in most practical applications for two reasons: firstly, since usually the particle source is floating by the acceleration voltage off ground and the two outer electrodes of the lens are grounded, the center electrode is then at a voltage with the same sign as the source voltage and can therefore be supplied via a voltage divider. Secondly, a high refractive power (=short focal length) can be achieved with a center electrode voltage comparable to the source voltage. In the accel–decel mode, a separate voltage supply with the opposite polarity as the source voltage supply is required, and much higher voltages are required for the same refractive power.

In spite of this, the accel–decel mode is advantageous when the focal length required is not too short. The reason is that in this mode both the spherical and the chromatic image aberrations are smaller than in the decel–accel mode. The former is smaller because the trajectories are closer to the axis. The latter because inside the lens field the relative energy spread $\Delta V/V$ of the particles is smaller. If this mode is chosen, the bore of the center electrode can be made smaller than that of the outer electrodes (Fig. 1.41). This reduces the voltage required for a given focal length.

On the decel–accel branch of the working curve, when the voltage ratio $V_\mathrm{L}/V_\mathrm{B}$ is increased to even more positive values, the lens strength D/f goes through a maximum, i.e. the focal length f through a minimum. This is the case because with increasing lens strength the focus approaches the lens field. By judicious choice of the lens geometry, this focal length minimum can be made to occur exactly at $V_\mathrm{L}/V_\mathrm{B} = 1$

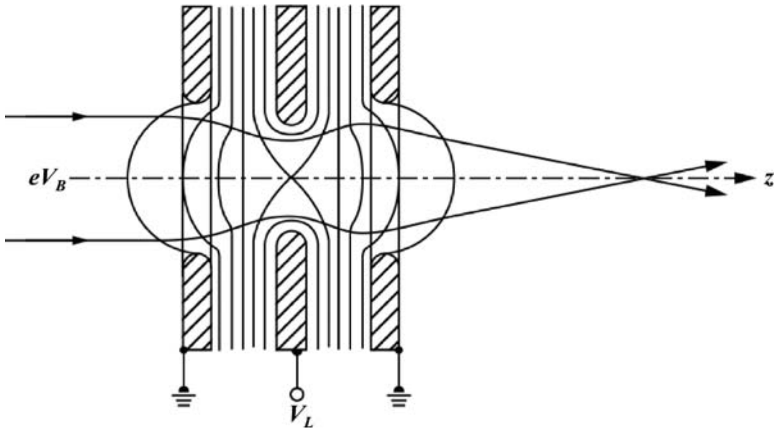

Fig. 1.41. Einzel lens geometry advantageous for accel–decel mode

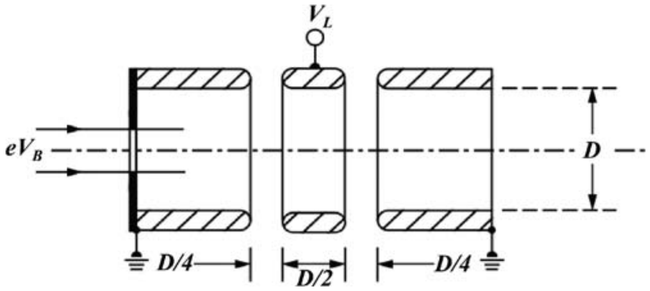

Fig. 1.42. Geometry of einzel lens having maximum refractive power with $V_{\rm L} = V_{\rm B}$ (middle electrode at source potential). The focal length is then $f \approx 2D$. For $V_{\rm L} = 0.5$ $V_{\rm B}$ the focal length becomes $f \approx 10D$

(see Fig. 1.42). For some applications this is advantageous because then both the source and the lens can be supplied by the same voltage.

When the ratio $V_{\rm L}/V_{\rm B}$ is increased beyond +1, there comes a point when the potential of the saddle point equals that of the source, i.e. the particles are slowed down to zero energy, and at a potential slightly above they are reflected. This is one way of switching a beam off.

Figures 1.42–1.45 show examples of various einzel lenses.

In the construction of lenses the most important feature is good concentricity of the lens elements in connection with the necessary electrical insulation to guarantee voltage stability. Distances and contours are less critical as long as everything is rotationally symmetric.

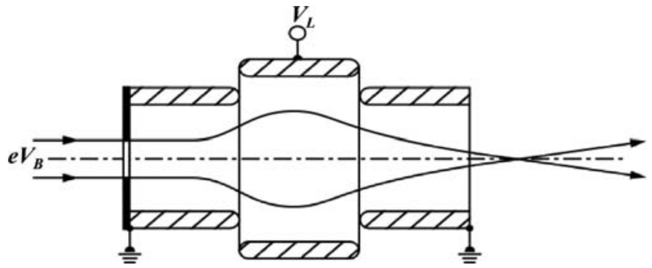

Fig. 1.43. Example of einzel lens with decel–accel mode

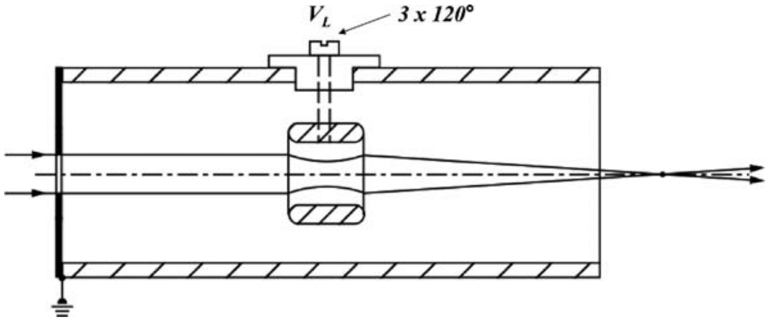

Fig. 1.44. Example of einzel lens with accel–decel mode

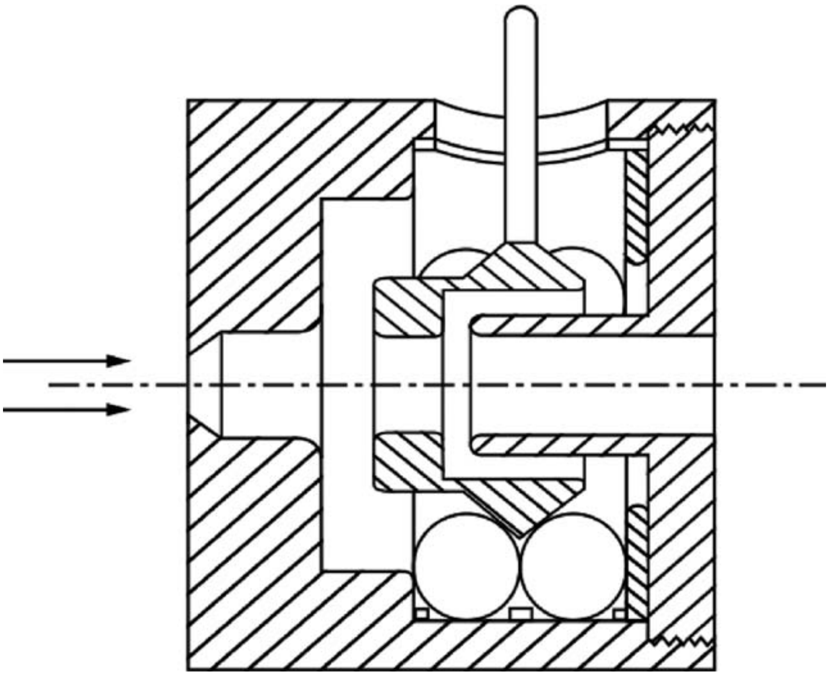

Fig. 1.45. Example of einzel lens where the middle electrode is centered and insulated by six precision ceramic balls

Figure 1.45 shows an example of an einzel lens, where the center electrode is held between six high precision sapphire (or alumina) spheres. The lens is self-centering during assembly and the voltage stability is very good because the center electrode touches the centering insulation spheres at six points only. Depending on the application, the electrode contours can be chosen arbitrarily.

2

Electrostatic Deflection

Summary. Optical parameters and dispersive properties of electrostatic sector fields are discussed.

The passage of charged particles through uniform electrostatic fields has been treated in the first section already for the two cases of deflection by large angles and acceleration or deceleration. The following section deals with deflection elements for beam steering with small deflection angles and sector fields with large angles. In both cases the beam energy is not altered by the passage through the device.

2.1 Parallel Plate Condenser

For beam steering, be it adjustment or scanning, a pair of parallel plates with a deflection voltage applied between them is the most commonly used device. Its deflection properties can be easily derived from first principles.

The field can be assumed to be sharply terminated at both ends by "effective boundaries", so that the effective length L of the deflector is longer than its physical length. This takes into account the effect of the fringe fields. The particle enters the field on the x-axis of the $x-y$ coordinate system (Fig. 2.1) with energy eV_0. The central plane ($y = 0$) has the potential V_0, the deflection voltage is supplied symmetrically to V_0.

From there on it experiences the deflection force

$$eE = m\ddot{y}. \tag{2.1}$$

We can integrate with respect to time, whereby starting time and transverse starting velocity are set to be zero at x, $y = 0$:

$$\ddot{y} = \frac{e}{m}E, \quad \dot{y} = \frac{e}{m}E\,t, \quad y = \frac{eE}{2m}t^2. \tag{2.2}$$

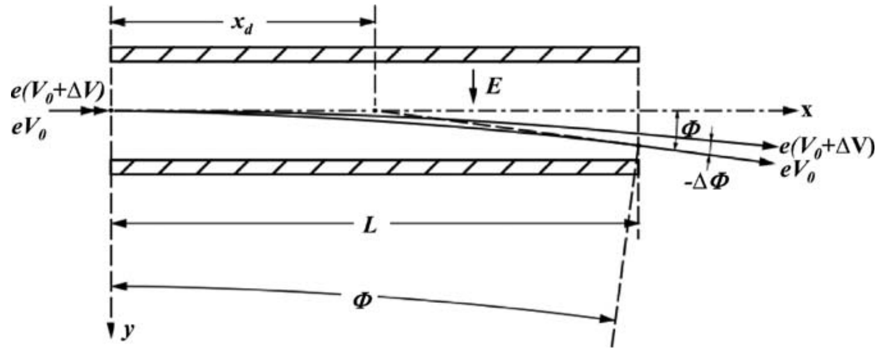

Fig. 2.1. Deflection and dispersion by parallel plate condenser

The axial starting velocity is $v_0 = \sqrt{2eV_0/m}$. We can replace t in (2.2) by $t = x/v_0$ and obtain then

$$y = \frac{E}{4V_0}x^2, \quad y' = \frac{E}{2V_0}x, \tag{2.3}$$

and for $x = L$

$$y_1 = \frac{E}{4V_0}L^2, \quad y_1' = \frac{E}{2V_0}L. \tag{2.4}$$

The virtual deflection center is located at

$$x_\mathrm{d} = L - y_1/y_1' = L/2. \tag{2.5}$$

For small deflection angles the tangent can be replaced by the angle

$$\phi = \frac{EL}{2\,V_0}. \tag{2.6}$$

The particle energy, which increases slightly inside the field to $e\,(V_0 + Ey)$, drops back to eV_0 after passage of the fringe field at the exit.

Above the trajectories for singly charged particles are calculated. Multiply charged particles follow the same trajectories in a deflection field if they were accelerated by the same voltage, because their charge drops out. If they however enter the deflection field with the same energy as singly charged particles, they experience more deflection according to the stronger deflection force neE, n being the number of elementary charges.

Since the deflection angle ϕ depends on the particle energy eV_0, the deflection field causes also energy dispersion. Particles with the energy $eV_0\,(1 + \delta)$ are deflected slightly differently. The term $\delta = \Delta V/V_0$ denotes the relative energy deviation.

By differentiating (2.6) with respect to V_0 one obtains

$$\Delta\phi = -\frac{EL}{2\,V_0^2}\Delta V = -\phi\delta. \tag{2.7}$$

Thus, the value of the energy dispersion factor is identical with the deflection angle ϕ.

2.2 Cylindrical Condenser

The energy dispersion of a parallel plate condenser is rather small (see (2.7)) because only small deflection angles are possible. Therefore, when an electrostatic deflection field is to be used for its energy dispersion, larger deflection angles are required. The use of a uniform field for energy dispersion was described already. For many applications, such a field requires an inconveniently large space and also a voltage of half the beam acceleration voltage. A more popular energy spectrometer is the cylindrical condenser (Fig. 2.2) [10]. Voltages V_a, V_b are applied to the plates so that the middle cylindrical surface lies at the potential outside the field (usually ground potential).

The field strength $E_0 = V_\mathrm{d}/d$ in the center is chosen so that particles entering with energy eV_0 on the entrance axis travel on a circular

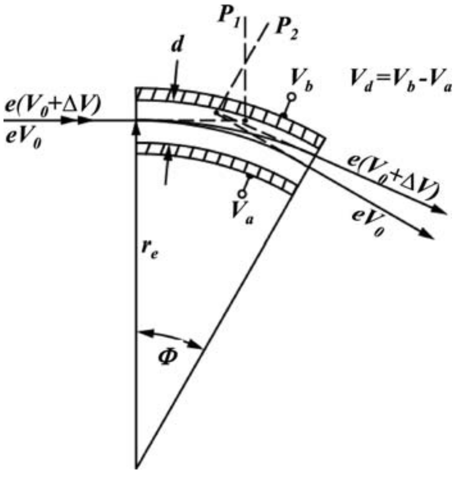

Fig. 2.2. Deflection and dispersion by cylindrical condenser

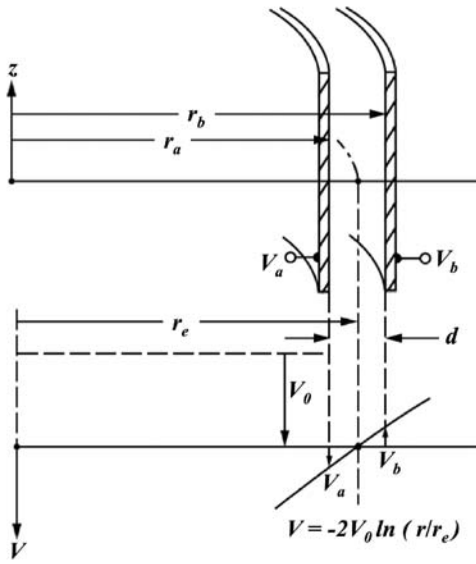

Fig. 2.3. Potential distribution in a cylindrical condenser. $V_\mathrm{a} = -2V_0 \ln (r_\mathrm{a}/r_\mathrm{e})$, $V_\mathrm{b} = -2V_0 \ln (r_\mathrm{b}/r_\mathrm{e})$

trajectory along the middle, which is the optic axis. The electrical centripetal force has to balance the centrifugal force:

$$eE_0 = \frac{mv_0^2}{r_\mathrm{e}} = \frac{2eV_0}{r_\mathrm{e}}, \quad E_0 = \frac{2V_0}{r_\mathrm{e}}. \tag{2.8}$$

In order to find the dispersive and focusing properties of the cylindrical condenser the paraxial trajectories have to be calculated.

The potential in between the plates can be written to be (Fig. 2.3)

$$V(r) = -2V_0 \ln (r/r_\mathrm{e}). \tag{2.9}$$

With this, the field strength results as

$$E(r) = -\frac{\mathrm{d}V(r)}{\mathrm{d}r} = 2\frac{V_0}{r}, \tag{2.10}$$

and for $r = r_\mathrm{e}$ one obtains (2.8). The particle energy in the field is

$$eV_0 + eV(r) = eV_0 \left(1 - 2\ln\frac{r}{r_\mathrm{e}}\right). \tag{2.11}$$

Developed in a Taylor series about $r = r_\mathrm{e}$, (2.9) and (2.10) can be rewritten, using the coordinate $\rho = (r/r_\mathrm{e}) - 1$:

$$V(\rho) = -2V_0\left(\rho - \frac{\rho^2}{2} + \frac{\rho^3}{3}\cdots\right), \tag{2.12}$$

$$E(\rho) = E_0\left(1 - \rho + \rho^2\cdots\right). \tag{2.13}$$

As a test, the Laplace equation (1.57) can be applied to (2.12). Since there is no z-dependence, it reads here

$$\frac{\partial^2 V}{\partial r^2} + \frac{\partial V}{r\partial r} = 0 \text{ or } \frac{\partial^2 V}{\partial \rho^2} + \frac{\partial V}{(1+\rho)\,\partial\rho} = 0.$$

The inner plate surfaces are located at $\rho_\mathrm{a} = -d/2r_\mathrm{e}$ and $\rho_\mathrm{b} = d/2r_\mathrm{e}$.

Inserting these into (2.12) we obtain the voltages (for negative particles) which have to be applied to the plates so that the middle is at zero potential:

$$V_\mathrm{a} = V_0\frac{d}{r_\mathrm{e}}\left(1 + \frac{1}{4}\frac{d}{r_\mathrm{e}}\right),$$

$$V_\mathrm{b} = -V_0\frac{d}{r_\mathrm{e}}\left(1 - \frac{1}{4}\frac{d}{r_\mathrm{e}}\right). \tag{2.14}$$

The cube term of (2.12) can be neglected.

The deflection voltage across the plates is then

$$V_\mathrm{d} = V_\mathrm{a} - V_\mathrm{b} = 2\frac{d}{r_\mathrm{e}}V_0. \tag{2.15}$$

The equations of motion for particles outside the optic axis are

$$m\ddot{r} = mr\dot{\varphi}^2 - eE, \tag{2.16}$$

$$mr^2\dot{\varphi} = \text{const.} \tag{2.17}$$

These are differential equations of an oscillation about the optic axis.

After integration to first order and elimination of the time the trajectory equation results. It has a period of $\pi\sqrt{2}$. By inserting the boundary conditions, including also the arrival energy $eV = eV_0(1+\delta)$, the focusing and dispersive properties of a sector field with a certain sector angle ϕ are found. The mass m drops out, only the energy eV of the particles matters.

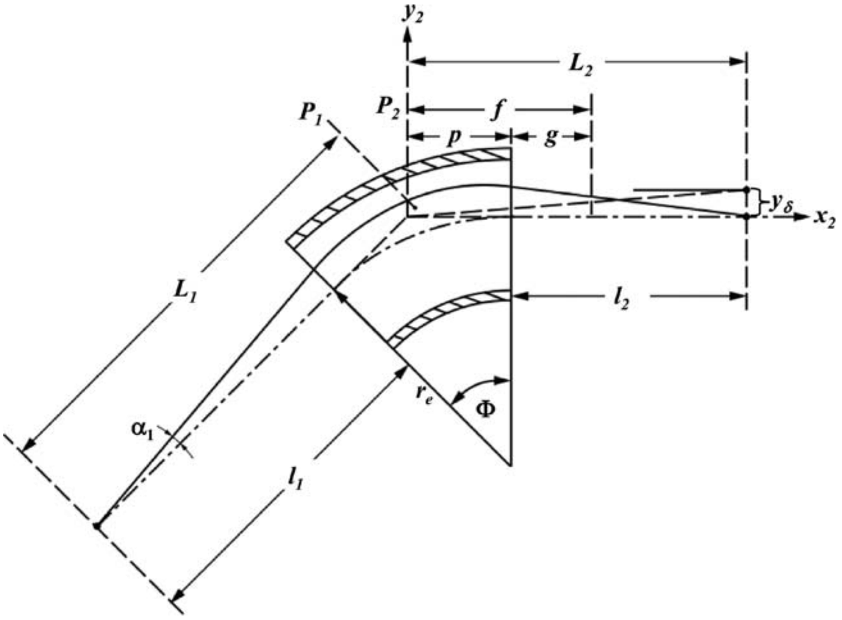

Fig. 2.4. Cylindrical condenser acting as thick lens

It is found that the cylindrical condenser sector field acts as a thick lens (Fig. 2.4) with two principal planes. In the exit principal plane P_2 the center of energy dispersion is located. In the x_2, y_2 coordinate system the equation of a trajectory leaving the sector field can be written

$$y_2 = L_1\alpha_1 + x_2\left[\left(1 - \frac{L_1}{f}\right)\alpha_1 + \lambda\delta\right] . \tag{2.18}$$

It is the equation of a lens plus the dispersion term $\lambda\delta$. The transfer matrix from the entrance principal plane P_1 to the exit principal plane P_2 is

$$\begin{pmatrix} y_2 \\ y_2' \\ \delta_2 \end{pmatrix} = \begin{pmatrix} 1 & 0 & 0 \\ -\frac{1}{f} & 1 & \lambda \\ 0 & 0 & 1 \end{pmatrix} \begin{pmatrix} y_1 \\ y_1' \\ \delta_1 \end{pmatrix} , \quad \begin{aligned} y_2 &= y_1 , \\ y_2' &= -\tfrac{y_1}{f} + y_1' + \lambda\delta , \\ \delta_2 &= \delta_1 = \delta , \end{aligned} \tag{2.19}$$

with $L_1\alpha_1 = y_1$, $\alpha_1 = y_1'$.

The parameters of the electrostatic sector field are:
focal length

$$f = \frac{r_\mathrm{e}}{\sqrt{2}\sin\left(\sqrt{2}\phi\right)} , \tag{2.20}$$

energy dispersion factor

$$\lambda = \frac{\sin\left(\sqrt{2}\phi\right)}{\sqrt{2}}, \tag{2.21}$$

focal distance (distance of focus from field boundary)

$$g = \frac{r_\mathrm{e}\cot\left(\sqrt{2}\phi\right)}{\sqrt{2}}, \tag{2.22}$$

distance of principal planes from field boundary

$$p = f - g = \frac{r_\mathrm{e}\tan\left(\phi/\sqrt{2}\right)}{\sqrt{2}}. \tag{2.23}$$

For small sector angles ϕ the sector field can be considered a parallel plate condenser, and indeed, the dispersion factor becomes (with $\sin(\sqrt{2}\phi) \approx \sqrt{2}\phi$) $\lambda = \phi$ (comp. (2.7); the different sign follows from the differently defined ordinate). Also, the distance of the deflection center becomes ($\tan(\phi/\sqrt{2}) \approx \phi/\sqrt{2}$) $p = r_\mathrm{e}\phi/2 = L/2$, when L ($= r_\mathrm{e}\phi$) is the length of the plates. It also turns out that the parallel plate condenser has weak focusing properties, the focal length being $f = r_\mathrm{e}/2\phi = L/2\phi^2$ [11]. From (2.18) the imaging equation can be deduced, with $x_2 = L_2$ (image distance) for $y_2 = 0$ and $\delta = 0$:

$$L_2 = \frac{L_1}{L_1/f - 1}. \tag{2.24}$$

The magnification is $s_2/s_1 = L_2/L_1$. The theoretical energy resolution is given when the image width s_2 equals the energy dispersion $y_2(\delta) \equiv y_\delta$. Then the images of an entrance slit of width s_1 formed by the two beams of energies eV_0 and $e(V_0 + \Delta V)$ just touch each other. Usually another slit, the exit slit, is placed there to stop the particles with energy $e(V_0 + \Delta V)$ and thus eliminate them from the beam. For intensity reasons the exit slit should be made as wide as the image of the entrance slit. If it is wider, one loses energy resolution, if it is narrower, one loses intensity without gaining energy resolution. With the exit slit thus chosen, the energy distribution behind it will be triangular with FWHM $e\Delta V$ and a base width of $2e\Delta V$ (Fig. 2.5), the tip reaching the original energy distribution.

When an energy bandwidth $e\Delta V$ is to be selected for further use, the mean pass energy should of course be set at the maximum of the original

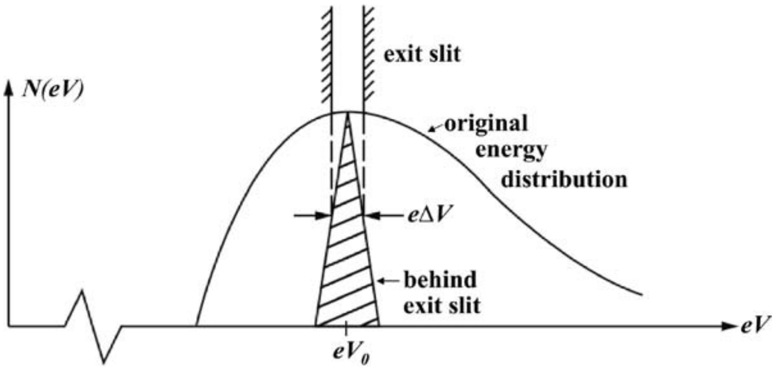

Fig. 2.5. Energy resolution of cylindrical condenser

energy distribution. When the energy distribution is to be surveyed, the pass energy is scanned over the energy distribution. The theoretical energy resolution is obtained from the relation

$$s_1 \frac{L_2}{L_1} = y_2(\delta) = L_2 \lambda \left(\frac{\Delta V}{V_0}\right)_{\mathrm{th}}, \quad \left(\frac{\Delta V}{V_0}\right)_{\mathrm{th}} = \frac{s_1}{L_1} \frac{1}{\lambda}. \tag{2.25}$$

Note that the image distance L_2 disappears. Also the radius r_e does not appear in (2.25). This means, the same energy resolution is obtained with a fixed ratio s_1/L_1 using a condenser with the same sector angle ϕ but different radii r_e. The radius r_e, however, determines the angular magnification and also the image aberrations.

For a given ratio s_1/L_1 optimum resolution is obtained with maximum λ, i.e. with $\sqrt{2}\phi = 90°$; $\phi = 63.6°$. In this case, because $g = 0$, the image position is close to the exit boundary when the object distance L_1 is large in comparison with r_e.

In designing such an energy analyzer care must be taken that the image is formed outside the condenser, where the exit slit can be placed. From (2.24) and (2.23) one can deduce the condition for that to be the case

$$L_2 = \frac{L_1}{L_1/f - 1} > p. \tag{2.26}$$

This yields for the range $90° < \sqrt{2}\phi < 180°$ $(63.6° < \phi < 127.3°)$ the condition for the object distance from the entrance boundary $l_1 = L_1 - p$:

$$l_1 < -r_\mathrm{e} \frac{\tan\left(\sqrt{2}\phi\right)}{\sqrt{2}}. \tag{2.27}$$

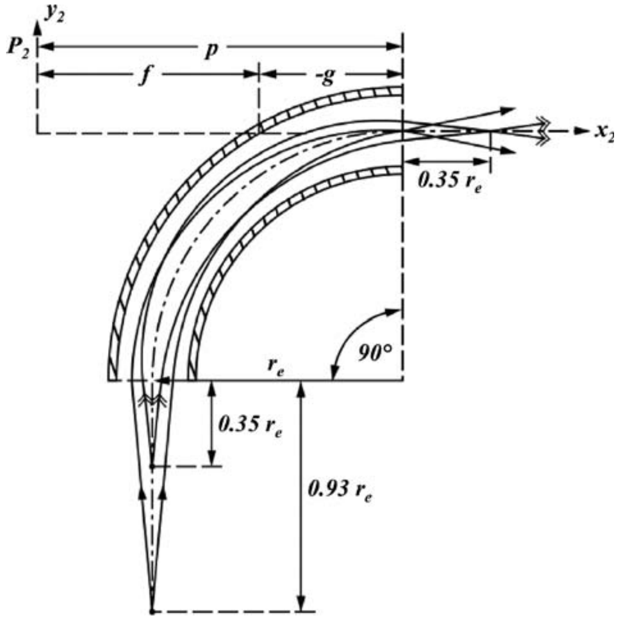

Fig. 2.6. Cylindrical condenser with 90° deflection angle

For example, with $\phi = 90°$ this yields $l_1 < 0.93\, r_\mathrm{e}$ (Fig. 2.6). If a larger l_1 were chosen the image would lie inside the field and no exit slit could be placed there.

When symmetric imaging is applied, we have

$$L_1 = L_2 = 2f \text{ and } l_1 = l_2 = g + f = r_\mathrm{e} \frac{1}{\sqrt{2}\tan\left(\phi/\sqrt{2}\right)}.$$

The distances l_1 and l_2 become zero for $\phi/\sqrt{2} = 90° \rightarrow \phi = 127.3°$. This is the well-known case of the 123.7° condenser (Fig. 2.7).

If (2.25) is used for the symmetric imaging case, one obtains, with $L_1 = 2f = r_\mathrm{e}\sqrt{2}/\sin\left(\sqrt{2}\phi\right)$ and $\lambda = \sin\left(\sqrt{2}\phi\right)/\sqrt{2}$, the theoretical energy resolution

$$\left(\frac{\Delta V}{V_0}\right)_\mathrm{th} = \frac{s_1}{r_\mathrm{e}}. \tag{2.28}$$

Note that this does not depend on the sector angle ϕ.

One important aspect in designing a sector field energy analyzer is the choice of the gap width d. It should be wide enough so that the selected beam does not hit the plates somewhere in the field. The plate spacing must therefore be wider than the largest beam width occurring in the field. Where the beam is widest, the trajectories are parallel

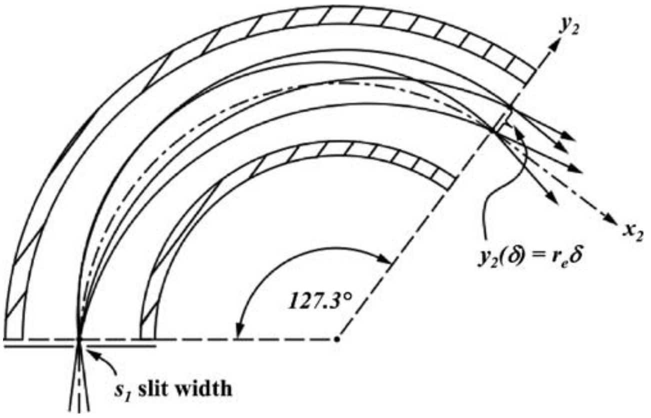

Fig. 2.7. Cylindrical condenser with 127.3° deflection angle

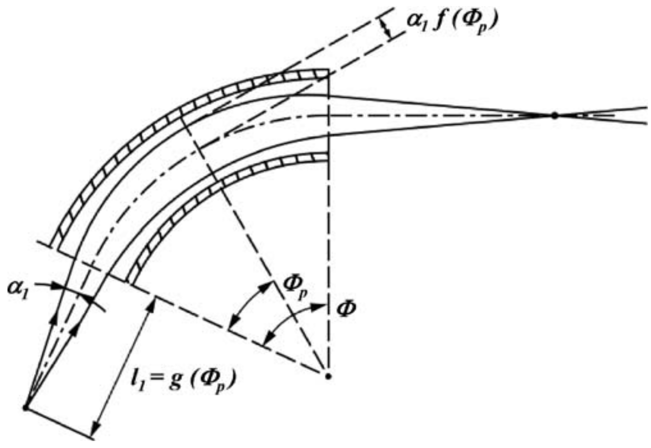

Fig. 2.8. Minimum gap width of cylindrical condenser

(Fig. 2.8). This occurs at a certain sector angle ϕ_{p}. We can consider this a separate sector field, for which we have

$$l_1 = g\left(\phi_{\mathrm{p}}\right) = \frac{r_{\mathrm{e}}}{\sqrt{2}\tan\left(\sqrt{2}\phi_{\mathrm{p}}\right)}. \tag{2.29}$$

From this the sector angle ϕ_{p} can be calculated, and then the focal length $f\left(\phi_{\mathrm{p}}\right) = r_{\mathrm{e}}/\sqrt{2}\sin\left(\sqrt{2}\phi_{\mathrm{p}}\right)$.

The largest trajectory distance from the optic axis is then $\alpha_1 f\left(\phi_p\right)$. In the z-direction there is no focusing in a cylindrical condenser.

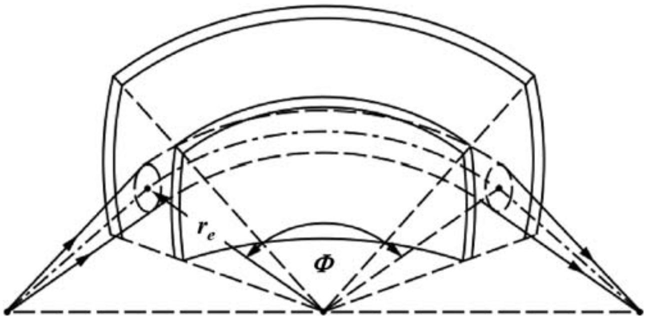

Fig. 2.9. Stigmatic focusing by spherical condenser

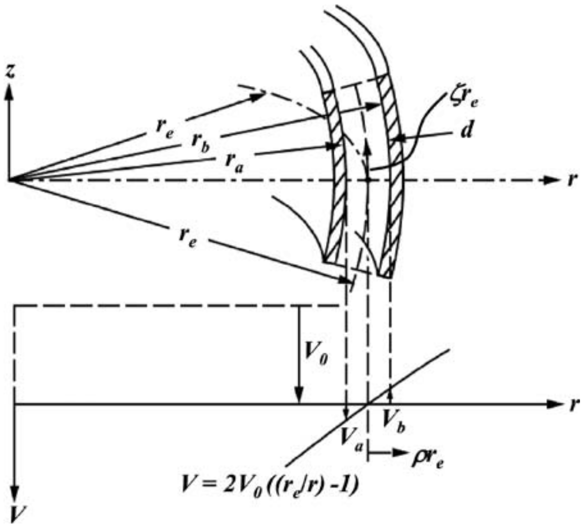

Fig. 2.10. Potential distribution in a spherical condenser. $V_{\mathrm{a}} = 2V_0\left((r_{\mathrm{e}}/r_{\mathrm{a}}) - 1\right)$, $V_b = 2V_0\left((r_{\mathrm{e}}/r_{\mathrm{b}} - 1)\right)$

2.3 Spherical Condenser

The lack of focusing in the z-direction with a cylindrical condenser often causes undesirable intensity losses. Therefore, spherical condensers are frequently used as energy spectrometers because they focus stigmatically like a round lens, but with a curved optic axis (Fig. 2.9) [12, 13].

Here the potential between the plates can be written to be (Fig. 2.10)

$$V\left(r\right) = 2V_0\left(\frac{r_{\mathrm{e}}}{r} - 1\right) \tag{2.30}$$

in a spherical coordinate system, and the radial field strength is

$$E\left(r\right)=-\frac{\mathrm{d}V\left(r\right)}{\mathrm{d}r}=2V_0\frac{r_{\mathrm{e}}}{r^2}. \tag{2.31}$$

For $r=r_{\mathrm{e}}$ this yields the desired field strength E_0 on the curved optic axis, which has to be the same as with the cylindrical condenser, $E_0=2V_0/r_{\mathrm{e}}$, (2.8). The particle energy in the field is $eV\left(r\right)=eV_0\left(2(r_{\mathrm{e}}/r)-1\right)$. Switching to the cylindrical coordinates $\rho=(r/r_{\mathrm{e}})-1$ and $\zeta=z/r_{\mathrm{e}}$ and developing the potential around $r=r_{\mathrm{e}}$ in a Taylor series in second approximation yields

$$V\left(\rho,\zeta\right)=2V_0\left(1-\rho+\rho^2-\frac{1}{2}\zeta^2+\cdots\right). \tag{2.32}$$

The Laplace equation, which can again be applied as a test, reads with these coordinates

$$\frac{\partial V^2}{\partial\rho^2}+\frac{\partial V}{\left(1+\rho\right)\partial\rho}+\frac{\partial^2 V}{\partial\zeta^2}=0. \tag{2.33}$$

The radial and axial components of the field strength $E_{\mathrm{r}}\left(\rho,\zeta\right)$ and $E_z\left(\rho,\zeta\right)$ are found by differentiation, with $2V_0/r_{\mathrm{e}}=E_0$, in first approximation:

$$E_{\mathrm{r}}=-\frac{\partial V}{r_{\mathrm{e}}\partial\rho}=E_0\left(1-2\rho+\cdots\right) \tag{2.34}$$

$$E_z=-\frac{\partial V}{r_{\mathrm{e}}\partial\zeta}=E_0\left(\zeta+\cdots\right). \tag{2.35}$$

The voltages against the middle potential to be applied to the plates (for negative particles) are here, again with $\rho_{\mathrm{a}}=-d/2r_{\mathrm{e}}$ and $\rho_{\mathrm{b}}=d/2r_{\mathrm{e}}$, in first approximation

$$\begin{aligned}V_{\mathrm{a}}&=V\left(\rho_{\mathrm{a}}\right)-2\,V_0=V_0\frac{d}{r_{\mathrm{e}}}\left(1+\frac{1}{2}\frac{d}{r_{\mathrm{e}}}\right),\\ V_{\mathrm{b}}&=V\left(\rho_{\mathrm{b}}\right)-2\,V_0=-V_0\frac{d}{r_{\mathrm{e}}}\left(1-\frac{1}{2}\frac{d}{r_{\mathrm{e}}}\right),\end{aligned} \tag{2.36}$$

and the deflection voltage across the plates is again $V_{\mathrm{d}}=V_{\mathrm{a}}-V_{\mathrm{b}}=2(d/r_{\mathrm{e}})V_0$.

The equations of motion are here in the r, z cylinder coordinate system

$$m\,\ddot{r} = m\,r\,\dot{\varphi}^2 - e\,E_r, \tag{2.37}$$

$$m\,r^2\dot{\varphi} = \text{const.}\,, \tag{2.38}$$

$$m\,\ddot{z} = -e\,E_z. \tag{2.39}$$

The solution of the differential equations is again an oscillation about the optic axis, this time not only radially but also in the z-direction. The period of the trajectories is here 2π for both directions. The sector field parameters result to be:

Radial and axial focal length

$$f_r = f_z = \frac{r_\mathrm{e}}{\sin\phi},$$

Energy dispersion factor

$$\lambda = \sin\phi.$$

Focal distance

$$g_r = g_z = r_\mathrm{e}\cot\phi,$$

Distance of principal planes from boundary

$$p_r = p_z = r_\mathrm{e}\tan\left(\phi/2\right).$$

The principal planes cross each other at the intersection of the entrance and exit axes (Fig. 2.11).

For the spherical condenser the image distance according to (2.24) can also be found very simply (Fig. 2.11): Object point, center point of the sector field and image point lie in a straight line.

The theoretical energy resolution according to (2.25) has its optimum for a given ratio s_1/L_1 with $\phi = 90° \rightarrow \lambda = 1$. It is better by a factor $\sqrt{2}$ than with the cylindrical condenser. With this sector angle, the object distance can be up to infinity before the image position is at the sector field exit.

In case of symmetric imaging, we have here $l_1 = l_2 = g + f = r_\mathrm{e}\cot\left(\phi/2\right)$ (Figs. 2.12 and 2.13). These distances become zero for $\phi = 180°$.

The energy resolution is for symmetric imaging, with (2.25) and

$$L_1 = 2f_r = \frac{2r_\mathrm{e}}{\sin\phi}, \quad \lambda = \sin\phi, \quad \left(\frac{\Delta V}{V_0}\right)_\mathrm{th} = \frac{s_1}{2r_\mathrm{e}}. \tag{2.40}$$

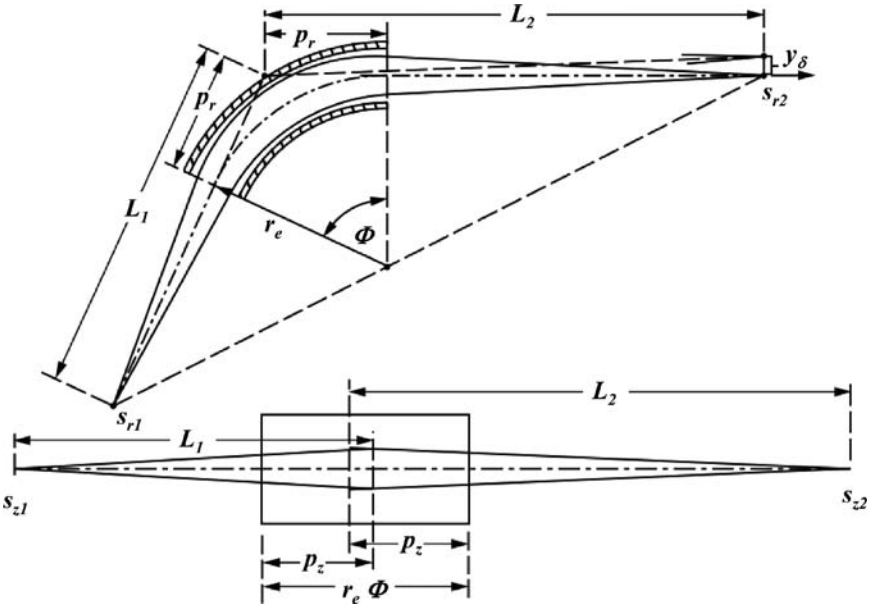

Fig. 2.11. Lens action of spherical condenser, radially and axially. Energy dispersion $y_\delta = L_2\delta$, $s_{r2} = (L_2/L_1)s_{r1}$, $s_{z2} = (L_2/L_1)s_{z1}$

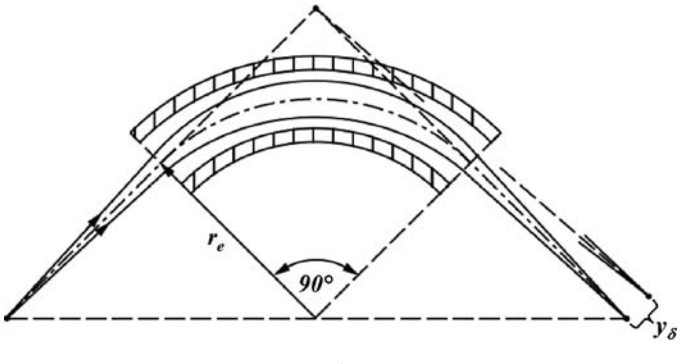

Fig. 2.12. Symmetric imaging with 90° spherical condenser. Energy dispersion $y_\delta = 2r_e\delta$

This is twice as good as for the cylindrical condenser (see (2.28)), compared on the basis of equal radius r_e. A fairer comparison would be on the basis of equal path length between object and image slit. If one calculates this, for example, with $\phi = 90°$, the improvement from cylindrical to spherical sector field is only a factor of 1.35.

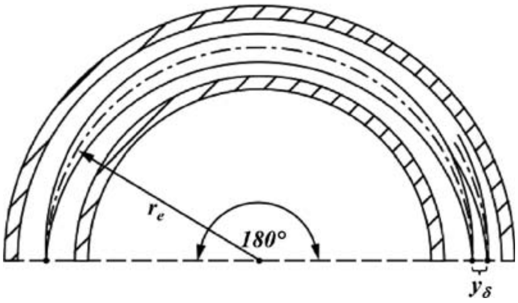

Fig. 2.13. Imaging with 180° spherical condenser. Energy dispersion $y_\delta = 2r_\mathrm{e}\delta$

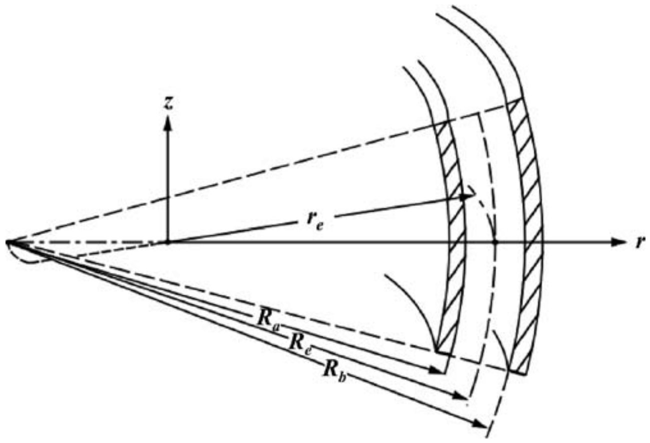

Fig. 2.14. Toroidal condenser, $r_\mathrm{e}/R_\mathrm{e} = c$

2.4 Toroidal Condenser

In most practical cases cylindrical or spherical condenser sector fields suffice for a given application. There are, however, rare cases were certain other imaging or dispersive properties are wanted which cannot be provided by the above sector fields.

A toroidal condenser (Fig. 2.14) has different radii of curvature r_e and R_e of the median equipotential surface in the *r*- and *z*-directions, and as a consequence different focusing properties in these directions.

We define the ratio of these radii as $c = r_\mathrm{e}/R_\mathrm{e}$. The potential around the optic axis can be written [14] (counted from the axis) to be

$$V(\rho, \zeta) = -2V_0 \left(\rho - \frac{1+c}{2}\rho^2 + \frac{c}{2}\zeta^2 + \cdots \right). \qquad (2.41)$$

The radial and axial field strength components, obtained by differentiation, are

$$E_r = E_0 \left[1 - (1+c)\,\rho + \cdots\right], \tag{2.42}$$

$$E_z = E_0 \left(c\zeta + \cdots\right) \tag{2.43}$$

The voltages to be applied to the plates are, from (2.41),

$$V_\mathrm{a} = V_0 \frac{d}{r_\mathrm{e}} \left(1 + \frac{1+c}{4} \frac{d}{r_\mathrm{e}}\right), \quad V_\mathrm{b} = -V_0 \frac{d}{r_\mathrm{e}} \left(1 - \frac{1+c}{4} \frac{d}{r_\mathrm{e}}\right). \tag{2.44}$$

The cylindrical ($c = 0$) and the spherical ($c = 1$) condenser can be considered special cases of this general toroidal condenser (comp. 2.12, 2.13, 2.32 and 2.34). The resulting field parameters are (comp. Fig. 2.4):

Radial focal length

$$f_r = \frac{r_\mathrm{e}}{\sqrt{2-c}\,\sin\left(\sqrt{2-c}\,\phi\right)},$$

Axial focal length

$$f_z = \frac{r_\mathrm{e}}{\sqrt{c}\,\sin\left(\sqrt{c}\,\phi\right)},$$

Radial focal distance

$$g_r = \frac{r_\mathrm{e} \cot\left(\sqrt{2-c}\,\phi\right)}{\sqrt{2-c}},$$

Axial focal distance

$$g_z = r_\mathrm{e} \frac{\cot\left(\sqrt{c}\,\phi\right)}{\sqrt{c}}, \tag{2.45}$$

Radial principal plane distance

$$p_r = f_r - g_r = \frac{r_\mathrm{e}}{\sqrt{2-c}} \tan\left(\frac{\sqrt{2-c}}{2}\phi\right),$$

Axial principal plane distance

$$p_z = f_z - g_z = \frac{r_\mathrm{e}}{\sqrt{c}} \tan\left(\frac{\sqrt{c}}{2}\phi\right),$$

Dispersion factor

$$\lambda = \frac{\sin\left(\sqrt{2-c}\,\phi\right)}{\sqrt{2-c}}.$$

For $0 < c < 1 (\infty > R_\mathrm{e} > r_\mathrm{e})$ the radial focusing is stronger than the axial one, while for $1 < c < 2 (r_\mathrm{e} > R_\mathrm{e} > r_\mathrm{e}/2)$ the axial focusing is stronger than the radial one.

In case of symmetric imaging we obtain with $L_1 = 2f_r$ from (2.25) the general expression for the energy resolution:

$$\left(\frac{\Delta V}{V_0}\right)_\mathrm{th} = \frac{s_1}{r_\mathrm{e}} \frac{2-c}{2}, \tag{2.46}$$

which includes (2.28) and (2.40). So for a given s_1/r_e, the energy resolution can be improved by letting c approach 2. This, however, goes at the expense of object to image distance along the optic axis. Further, the axial focusing has to be taken into account, so that the intensity is not lost by axial divergence of the beam.

There is a possibility to choose c in the favourable range $1 < c < 2$ [15] and still achieve stigmatic imaging in both directions. This is the case when an axial intermediate image is formed but no radial one. If one chooses symmetric imaging, the intermediate axial image is formed at half the sector angle. On the other hand, the object (or image) distance $l_{r1} (= l_{z1})$ of the full sector field is identical with the radial focal distance $g_{r1/2}$ of half the sector field. Using Newton's form of the axial imaging equation

$$\left(l_{z1} - g_{z1/2}\right)\left(l_{z2\,1/2} - g_{z1/2}\right) = f_{z1/2}^2,$$

we have therefore

$$\left(g_{r1/2} - g_{z1/2}\right)\left(-g_{z1/2}\right) = f_{z1/2}^2.$$

With the values from (2.45) this yields the condition

$$\sqrt{\frac{c}{2-c}} = -\tan\left(\frac{\sqrt{2-c}}{2}\phi\right)\tan\left(\frac{\sqrt{c}}{2}\phi\right). \tag{2.47}$$

For example, this condition is met with $\phi = 180°$ and $c = 1.69$ (Fig. 2.15). The other parameters are then $l_{r1} = 1.5 r_\mathrm{e}$, $p_r = 2.15 r_\mathrm{e}$, $f_r = 1.83 r_\mathrm{e}$, $\lambda = 1.77$.

The energy dispersion is a factor $1/(2-c) = 3.2$ higher than that of a spherical condenser with the same r_e, and therefore the energy resolution by the same factor better (comp. Fig. 2.13 with Fig. 2.15).

Other cases of stigmatically imaging toroidal sector fields are possible, namely when a radial but no axial intermediate image is

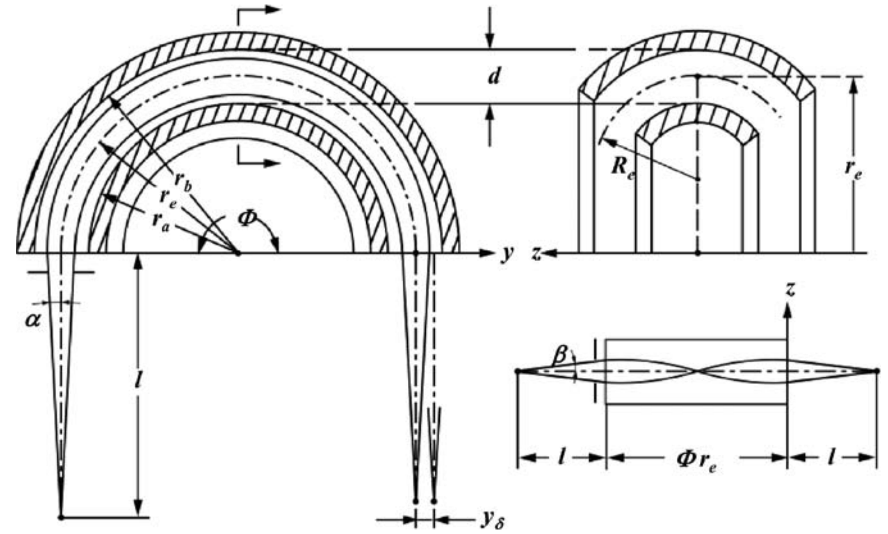

Fig. 2.15. Stigmatically imaging toroidal condenser with axial intermediate image. $\phi = 180°$, $R_\mathrm{e} = 0.59 r_\mathrm{e}$, $l = 1.5 r_\mathrm{e}$, $y_\delta = 6.45 r_\mathrm{e}\delta$

formed [16]. The condition for this to be the case for symmetric imaging is found to be

$$\sqrt{\frac{2-c}{c}} = -\tan\left(\frac{\sqrt{2-c}}{2}\phi\right)\tan\left(\frac{\sqrt{c}}{2}\phi\right). \qquad (2.48)$$

Such a sector field, however, has no use as an energy analyzer because the energy dispersion at the final image position is zero: the energy dispersion of the first half of the field is cancelled by the second half. There is, however, a very useful application: When a certain additional condition is met concerning the time-of-flight of ions from entrance to exit slit, a short pulse of ions formed with a small relative energy spread at the entrance slit arrives simultaneously at the exit slit. With this, we have a time-of-flight mass spectrometer with good mass resolution [17]. Figure. 2.16 shows a geometry which has been realized.

A special case of a toroidal condenser is when $c = 2$, $R_\mathrm{e} = r_\mathrm{e}/2$ (Fig. 2.17). Then the radial focal length f_r becomes infinite (see (2.45)), and there is focusing only in the axial direction. The dispersion factor becomes $\lambda = \phi$ (because $\sin\left(\sqrt{2-c}\phi\right) \rightarrow \sqrt{2-c}\phi$ for $\sqrt{2-c}\phi \rightarrow 0$). With (2.45) we have here:

Axial focal length

$$f_z = \frac{r_\mathrm{e}}{\sqrt{2}\sin\left(\sqrt{2}\phi\right)},$$

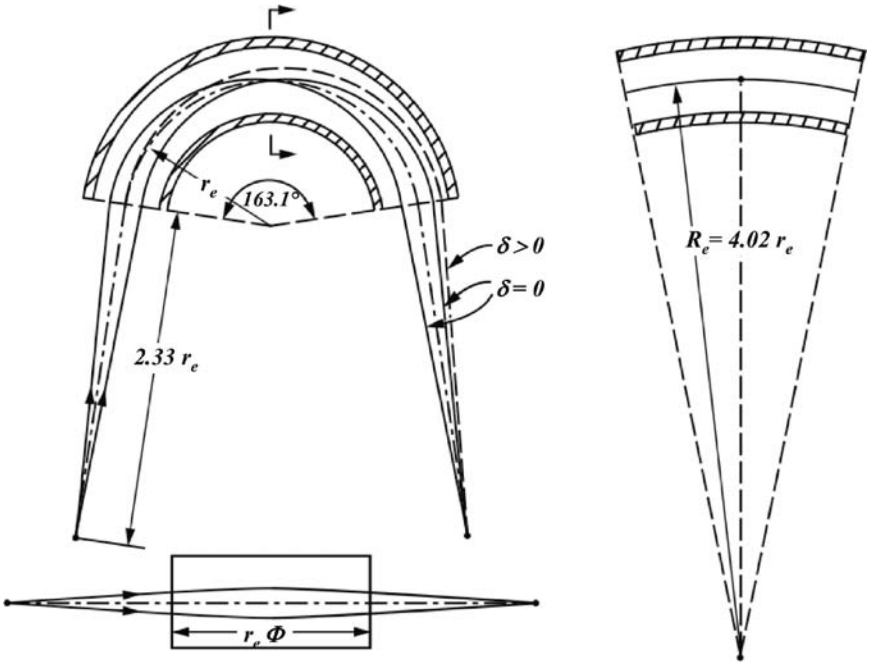

Fig. 2.16. Stigmatically imaging toroidal condenser with radial intermediate image, without energy dispersion, but with time-of-flight focusing

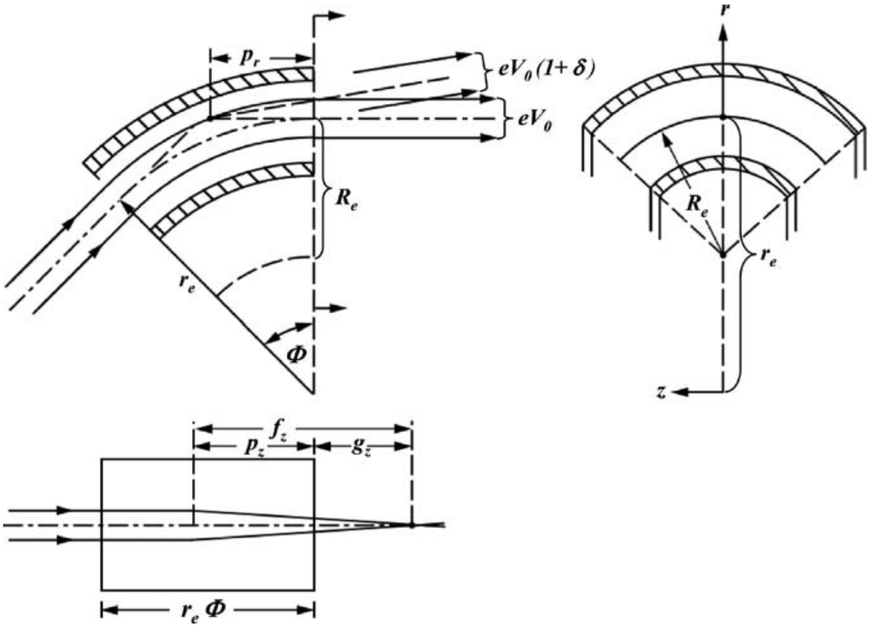

Fig. 2.17. Toroidal condenser with $R_\mathrm{e} = r_\mathrm{e}/2$ has no radial but strong axial focusing

Axial focal distance

$$g_z = r_{\mathrm{e}} \frac{\cot\left(\sqrt{2}\phi\right)}{\sqrt{2}},$$

Radial principal plane distance

$$p_r = r_{\mathrm{e}} \frac{\phi}{2}, \tag{2.49}$$

Axial principal plane distance

$$p_z = \frac{r_{\mathrm{e}}}{\sqrt{2}} \tan\left(\frac{\phi}{\sqrt{2}}\right),$$

Dispersion factor

$$\lambda = \phi.$$

Note that the axial lens parameters are the same as the radial ones for the cylindrical condenser ((2.20)–(2.23)). When such a sector field is to be used as an energy spectrometer, it has to be combined with a device focusing in the r-direction.

If the axial curvature is made even stronger ($c > 2, R_{\mathrm{e}} < r_{\mathrm{e}}/2$), the expression $\sqrt{2-c}$ in (2.45) becomes imaginary. The lens parameters, however, are still real and we have (with $\sqrt{2-c} = \mathrm{i}\sqrt{c-2}$, $\sin\left(\mathrm{i}\sqrt{c-2}\phi\right) = \mathrm{i}\sinh\sqrt{c-2}$, etc., $\mathrm{i}\cdot\mathrm{i} = -1$):

$$\begin{aligned} f_r &= \frac{-r_{\mathrm{e}}}{\sqrt{c-2}\sinh\left(\sqrt{c-2}\phi\right)}, & f_z &= \frac{r_{\mathrm{e}}}{\sqrt{c}\sin\left(\sqrt{c}\phi\right)}, \\ g_r &= -r_{\mathrm{e}}\frac{\coth\left(\sqrt{c-2}\phi\right)}{\sqrt{c-2}}, & g_z &= r_{\mathrm{e}}\frac{\cot\left(\sqrt{c}\phi\right)}{\sqrt{c}}, \\ p_r &= \frac{r_{\mathrm{e}}}{\sqrt{c-2}}\tanh\left(\frac{\sqrt{c-2}}{2}\phi\right), & p_z &= \frac{r_{\mathrm{e}}}{\sqrt{c}}\tan\left(\frac{\sqrt{c}}{2}\phi\right), \\ \lambda &= \frac{\sinh\left(\sqrt{c-2}\phi\right)}{\sqrt{c-2}}. \end{aligned} \tag{2.50}$$

Such a sector field acts radially as a diverging lens and axially as a strong focusing lens (Fig. 2.18).

Remembering the hyperbolic functions (Fig. 2.19), very large dispersion factors λ can be realized with such a sector field, e.g. with $c = 3$, $R_{\mathrm{e}} = r_{\mathrm{e}}/3$ and $\phi = 90°$ the dispersion factor is $\lambda = \sinh\phi = 2.3$. The strong axial focusing, however may be a hindrance.

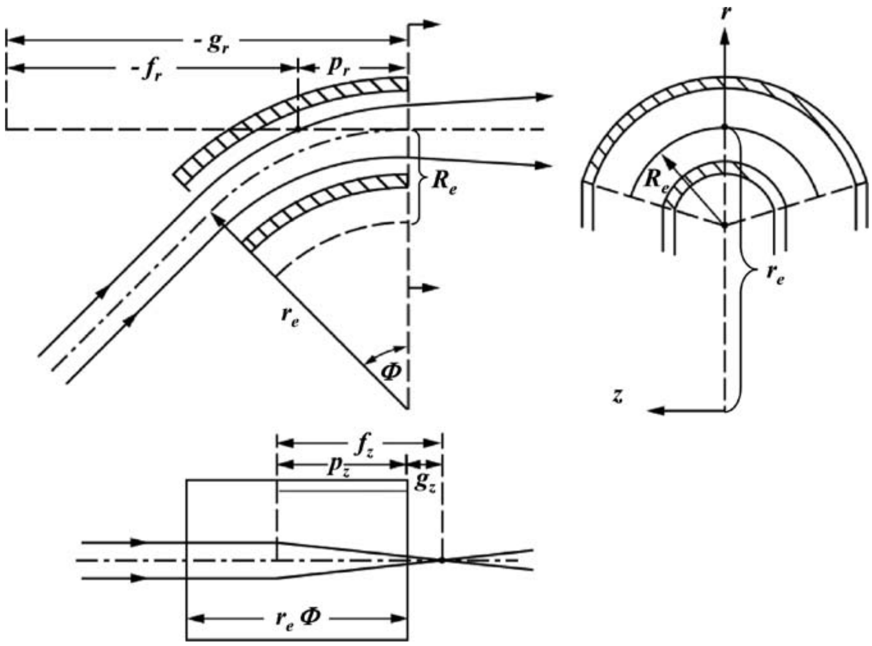

Fig. 2.18. Toroidal condenser with $R_e < r_e/2$ focuses axially but defocuses radially

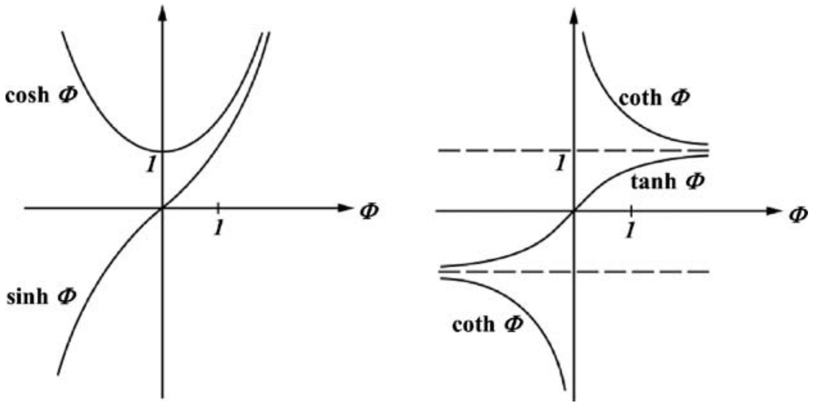

Fig. 2.19. The hyperbolic functions

Another class of toroidal condensers, which is also covered by (2.45), arises when the radial and axial curvatures are made opposite (Fig. 2.20). In this case the radius R_e is counted negative, so that c is negative.

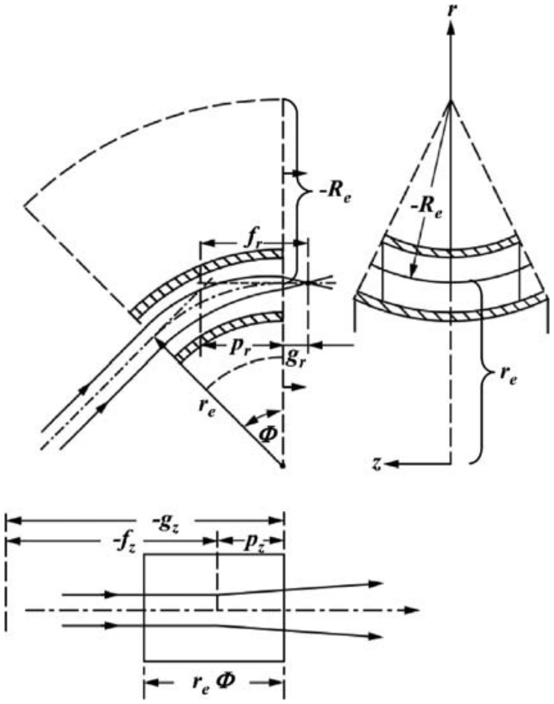

Fig. 2.20. Toroidal condenser with negative axial radius of curvature: strong radial focusing, but defocusing axially

The lens parameters are then

$$\begin{aligned}
f_r &= \frac{r_\mathrm{e}}{\sqrt{2-c}\,\sinh\left(\sqrt{2-c}\phi\right)}, & f_z &= \frac{-r_\mathrm{e}}{\sqrt{|c|}\,\sinh\left(\sqrt{|c|}\phi\right)}, \\
g_r &= r_\mathrm{e}\frac{\cot\left(\sqrt{2-c}\phi\right)}{\sqrt{2-c}}, & g_z &= -r_\mathrm{e}\frac{\coth\left(\sqrt{|c|}\phi\right)}{\sqrt{|c|}}, \\
p_r &= \frac{r_\mathrm{e}}{\sqrt{2-c}}\tan\left(\frac{\sqrt{2-c}}{c}\phi\right), & p_z &= \frac{r_\mathrm{e}}{\sqrt{|c|}}\tanh\left(\frac{\sqrt{|c|}}{2}\phi\right), \\
\lambda &= \frac{\sin\left(\sqrt{2-c}\phi\right)}{\sqrt{2-c}}.
\end{aligned} \tag{2.51}$$

These sector fields act radially as focusing lenses, but axially as diverging lenses.

3

Magnetic Deflection

Summary. Optical parameters and dispersive properties of magnetic sector fields are discussed.

When a singly charged particle of energy eV enters a uniform magnetic field B oriented transversely to the particle trajectory, it experiences the deflecting Lorentz force $F_{\mathrm{L}} = evB$, which is counterbalanced by the centrifugal force $F_{\mathrm{c}} = mv^2/r$, where v is the particle velocity and m its mass:

$$\frac{mv^2}{r} = evB, \quad \frac{mv}{r} = eB. \tag{3.1}$$

With $mv^2/2 = eV$, $mv = \sqrt{2emV}$ this yields

$$rB = \sqrt{2mV/e} \text{ or } rB = 143.6\sqrt{MV} \tag{3.2}$$

with r [cm], B [G], M [dalton], V [V] (Fig. 3.1).

Another form is $rB = 0.454\sqrt{MV}$, with r [cm], B [T], M [dalton], V [kV]. For electrons (with $M = 1/1,823$ dalton) we have

$$rB = 3.35\sqrt{V} \tag{3.3}$$

with r [cm], B [G], V [V]. Multiply charged ions with n elementary charges are deflected as if they had the mass M/n, if they have been accelerated by the same voltage V as singly charged ions.

3.1 Small Deflection Angles

Small deflection angles ϕ are obtained from $\phi \approx L/r$, where L is the length of the field and r is obtained from (3.2) or (3.3). The deflection

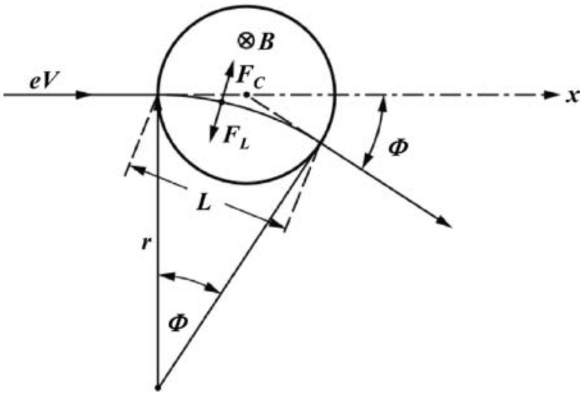

Fig. 3.1. Magnetic deflection of charged particles

at the end of the field is (cosine developed as power series) $y\,(L) = r\,(1-\cos\phi) \approx r\phi^2/2 = L^2/2r$. The center of deflection is situated at the distance $y\,(L)/\phi = L/2$ from the end of the field, i.e. in the middle of the field (comp. Fig. 2.1). Since the deflection depends on the mass and the energy (see (3.2)) one can define a mass and energy dispersion coefficient. Inserting a slightly different mass $M_1 = M_0\,(1+\gamma)$ and energy $V_1 = V_0\,(1+\delta)$ into (3.2) and developing it into a power series, one obtains in first order

$$\begin{aligned} r_1 &= \frac{143.6}{B}\sqrt{M_1V_1} = \frac{143.6}{B}\sqrt{M_0\,(1+\gamma)\,V_0\,(1+\delta)} \\ &= \frac{143.6}{B}\sqrt{M_0V_0}\left(1+\frac{\gamma}{2}+\frac{\delta}{2}\right). \end{aligned}$$

This yields

$$r_1 = r_0\left(1+\frac{\gamma}{2}+\frac{\delta}{2}\right)$$

and

$$\phi_1 = \frac{L}{r_1} = \frac{L}{r_0}\left(1-\frac{\gamma}{2}-\frac{\delta}{2}\right).$$

Therefore,

$$\phi_1 - \phi_0 = \Delta\phi = -\frac{1}{2}\phi_0\,(\gamma+\delta)\,. \tag{3.4}$$

The dispersion factor is thus $\phi_0/2$ both for mass and energy. Note that the energy dispersion factor is half of that of an electrostatic field (comp. (2.7)). Magnetic deflection fields are used mostly for their mass dispersion in ion physics, and then larger deflection angles are common for their larger mass dispersion.

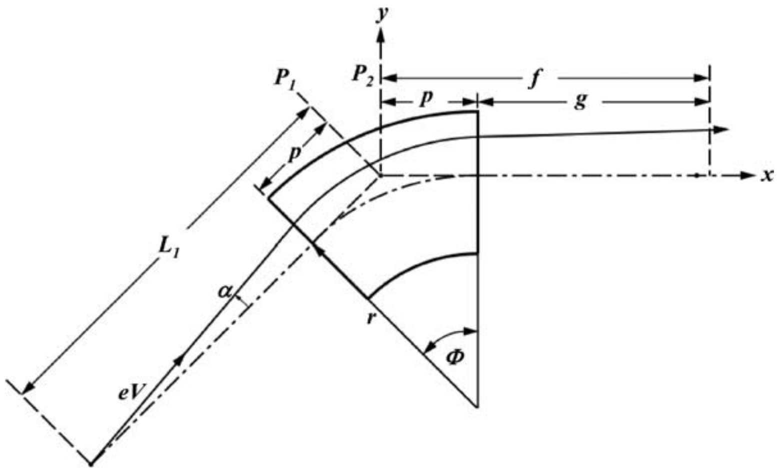

Fig. 3.2. Optical parameters of uniform magnetic sector field

3.2 Magnetic Sector Fields

A magnetic sector field is usually shaped after the contour of the beam passing through it in order to save magnetic volume (Fig. 3.2). The optic axis has three parts: the straight entrance axis perpendicular to the field boundary, the curved axis inside the field followed by a particle with mass M_0 and energy eV_0 entering on the entrance axis, and the straight exit axis perpendicular to the exit boundary.

In a uniform magnetic sector field a paraxial trajectory can be calculated simply trigonometrically, in contrast to the electrostatic sector field, because the particle energy stays the same and hence also the radius of the trajectory. Its exit equation results to be

$$y = L_1\alpha + x\left[\left(1 - \frac{L_1}{f}\right)\alpha + \nu\,(\gamma + \delta)\right]. \tag{3.5}$$

Similar to an electrostatic sector field, a magnetic sector field combines focusing with dispersive properties, characterized by the two terms in the parenthesis. The dispersion term comprises the sum $\gamma + \delta$. This means that a particle is deflected the same way whether it has a certain mass deviation or the same relative energy deviation. If they are equal but opposite, no dispersion occurs.

The two principal planes P_1 and P_2 are rotated by the sector angle ϕ about the intersection of the entrance and exit optic axes. The transfer matrix from P_1 and P_2 is

$$\begin{pmatrix} y_2 \\ y_2' \\ \gamma + \delta \end{pmatrix} = \begin{pmatrix} 1 & 0 & 0 \\ -\frac{1}{f} & 1 & \gamma \\ 0 & 0 & 1 \end{pmatrix} \begin{pmatrix} y_1 \\ y_1' \\ \gamma + \delta \end{pmatrix} \tag{3.6}$$

with $L_1\alpha = y_1$, $\alpha = y_1'$. The parameters of the uniform magnetic sector field are:

Focal length

$$f = \frac{r}{\sin\phi} \ ,$$

dispersion factor

$$\nu = \frac{1}{2}\sin\phi \ , \tag{3.7}$$

focal distance (from field boundary)

$$g = r\cot\phi \ ,$$

distance of principal planes from field boundary

$$p = r\tan\frac{\phi}{2}.$$

From (3.5) the imaging equation can be deduced, with $x = L_2$ (image distance) for $y = 0$ and $\gamma = \delta = 0$:

$$L_2 = \frac{L_1}{L_1/f - 1}. \tag{3.8}$$

A real image is formed ($L_2 > 0$), when $L_1 > f$. The magnification equals L_2/L_1. The image position can be found geometrically by Barber's construction (Fig. 3.3): object point, sector center and image point lie in a straight line. This is also true for virtual objects and images (Figs. 3.4–3.7).

The most common application of magnetic sector fields is for mass separation or mass spectrometry. In order to express the mass resolution of a magnetic sector field, the image width of an entrance slit placed at the object position has to be compared with the mass dispersion. The mass dispersion in the image plane is, from (3.5),

$$y_\gamma = L_2\nu\gamma, \tag{3.9}$$

where $\gamma = \Delta M/M$ is the relative mass difference. The width of the image of the entrance slit is $s_2 = s_1 L_2/L_1$. This would be due to ions with the energy eV_0. Because of the unavoidable energy spread of the ions, the energy dispersion in the image plane has to be added, which

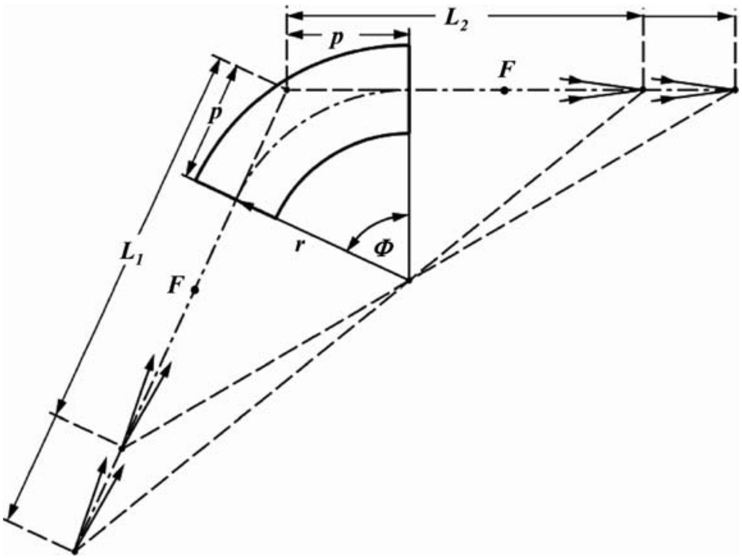

Fig. 3.3. Barber's construction with real object and image points outside the field ($L_1 > 0; L_2 > 0$)

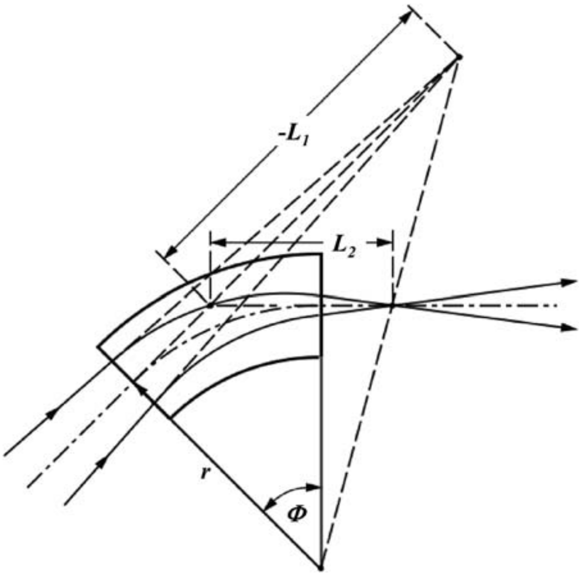

Fig. 3.4. Barber's construction with virtual object point ($L_1 < 0$) and image point outside the field ($L_2 > p$)

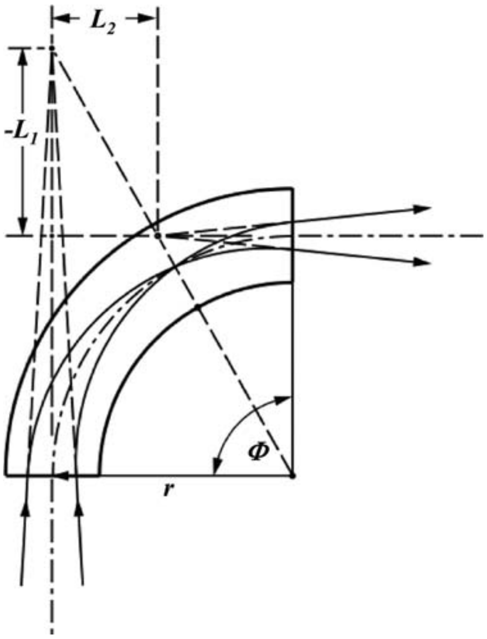

Fig. 3.5. Barber's construction with virtual object point ($L_1 < 0$) and image point inside the field ($L_2 < p$)

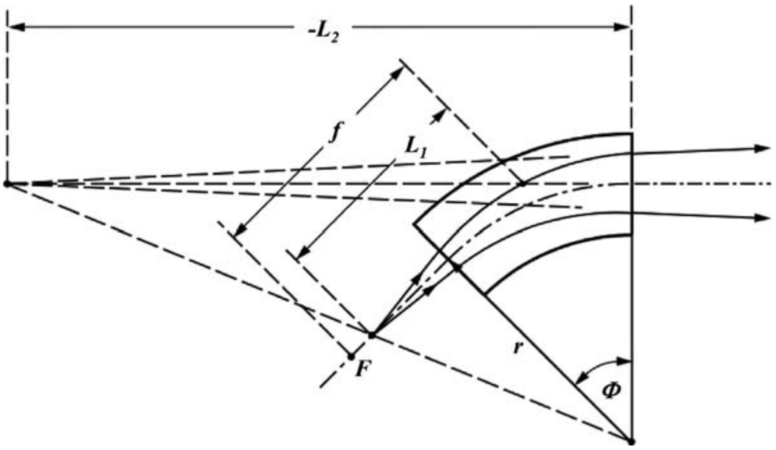

Fig. 3.6. Barber's construction with real object point ($L_1 < f$) and virtual image point ($L_2 < 0$)

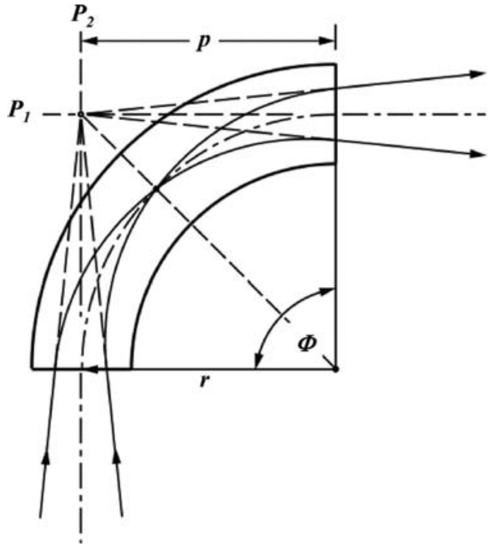

Fig. 3.7. Barber's construction with $L_1 = L_2 = 0$

is, in analogy to (3.9), $y_\delta = L_2 \nu \delta$, where $\delta = \Delta V / V_0$ is the relative energy spread of the ions. The total image width is thus

$$w = s_2 + y_\delta = (s_1/L_1 + \nu\delta)\, L_2 . \tag{3.10}$$

An exit slit is placed in the image plane, which for intensity reasons should have the width w. The theoretical mass resolution is given when the image width w equals the mass dispersion

$$(s_1/L_1 + \nu\delta)\, L_2 = L_2 \nu \gamma, \qquad \left(\frac{\Delta M}{M}\right)_{\text{th}} = \frac{s_1}{L_1 \nu} + \delta . \tag{3.11}$$

This relation shows that the relative energy spread principally limits the achievable mass resolution. For a given energy spread ΔV it can only be improved by increasing the acceleration voltage, which in turn requires a higher magnetic field.

When symmetric imaging is employed ($L_1 = L_2 = L = 2f$), we have, with (3.7), $L_1 \nu = r$, so that

$$\left(\frac{\Delta M}{M}\right)_{\text{th}} = \frac{s_1}{r} + \delta . \tag{3.12}$$

Note that this does not depend on the sector angle ϕ. With decreasing ϕ, however, the distance from the boundaries $L - p = g + f = r \cot(\phi/2)$

becomes larger and hence the solid angle accepted by a certain aperture diameter becomes smaller.

3.3 Axial Focusing with Uniform Magnetic Sector Field

A uniform magnetic sector field as described in the previous section, has dispersing and focusing properties only parallel to the plane defined by the curved optic axis, in analogy to the cylindrical condenser. In order to achieve focusing action also normal to that plane (parallel to the axis of rotation), oblique field boundaries are frequently used [18,19]. When the field boundary normal includes an angle ε with the entrance or exit optic axis (Fig. 3.8), there is a field component B_ε acting parallel to the plane of the optic axis and normal to the trajectory, thus resulting in a deflecting force normal to the plane of the optic axis. As a consequence, the fringe field acts as a thin lens focusing normal to the plane of symmetry with the first-order focal length

$$f_\varepsilon = r \cot \varepsilon. \tag{3.13}$$

It can be positive or negative, depending on the sign of ε. Figure 3.8 shows a positive ε. Oblique field boundaries, however, have an effect

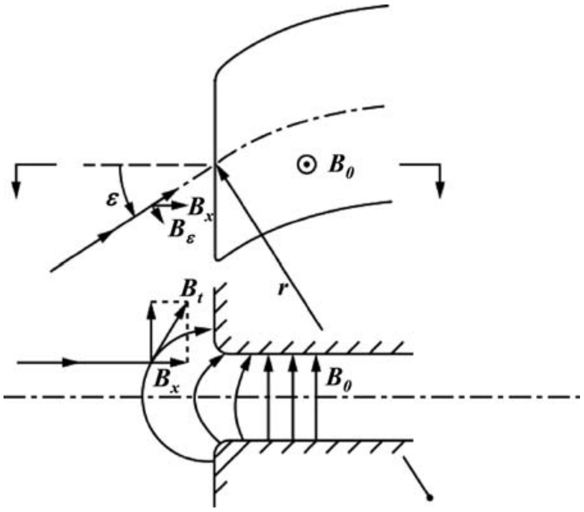

Fig. 3.8. Axial focusing by fringe field of oblique field boundary. Component B_x of field line tangent B_t is split up into one component along trajectory and another perpendicular to it, B_ε. Component B_ε exerts a focusing force towards the plane of the optic axis

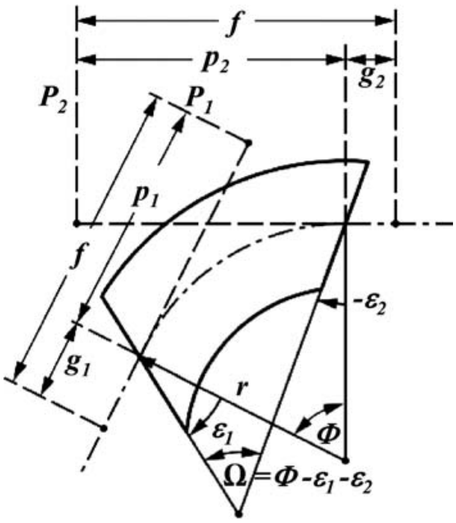

Fig. 3.9. Optical parameters of uniform magnetic sector field with oblique boundaries

also on the radial focusing of a uniform magnetic sector field. When one of the fringe fields acts as a converging lens in the axial direction (ε positive) the radial focusing action is weaker. When a fringe field acts as a diverging lens (negative ε), the radial focusing is stronger. The following are the focusing parameters for the general case (Fig. 3.9).

$$\begin{aligned} f &= r\frac{\cos\varepsilon_1\cos\varepsilon_2}{\sin\Omega}, \\ g_1 &= r\frac{\cos\varepsilon_1\cos(\phi-\varepsilon_2)}{\sin\Omega}, \quad g_2 = r\frac{\cos\varepsilon_2\cos(\phi-\varepsilon_1)}{\sin\Omega}, \\ p_1 &= f - g_1 = r\frac{\cos\varepsilon_1}{\sin\Omega}\left[\cos\varepsilon_2 - \cos(\phi-\varepsilon_2)\right], \\ p_2 &= f - g_2 = r\frac{\cos\varepsilon_2}{\sin\Omega}\left[\cos\varepsilon_1 - \cos(\phi-\varepsilon_1)\right]. \end{aligned} \tag{3.14}$$

With the above value of f, (3.5) and (3.8) apply. The center of mass and energy dispersion is at the distance p_ν from the exit boundary, which is here different from p_2 (with normal boundaries it is the same) (Fig. 3.10):

$$p_\nu = \frac{r}{\cot(\phi/2) + \tan\varepsilon_2}. \tag{3.15}$$

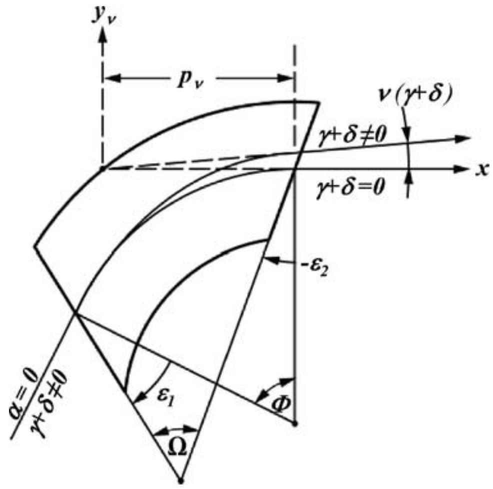

Fig. 3.10. Center of dispersion of uniform magnetic sector field with oblique boundaries

The trajectory equation behind the field in the $x-y_\nu$ coordinate system is

$$y_\nu = x\nu\,(\gamma+\delta) \tag{3.16}$$

with the dispersion factor

$$\nu = \frac{1}{2}\left[\sin\phi + (1-\cos\phi)\tan\varepsilon_2\right]. \tag{3.17}$$

In the special case where the field boundaries are parallel ($\Omega = 0$, $\varepsilon_1+\varepsilon_2=\phi$), there is no radial focusing ($f=\infty$, see (3.14)), but always axial focusing (Fig. 3.11).

With an example the application of fringe field focusing is demonstrated, viz. a symmetric stigmatic imaging mass separator with $\varepsilon_1 = \varepsilon_2 = \varepsilon$ (Fig. 3.12). In the middle of the sector field (at $\phi/2$), the beam must be parallel both radially and axially. Thus, considering one half of the sector field, we have $f_\varepsilon = g\,(\phi/2)$; with (3.13 and 3.14) we obtain

$$\cot\varepsilon = \frac{\cos\varepsilon\cos(\phi/2)}{\sin(\phi/2-\varepsilon)}, \quad \frac{\sin(\phi/2-\varepsilon)}{\cos(\phi/2)} = \sin\varepsilon,$$

$$\tan\frac{\phi}{2}\cos\varepsilon - \sin\varepsilon = \sin\varepsilon,$$

$$\tan\varepsilon = \frac{1}{2}\tan\frac{\phi}{2}. \tag{3.18}$$

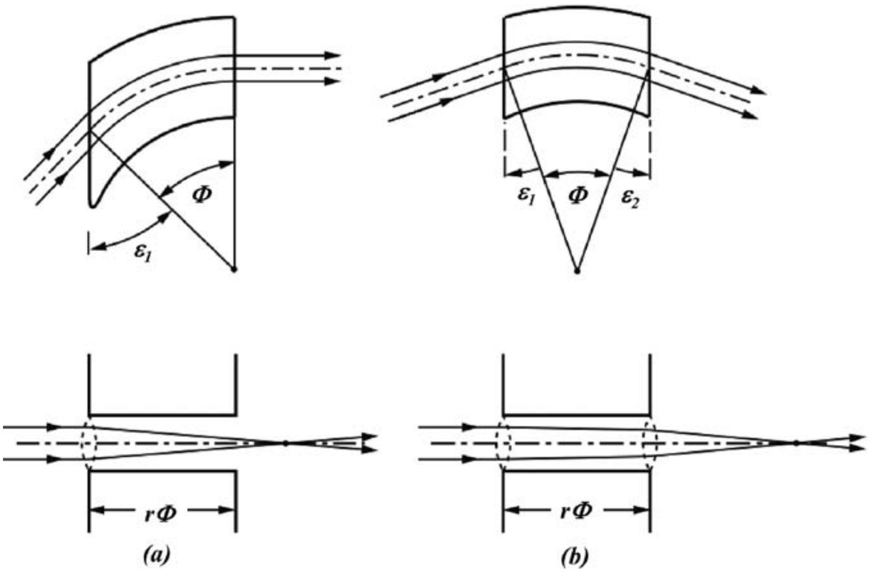

(a) (b)

Fig. 3.11. Parallel field boundaries: no radial, but axial focusing, (**a**) $\epsilon_1 = \phi, \epsilon_2 = 0$, (**b**) $\epsilon_1 = \epsilon_2 = \phi/2$

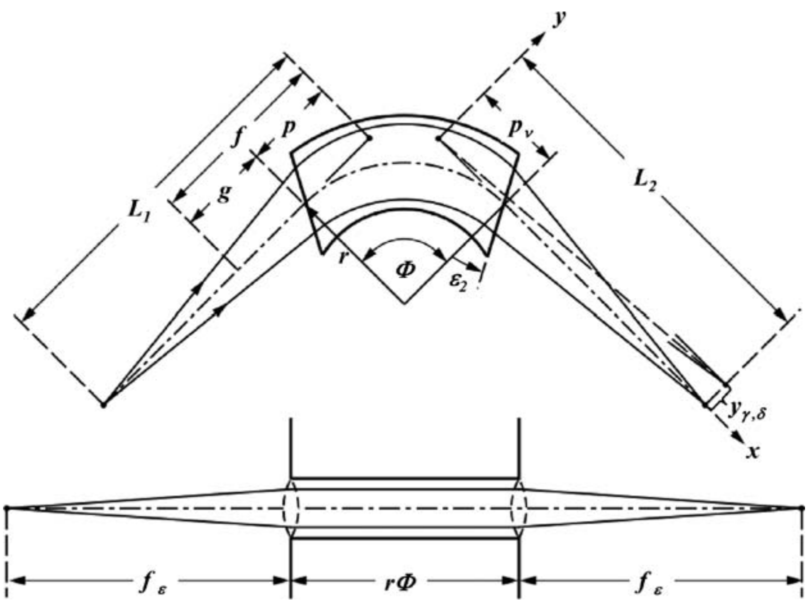

Fig. 3.12. Symmetric stigmatic imaging by fringe field focusing, $L_1 = L_2$

This is the relation between ε and ϕ which must be met. With $\phi = 90°$ one obtains $\tan \epsilon = 0.5$, $\varepsilon = 26.6°$, $f_\varepsilon = 2r$, $f = (4/3)r$, $g = (2/3)r$, $p = (2/3)r$, $L = 2f = (8/3)r$.

The deflection center for the mass dispersion is at the distance $p_\nu = (2/3)r$ from the exit, the same as p, the distance of the principal plane. Further we have $\nu = 3/4$ and the dispersion at the image plane

$$y_{\gamma,\delta} = L\nu\left(\gamma + \delta\right) = 2r\left(\gamma + \delta\right). \tag{3.19}$$

This is twice as much as with a uniform sector field with normal boundaries having the same mean deflection radius r. The mass resolution is obtained (see. (3.11)) to be

$$\left(\frac{\Delta M}{M}\right)_{\mathrm{th}} = \frac{s_1}{2r} + \delta. \tag{3.20}$$

This is better than in the case of normal boundaries (comp. (3.12)), but at the expense of longer distances of source and image from the sector field.

3.4 Non-Uniform Magnetic Sector Fields

Another way to achieve focusing also in the axial direction, but without axial fringe field focusing, is to use sector fields which are radially non-uniform [20–23].

When the pole piece surfaces of the sector magnet are not parallel but conical (Fig. 3.13) so that in a cross section in a plane through z their tangents intersect at a radial distance R_{m} from the optic axis, a coefficient of non-uniformity can be defined:

$$n = \frac{r_{\mathrm{m}}}{R_{\mathrm{m}}}, \tag{3.21}$$

r_{m} being the radius of the circularly curved optic axis inside the field. With B_0 being the field strength on the optic axis, the off-axis field can be described by its axial and radial components (in first-order approximation):

$$B_z\left(r, z\right) = B_0\left(1 - n\rho + \cdots\right), \tag{3.22}$$

$$B_r\left(r, z\right) = B_0\left(-n\zeta + \cdots\right). \tag{3.23}$$

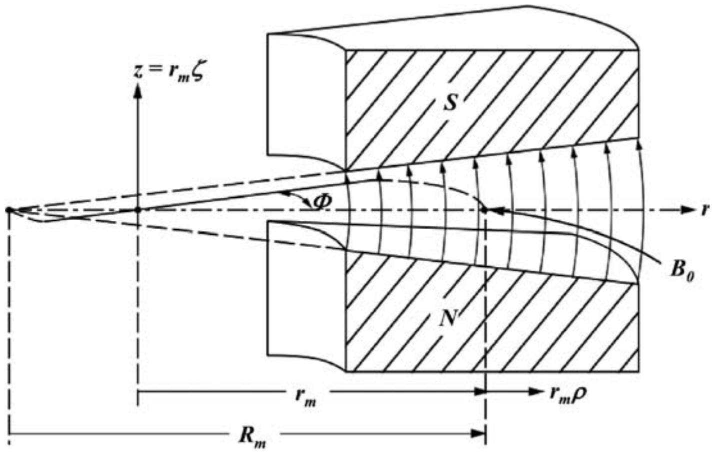

Fig. 3.13. Non-uniform magnetic sector field

The optical parameters of such a field are (comp. Fig. 3.2):

$$f_r = \frac{r_\mathrm{m}}{\sqrt{1-n}\sin\left(\sqrt{1-n}\phi\right)} \qquad \text{radial focal length} \tag{3.24a}$$

$$g_r = \frac{r_\mathrm{m}}{\sqrt{1-n}\tan\left(\sqrt{1-n}\phi\right)} \qquad \text{radial focal distance} \tag{3.24b}$$

$$p_r = f_r - g_r = \frac{r_\mathrm{m}}{\sqrt{1-n}}\tan\left(\sqrt{1-n}\phi/2\right) \qquad \text{distance of radial principal plane} \tag{3.24c}$$

$$\nu = \frac{\sin\left(\sqrt{1-n}\phi\right)}{2\sqrt{1-n}} \qquad \text{dispersion factor} \tag{3.24d}$$

$$p_\nu = p_r \qquad \text{distance of dispersion center} \tag{3.24e}$$

$$f_z = \frac{r_\mathrm{m}}{\sqrt{n}\sin\left(\sqrt{n}\phi\right)} \qquad \text{axial focal length} \tag{3.24f}$$

$$g_z = \frac{r_\mathrm{m}}{\sqrt{n}\tan\left(\sqrt{n}\phi\right)} \qquad \text{axial focal distance} \tag{3.24g}$$

$$p_z = f_z - g_z = \frac{r_\mathrm{m}}{\sqrt{n}}\tan\left(\sqrt{n}\phi/2\right) \qquad \text{distance of axial principal plane} \tag{3.24h}$$

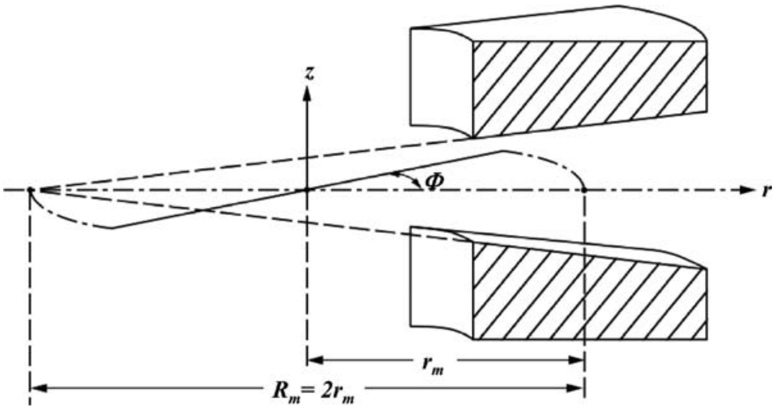

Fig. 3.14. Special case of non-uniform magnetic sector field: $R_\mathrm{m} = 2r_\mathrm{m}$

In the special case when $n = 1/2\,(R_\mathrm{m} = 2r_\mathrm{m})$ (Fig. 3.14), the radial and axial parameters become equal so that stigmatic imaging occurs:

$$\begin{aligned} f_r &= f_z = r_\mathrm{m}\frac{\sqrt{2}}{\sin\left(\phi/\sqrt{2}\right)}\,, \\ g_r &= g_z = r_\mathrm{m}\sqrt{2}\cot\left(\phi/\sqrt{2}\right)\,, \\ p_r &= p_z = r_\mathrm{m}\sqrt{2}\tan\left(\phi/2\sqrt{2}\right)\,, \\ \nu &= \frac{1}{\sqrt{2}}\sin\left(\phi/\sqrt{2}\right)\,. \end{aligned} \tag{3.25}$$

In case of symmetric imaging the source and image distance becomes

$$l = r_\mathrm{m}\sqrt{2}\frac{1+\cos\left(\phi/\sqrt{2}\right)}{\sin\left(\phi/\sqrt{2}\right)} = r_\mathrm{m}\sqrt{2}\cot\left(\phi/2\sqrt{2}\right)\,. \tag{3.26}$$

Two examples are shown in Figs. 3.15 and 3.16. The dispersion in the image plane is

$$y_{\gamma,\delta} = 2f\nu\,(\gamma+\delta) = 2r_\mathrm{m}\,(\gamma+\delta)\,, \tag{3.27}$$

independent of the sector angle ϕ. Note that this is the same as in the previous example of stigmatic imaging with fringe field focusing and $\phi = 90°$ ((3.19)).

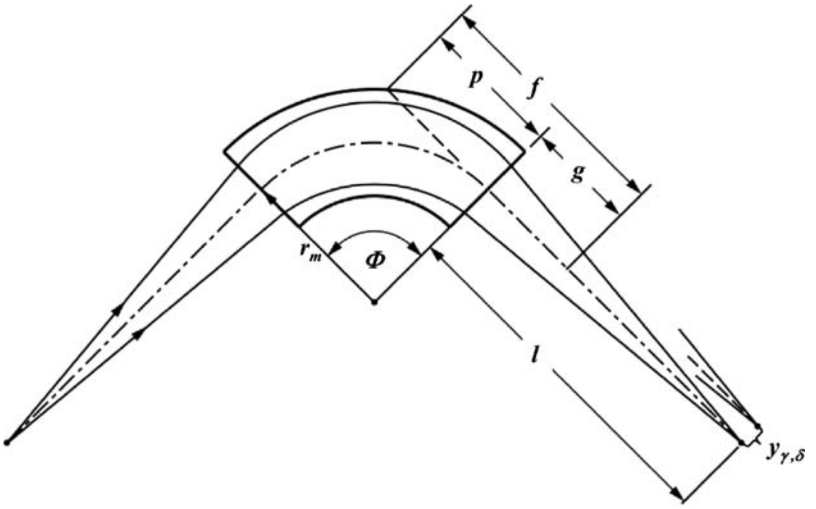

Fig. 3.15. Symmetric stigmatic imaging by non-uniform magnetic sector field with $R_\mathrm{m} = 2r_\mathrm{m}$. Example: $\phi = 90°; f = 1.58\,r_\mathrm{m}; p = 0.88\,r_\mathrm{m}; g = 0.70\,r_\mathrm{m}; l = 2.28\,r_\mathrm{m}$. Dispersion $y_{\gamma,\delta} = 2r_\mathrm{m}\,(\gamma + \delta)$

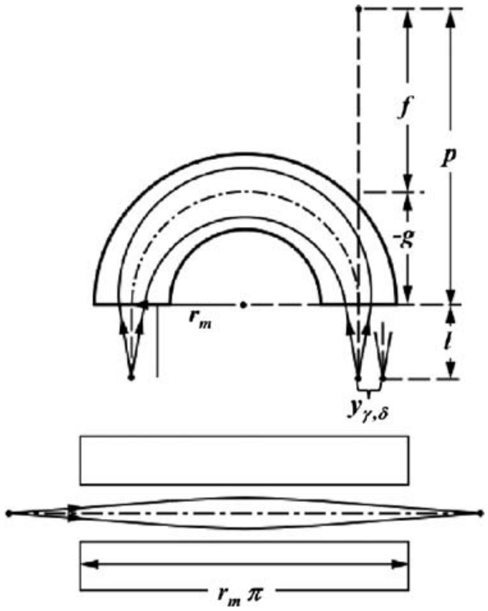

Fig. 3.16. Symmetric stigmatic imaging by non-uniform magnetic sector field with $\phi = 180°; f = 1.78\,r_\mathrm{m}; p = 2.85\,r_\mathrm{m}; g = -1.08\,r_\mathrm{m}; l = 0.70\,r_\mathrm{m}$. Dispersion $y_{\gamma,\delta} = 2r_\mathrm{m}\,(\gamma + \delta)$

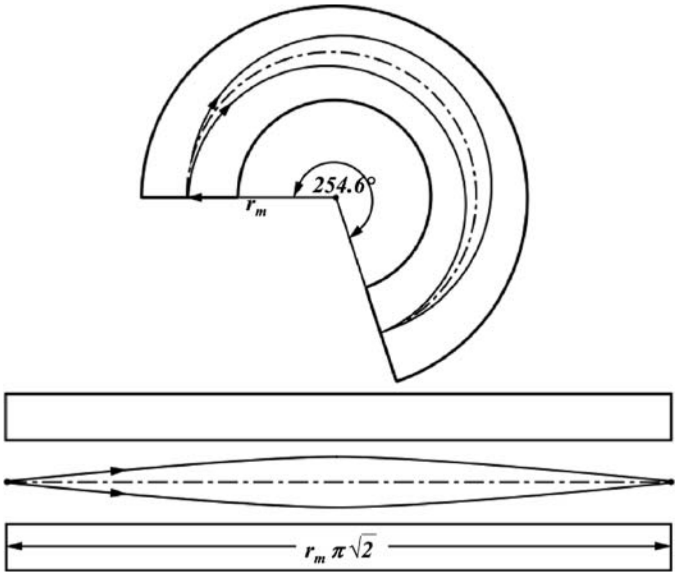

Fig. 3.17. Stigmatic imaging by non-uniform magnetic sector field from entrance to exit boundary

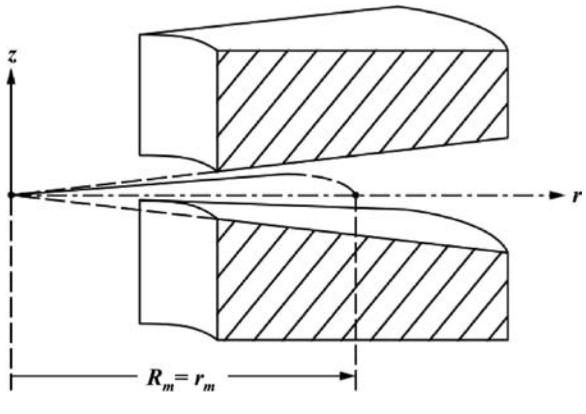

Fig. 3.18. Non-uniform magnetic sector field with $R_\mathrm{m} = r_\mathrm{m}$

The object and image distance becomes zero with (see (3.26)) $\phi = 2\sqrt{2} \times 90^\circ = 254.6^\circ$ (Fig. 3.17). Another special case is when $n = 1$ ($R_\mathrm{m} = r_\mathrm{m}$) (compare the toroidal field case with $c = 2$) (Fig. 3.18).

In this case the radius of curvature of a particle trajectory equals the distance from the z-origin, there is no radial focusing, only axial focusing (Fig. 3.19).

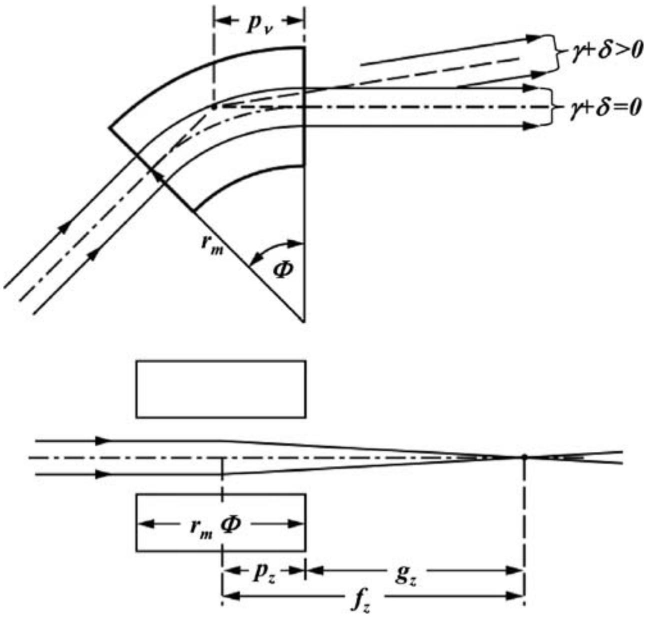

Fig. 3.19. Non-uniform magnetic sector field with $R_\mathrm{m} = r_\mathrm{m}$: no radial focusing, but axial focusing

The optical parameters are

$$
\begin{aligned}
&f_r = \infty,\ g_r = \infty,\ f_z = \frac{r_\mathrm{m}}{\sin\phi},\ g_z = r_\mathrm{m}\cot\phi, \\
&p_z = p_\nu = r_\mathrm{m}\tan\left(\frac{\phi}{2}\right),\ \nu = \phi/2. \qquad (3.28)
\end{aligned}
$$

In case $n > 1 \quad (R_\mathrm{m} < r_\mathrm{m})$ (Fig. 3.20) the expression $\sqrt{1-n}$ in (3.24) becomes imaginary. (Comp. case $c > 2$).

The lens parameters, however, are again still real:

$$
\begin{aligned}
f_r &= \frac{-r_\mathrm{m}}{\sqrt{n-1}\sinh\left(\sqrt{n-1}\phi\right)}, \\
g_r &= \frac{-r_\mathrm{m}}{\sqrt{n-1}\tanh\left(\sqrt{n-1}\phi\right)}, \\
p_r = p_\nu &= \frac{r_\mathrm{m}}{\sqrt{n-1}}\tanh\left(\sqrt{n-1}\phi/2\right), \\
\nu &= \frac{\sinh\left(\sqrt{n-1}\phi\right)}{2\sqrt{n-1}}.
\end{aligned}
\qquad (3.29)
$$

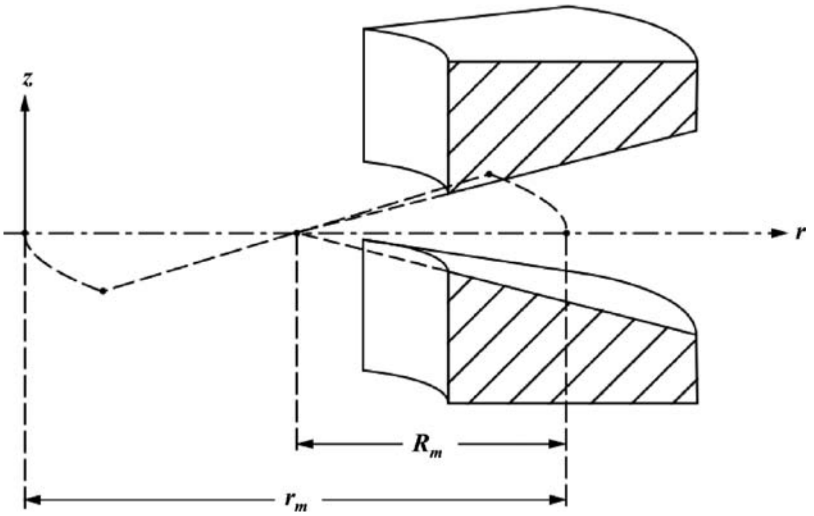

Fig. 3.20. Non-uniform magnetic sector field with $R_\mathrm{m} < r_\mathrm{m}$

The axial parameters are the same as above (3.24f–h)

$$\begin{aligned} f_z &= \frac{r_\mathrm{m}}{\sqrt{n}\sin\left(\sqrt{n}\phi\right)}, \\ g_z &= \frac{r_\mathrm{m}}{\sqrt{n}\tan\left(\sqrt{n}\phi\right)}, \\ p_z &= \frac{r_\mathrm{m}}{\sqrt{n}}\tan\left(\sqrt{n}\phi/2\right). \end{aligned}$$

Such a sector field acts radially as a diverging lens and axially as a strong focusing lens (Fig. 3.21).

In view of the rising characteristic of the sinh function (see Fig. 2.19), large dispersion factors ν can be realized with such a sector field. When used as a mass spectrometer, a radially focusing lens has to be provided. The factor n can be made negative, too (Fig. 3.22). Here the radial lens parameters are the same as in the general case (see (3.24 a–e)), but the axial ones are

$$\begin{aligned} f_z &= \frac{-r_\mathrm{m}}{\sqrt{|n|}\sinh\left(\sqrt{|n|}\phi\right)}, \\ g_z &= \frac{-r_\mathrm{m}}{\sqrt{|n|}\tanh\left(\sqrt{|n|}\phi\right)}, \\ p_z &= \frac{-r_\mathrm{m}}{\sqrt{|n|}}\tanh\left(\sqrt{|n|}\phi/2\right). \end{aligned} \tag{3.30}$$

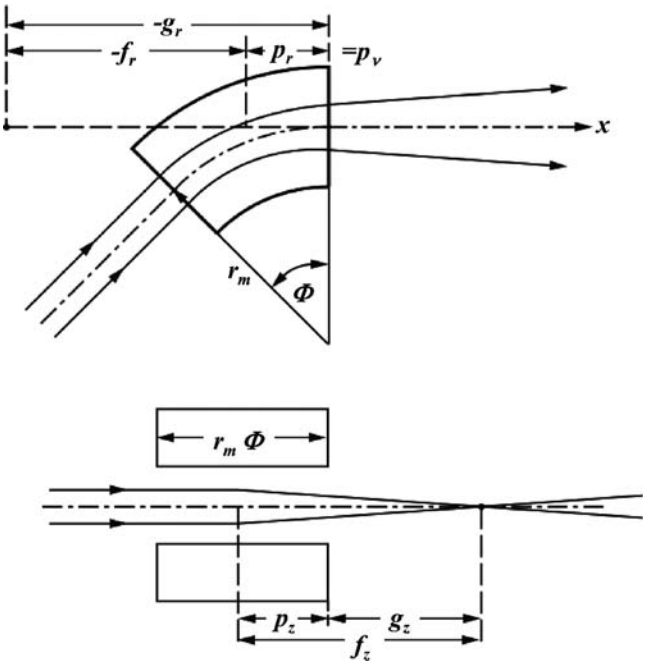

Fig. 3.21. Optical parameters of non-uniform magnetic sector field with $R_\mathrm{m} < r_\mathrm{m}$

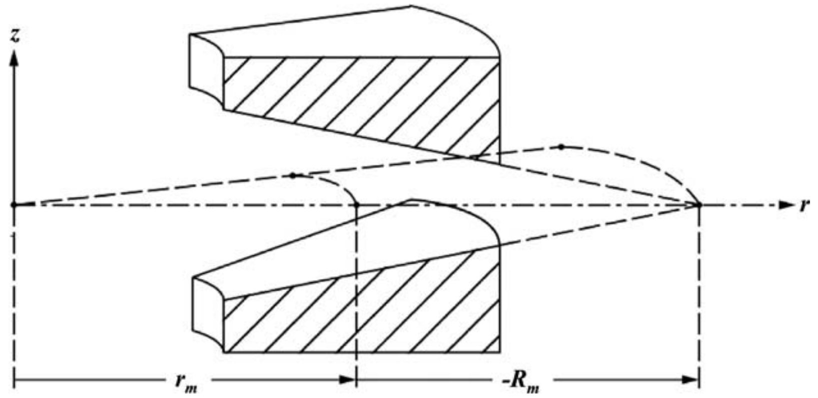

Fig. 3.22. Non-uniform magnetic sector field with $R_\mathrm{m} < 0$

The sector field acts as a diverging lens axially (Fig. 3.23). Another form of mass separators with a non-uniform magnetic field are those with a wedge-shaped magnetic gap. It is formed by tilting the planar pole piece surfaces, so that their planes intersect along a straight line (Fig. 3.24), the y-axis [24–27].

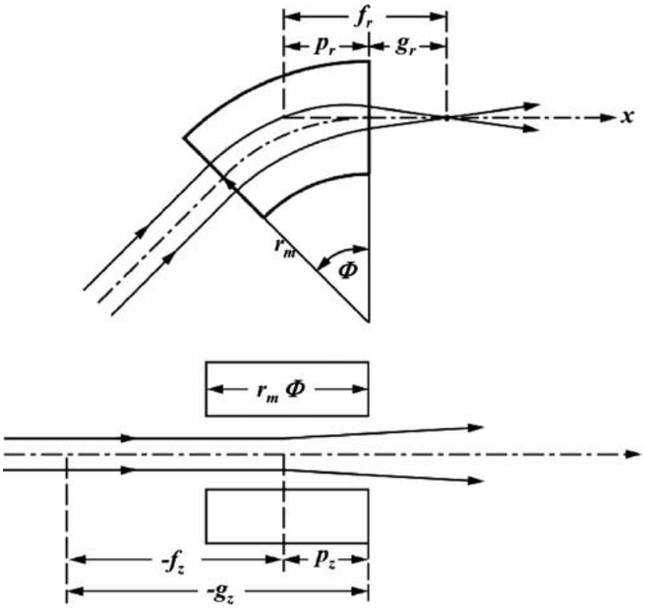

Fig. 3.23. Optical parameters of non-uniform magnetic sector field with $R_\mathrm{m} < 0$

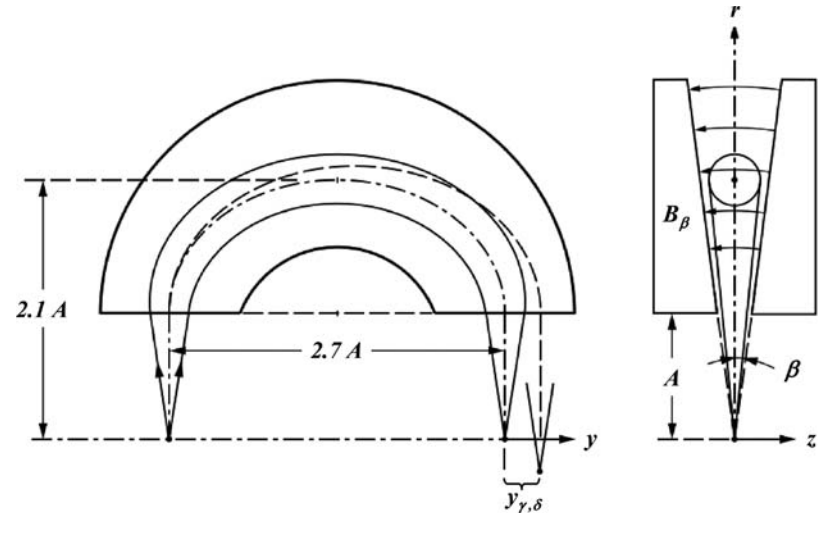

Fig. 3.24. Non-uniform magnetic field with wedge-shaped gap. Stigmatic focusing with the geometry shown. For central trajectory $K_0 = 0.7425$. Dispersion $y_{\gamma,\delta} = 2.17A\,(\gamma + \delta)$

The field lines between the pole piece surfaces inside the gap are circular arcs having the y-axis as their center. The tangential field strength is inversely proportional to the distance from the y-axis: $B_\beta = C/r$. The trajectories are trochoidal, the radius of curvature being proportional to the distance from the y-axis: $\rho = Kr$. The connection between K and C for singly charged ions is given by $KC = 143.6\sqrt{MV}$ (B in gauss, M in dalton, V in volt, r in cm). It is obvious that such a field refocuses ions starting from the y-axis with an angle β (see Fig. 3.24) back onto the y-axis simply because they cross the field lines inside the gap always at right angles so that the trajectories lie in the plane through the axis. In the y-direction there is also focusing, as shown in Fig. 3.24. However, no general analytical formulae can be given here, as in the previous cases of sector fields, for the ion optical parameters as functions of mean deflection radius and angle, because each case must be treated numerically. So only two examples of stigmatically focusing wedge fields are given here, one with 180° deflection, shown in Fig. 3.24, the other with 90° deflection (Fig. 3.25).

One can compare the first example (180° deflection) with a 180°-field with $n = 1/2$, taking the distance D between entrance and exit point of the optic axis as scaling parameter. In the wedge-gap case it is $D = 2.7A$, while in the $n = 1/2$-case it is $D = 2r_\mathrm{m}$. The dispersions are $y_{\gamma,\delta} = 0.8D\,(\gamma + \delta)$ (Fig. 3.24) and $y_{\gamma,\delta} = D\,(\gamma + \delta)$, respectively.

In comparing the two cases with 90° deflection (Figs. 3.25, 3.15) and choosing as scaling parameter again the distance D between entrance and exit point of the optic axis, one has in the wedge-gap case

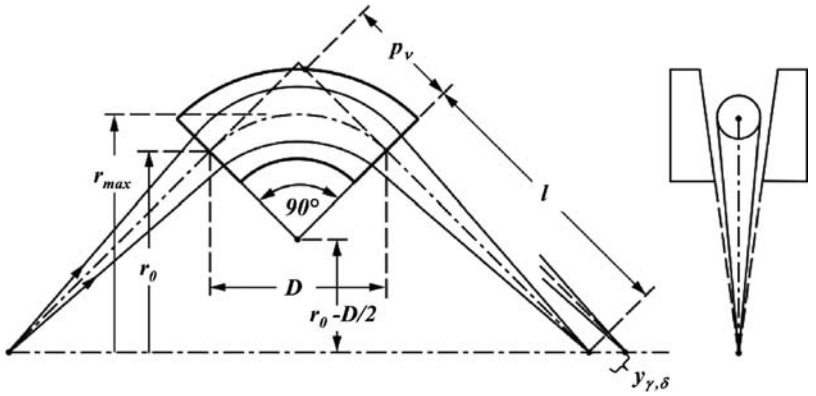

Fig. 3.25. Non-uniform magnetic field with wedge-shaped gap and stigmatic focusing with the geometry shown: $\phi = 90°; K_0 = 0.55; r_\mathrm{max} = 0.83l; \rho_\mathrm{max} = 0.46l; r_0 = 0.71l; \rho_0 = 0.39l; D = 0.62\,l; p_\nu = 0.39\,l$. Dispersion $y_{\gamma,\delta} = 0.95\,l\ (\gamma + \delta)$

$D = 0.62\,l$ and in the $n = 1/2$-case $D = \sqrt{2}r_{\mathrm{m}}$. The dispersions are $y_{\gamma,\delta} = 1.53D\,(\gamma + \delta)$ (wedge) and $y_{\gamma,\delta} = 1.41D\,(\gamma + \delta)$. So there is not much difference in the performance of the two stigmatic focusing cases. A disadvantage of the wedge-gap geometry is, however, that the gap width varies by more than a factor of two for 180° deflection, so that the pole pieces approach saturation earlier where the gap is narrower, with the consequence that the field distribution deviates from the dependency $B_\beta = C/r$.

4

Image Aberrations

Summary. The most important image aberrations of lenses and electric and magnetic sector fields are given.

In the previous chapters the first-order focusing properties were considered. When designing or operating an optical element such as a lens or a sector field, very soon the question arises what aperture angles can be admitted or which beam limiting apertures can be used. Large apertures are of course desirable for intensity reasons, but the limitation as to their diameter or width is given when the aberrations become comparable with the geometric (Gaussian) image size.

Only the most important aberrations are considered here: of trajectories starting from the axis point of the object, in rotationally symmetric systems (lenses) the so-called spherical $\left(\alpha^3\right)$ aberration and the chromatic $(\alpha\delta)$ aberration, in sector fields the quadratic $\left(\alpha^2, \beta^2\right)$ aberrations in the direction of the dispersion due to the aperture angles in the deflection plane α and β out of it.

4.1 Lenses

In a number of publications the optical properties of electrostatic lenses have been computed, including the spherical and chromatic aberrations [6–9]. Here, only rules of thumb are given for these aberrations of einzel lenses, since they depend very much on their geometries.

When a beam of particles consisting of trajectories parallel to the axis enters the lens, it is focused to the axis at the focal distance. But since the refraction of the trajectories increases slightly more than proportional to their distance from the axis, they do not meet exactly at the same point but form a caustic figure (Fig. 4.1). The narrowest

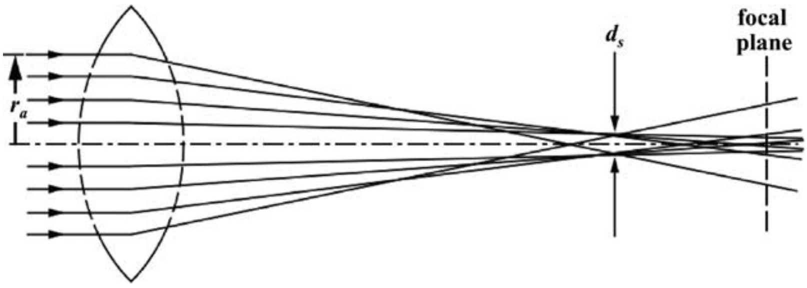

Fig. 4.1. Spherical aberration of rotationally symmetric lens

cross section, the so-called "circle of least confusion" is formed by the trajectories entering the lens at the distances r_a and $r_\mathrm{a}/2$, resp., where maximum distance r_a is usually defined by a round aperture.

The diameter of the circle of least confusion is usually called the spherical aberration. It can be given by the expression

$$d_\mathrm{s} = K_\mathrm{s} r_\mathrm{a}^3 / D^2, \tag{4.1}$$

where K_s is a dimensionless lens-specific factor ranging from 2 to 10 for einzel lenses, and D is a scaling parameter (cm) relating to the axial extent of the lens field. The spherical aberration of a lens with a given geometry is nearly independent of the imaging ratio, thus depending only on the diameter of the beam where it passes the lens. This is expressed by (4.1). The factor K_s is lower when the lens is operated in the accel–decel mode for the reason given above. As (4.1) shows, the dimension D has a strong influence on the spherical aberration: for a given distance between object and image, the field should be made axially as long as possible.

The chromatic aberration is a consequence of the fact that the focal length depends on the energy of the particles (Fig. 4.2). It can be written as

$$d_\mathrm{c} = K_\mathrm{c} r_\mathrm{a} \Delta V / V_0, \tag{4.2}$$

where K_c is a dimensionless factor ranging from 1 to 5 for einzel lenses, and $\Delta V / V_0 = \delta$ is the relative energy spread of the charged particles. The factor K_c is close to unity for accel–decel type einzel lenses, while for decel–accel type lenses it is closer to 5. This is a consequence of the fact that in the first case the particle energy inside the lens becomes higher than outside, so that inside the relative energy spread is smaller than outside, ΔV being constant.

With decel–accel lenses the opposite is the case: the relative energy spread inside the lens becomes larger than outside, resulting in a larger

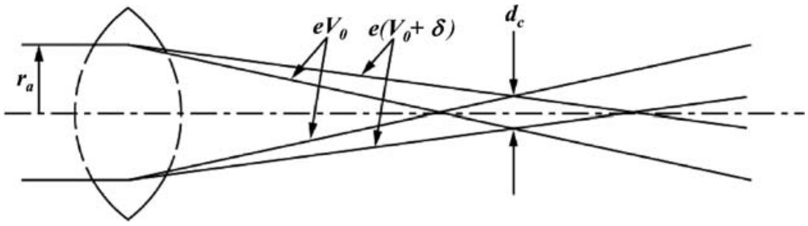

Fig. 4.2. Chromatic aberration of rotationally symmetric lens

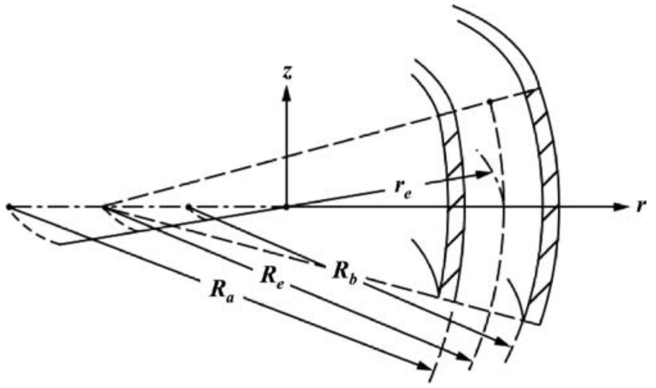

Fig. 4.3. Toroidal condenser with excentric axial curvatures of the electrode surfaces

factor K_c. So in view of keeping both the spherical and the chromatic aberrations as low as possible, einzel lenses are preferably operated in the accel–decel mode, provided that voltage breakdown considerations allow it, because this mode requires higher voltages to be applied to the middle lens element than the decel–accel mode (comp. Fig. 1.40).

4.2 General Toroidal Condenser

The first-order focusing properties of a toroidal condenser are determined by the axial curvature of the median equipotential surface, $c = r_e/R_e$. Given a certain radius R_e of the axial curvature, the curvatures of the condenser plates R_a and R_b do not necessarily have to be concentric, as shown in Fig. 2.14, but may be excentric, as shown in Fig. 4.3. This can be used to influence the second-order focusing properties, i.e. the α^2- and β^2-image aberrations [28–33].

This geometrical feature can be expressed by the differential quotient $R'_{\mathrm{e}} = \left(\frac{\mathrm{d}R}{\mathrm{d}r}\right)_{r=r_{\mathrm{e}}, z=0}$, which indicates the variation of the axial radius R as one moves away from the optic axis in the radial direction. When the axial curvatures are concentric, R'_{e} equals unity. Another description generally used is the derivation of the axial curvature at the optic axis

$$c' = r_{\mathrm{e}} \left[\frac{\mathrm{d}}{\mathrm{d}r} \left(\frac{r_{\mathrm{e}}}{R} \right) \right]_{r_{\mathrm{e}},0} . \tag{4.3}$$

The two coefficients are connected by the relation

$$c' = -c^2 R'_{\mathrm{e}}.$$

In order to calculate these aberrations for electrostatic sector fields, the potential near the optic axis (comp. (2.41)), has to be developed in a Taylor series to third order. This can be done analytically. The field strength components E_{r} and E_{z} are then obtained to second order, and with these also the trajectories. The potential is found to be

$$\begin{aligned} V(\rho, \zeta) = -2V_0 \Bigg[\rho - \frac{1}{2}(1+c)\rho^2 + \frac{c}{2}\zeta^2 + \frac{1}{6}\left(2 + 2c + c^2 - c'\right)\rho^3 \\ -\frac{1}{2}\left(c + c^2 - c'\right)\rho\zeta^2 \ldots \Bigg], \end{aligned} \tag{4.4}$$

where eV_0 is the particle energy outside the field and the potential of the optic axis $(\rho = \zeta = 0)$ is defined as zero. By differentiation, one obtains the field strength components

$$E_r = E_0 \left[1 - (1+c)\rho + \frac{1}{2}\left(2 + 2c + c^2 - c'\right)\rho^2 - \frac{1}{2}\left(c + c^2 - c'\right)\zeta^2 \ldots \right] \tag{4.5}$$

$$E_z = E_0 \zeta \left[c - \left(c + c^2 - c'\right)\rho \ldots \right] . \tag{4.6}$$

Another means to influence the second-order focusing properties is to replace the planar end faces of a sector field by curved ones (see Fig. 4.4).

The second-order angular aberrations of the image of a point source in the plane of symmetry $(z = 0)$ transverse to the exit optic axis are the α^2 aberration and the β^2 aberration (Fig. 4.5). They can be written as follows:

$$y_{\alpha\alpha} = r_{\mathrm{e}} \left(\kappa_{\alpha\alpha}\alpha^2 + \kappa_{\alpha u}\alpha u + \kappa_{uu}u^2 \right) + l_2 \left(\lambda_{\alpha\alpha}\alpha^2 + \lambda_{\alpha u}\alpha u + \lambda_{uu}u^2 \right), \tag{4.7}$$

$$y_{\beta\beta} = r_{\mathrm{e}} \left(\kappa_{\beta\beta}\beta^2 + \kappa_{\beta v}\beta v + \kappa_{vv}v^2 \right) + l_2 \left(\lambda_{\beta\beta}\beta^2 + \lambda_{\beta v}\beta v + \lambda_{vv}v^2 \right), \tag{4.8}$$

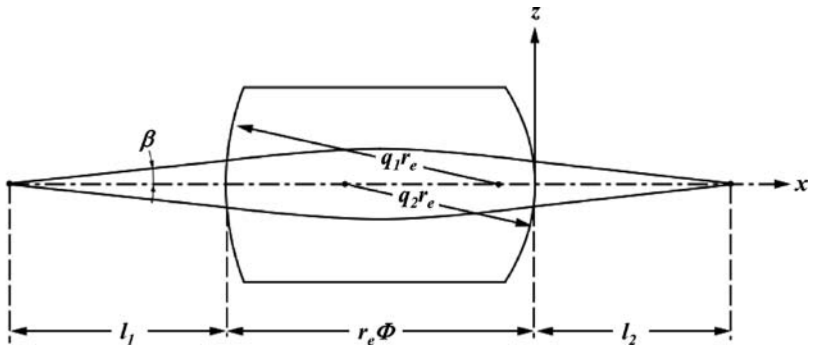

Fig. 4.4. Electrostatic sector field with curved entrance and exit faces, $q_1 r_\mathrm{e} = Q_1, q_2 r_\mathrm{e} = Q_2$

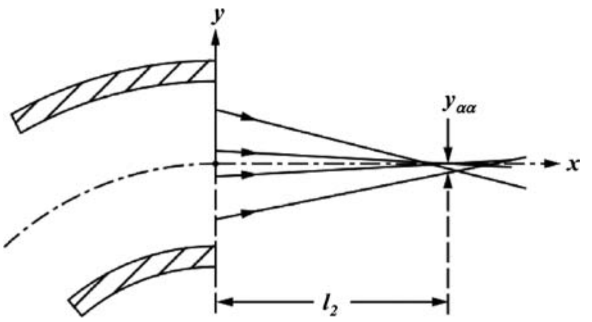

Fig. 4.5. Second-order angular aberration of image point formed by a sector field

where u and v are the dimensionless radial and axial entrance distances from the optic axis: $u = r/r_\mathrm{e} - 1 = \alpha l_1/r_\mathrm{e}$, $v = z/r_\mathrm{e} = \beta l_1/r_\mathrm{e}$.

The coefficients κ_{ik} and λ_{ik} are

$$\begin{aligned}
\kappa_{\alpha\alpha} &= \frac{k_1}{2-c}\left(\frac{1}{2}\kappa_\alpha^2 - \kappa_\delta\right), \\
\kappa_{\alpha u} &= -k_1\kappa_\alpha\kappa_\delta, \\
\kappa_{uu} &= -\frac{k_1}{2}\left(\kappa_\alpha^2 + \kappa_\delta\right) - \frac{1}{2q_1}\kappa_\alpha, \\
\lambda_{\alpha\alpha} &= -k_1\kappa_\alpha\kappa_\delta - \frac{1}{2q_2}\kappa_\alpha^2, \\
\lambda_{\alpha u} &= -k_1\left(\kappa_\alpha^2 + \kappa_u\kappa_\delta\right) - \frac{1}{q_2}\kappa_\alpha\kappa_u,
\end{aligned}$$

$$\begin{aligned}
\lambda_{uu} &= -\frac{k_1}{2}\kappa_\alpha\left(1+2\kappa_u\right) - \frac{1}{2q_1}\kappa_u - \frac{1}{2q_2}\kappa_u^2, \\
\kappa_{\beta\beta} &= k_2\left(\frac{1}{2}\kappa_\beta^2 - \kappa_\delta\right) - \kappa_\delta, \\
\kappa_{\beta v} &= k_2\left(\kappa_\beta\kappa_u - \kappa_\alpha\right), \\
\kappa_{vv} &= \frac{k_2}{2}\left[\left(2-3c\right)\kappa_\delta - c\kappa_\beta^2\right] - c\kappa_\delta + \frac{1}{2q_1}\kappa_\alpha, \\
\lambda_{\beta\beta} &= k_2\left(\kappa_\beta\kappa_u - \kappa_\alpha\right) - \kappa_\alpha + \frac{1}{2q_2}\kappa_\beta^2, \\
\lambda_{\beta v} &= k_2\left[\left(2-c\right)\kappa_\delta - 2c\kappa_\beta^2\right] + \frac{1}{q_2}\kappa_\beta\kappa_u, \\
\lambda_{vv} &= k_2\left(\frac{2-3c}{2}\kappa_\alpha - c\kappa_\beta\kappa_v\right) - c\kappa_\alpha + \frac{1}{2q_1}\kappa_u + \frac{1}{2q_2}\kappa_v^2,
\end{aligned} \tag{4.9}$$

with the abbreviations

$$\begin{aligned}
\kappa_\alpha &= \frac{\sin\left(\sqrt{2-c}\phi\right)}{\sqrt{2-c}}, \\
\kappa_\delta &= \frac{1-\cos\left(\sqrt{2-c}\phi\right)}{2-c}, \\
\kappa_u &= \cos\left(\sqrt{2-c}\phi\right), \\
\kappa_\beta &= \frac{\sin\left(\sqrt{c}\phi\right)}{\sqrt{c}}, \\
\kappa_v &= \cos\left(\sqrt{c}\phi\right).
\end{aligned}$$

The factors q_1 and q_2 denote the curvatures of the entrance and exit front faces (see Fig. 4.4). The factors k_1 and k_2 are

$$\begin{aligned}
k_1 &= \frac{1}{3}\left(8-7c+c^2-c'\right), \\
k_2 &= \frac{c+c^2-c'}{2-5c}.
\end{aligned}$$

As an example, the toroidal energy analyzer described earlier (Fig. 2.15) would have rather large α^2 and β^2 aberrations with planar end faces and concentric axial radii. By judicious choice of $q_1,\ q_2 = q$ and c' both of these aberrations can be made to vanish [33], thus allowing rather large aperture angles.

When a certain value of c' is chosen, the axial radii R_a and R_b of the condenser plates have to be determined. They can be calculated by means of the relation [34]

$$\frac{r_\mathrm{e}}{R_\mathrm{a,b}} = c + c'\rho_\mathrm{a,b} + \frac{1}{2}\rho_\mathrm{a,b}^2 \left(-c + 2c^2 - c^3 + c' - 3cc'\right) , \qquad (4.10)$$

where $r_\mathrm{e}\rho_\mathrm{a,b}$ is the distance of the plates in the plane $z = 0$ from the axis ($\rho_\mathrm{a} < 0$; $\rho_\mathrm{b} > 0$).

In order to realize the required radii qr_e, Herzog shunts [42] (see below) should be fitted to both ends of the sector field, so that the effective field boundaries coincide with the contours given by the values of q.

Note: For the special case $c = 2$ (see Fig. 2.17) the coefficients κ_{ik} and λ_{ik} (4.9) cannot be used because most of the coefficients go to infinity. It requires a separate integration of the equation of motion for the trajectory. The same applies for the special case $c = 0.4$ for the axial coefficients because the factor k_2 goes to infinity. Since these cases are not important, their coefficients κ_{ik} and λ_{ik} are not given here.

4.3 Spherical Condenser

Inserting $c = 1$ into the coefficients of (4.9), the image aberrations of spherical condensers are easily calculated.

For example, for a 180° spherical condenser with concentric electrodes ($c' = -1$; Fig. 2.13) the aberration is found to be $y_{\alpha\alpha} = r_\mathrm{e}\kappa_{\alpha\alpha}\alpha^2$ with $\kappa_{\alpha\alpha} = -2$, while $y_{\beta\beta} = r_\mathrm{e}\kappa_{\beta\beta}\beta^2 = 0$, since $\kappa_{\beta\beta} = 0$. A 90° spherical condenser with symmetric imaging (Fig. 2.12) has the aberrations $y_{\alpha\alpha} = -5r_\mathrm{e}\alpha^2$, $y_{\beta\beta} = r_\mathrm{e}\beta^2$, so that the combined aberration turns out to be $6r_\mathrm{e}\alpha^2$, when the particle beam is confined by a round aperture so that $\beta = \alpha$. When values of $c' \neq 1$ and curved end faces are admitted, the aberrations can be modified. It turns out, however, that it is not possible, by a judicious choice of c' and q_1, q_2 to correct both the α^2 and β^2 aberrations simultaneously. However, they can be made to coincide at the value $y_{\alpha\alpha} = y_{\beta\beta} = -2r_\mathrm{e}\alpha^2$. This is the case for $c' = 0.8$ with planar end faces ($q_1 = q_2 = \infty$) (Fig. 4.6). This is only a third of the former value with concentric spherical plates, which means three times higher luminosity of this partly corrected sector field. Only the median equipotential surface is spherical ($c = 1$), while the electrode surfaces are slightly toroidal.

The same value $y_{\alpha\alpha} = y_{\beta\beta} = -2r_\mathrm{e}\alpha^2$ can be obtained with exactly spherical electrode surfaces ($c' = -1$) but curved end faces, whereby

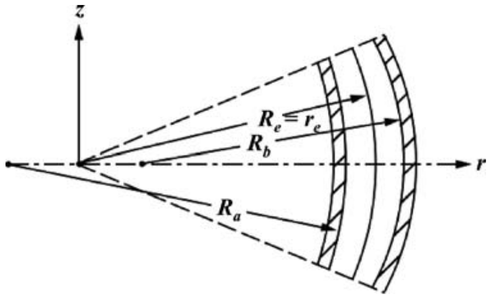

Fig. 4.6. Cross section of modified spherical condenser with slightly toroidal electrode surfaces. The median equipotential surface is spherical, while the axial curvatures of the electrode surfaces are excentric

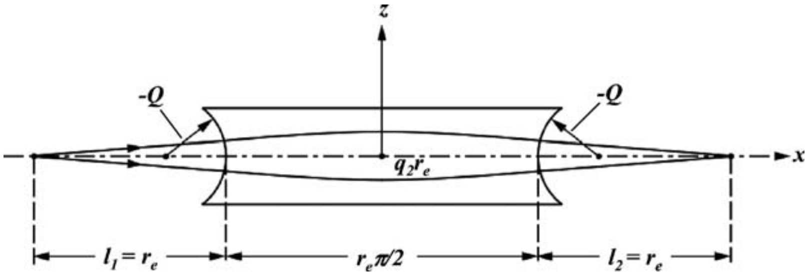

Fig. 4.7. Sector field with spherical electrode surfaces and curved end faces

the curvature of the end faces has to be $q_1 = q_2 = q = -3$. The radius of curvature is then $Q = qr_\mathrm{e} = -r_\mathrm{e}/3$ (Fig. 4.7).

With a 180° spherical condenser the two aberrations can be made equal when $c' = 0.5$. Then they have the value $y_{\alpha\alpha} = y_{\beta\beta} = -r_\mathrm{e}\alpha^2$. This is half the value as for a 90° sector field. Another example are sector fields with spherical electrodes ($c' = -1$) and symmetric imaging ($l_1 = l_2 = l = r_\mathrm{e} \cot(\phi/2)$), which have entrance and exit faces with curvatures centered at the source and image points ($q_1 = q_2 = -l/r_\mathrm{e}$) (Fig. 4.8). They have no β^2 aberration, only an α^2 aberration. This could be utilized in applications where the axial acceptance angle β can be made substantially larger than the radial one α.

4.4 Cylindrical Condenser

The aberrations of cylindrical condenser sector fields are found using the coefficients of (4.9) with $c = 0$, so that $k_1 = (8 - c')/3$; $k_2 = -c'/2$. When the electrodes have exactly cylindrical surfaces, $c' = 0$, too. In

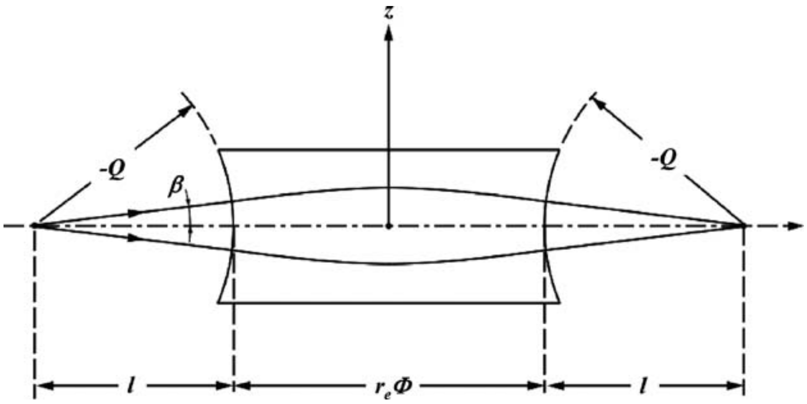

Fig. 4.8. When the centers of curvature of the end faces coincide with the object and image points the β^2 aberration becomes zero

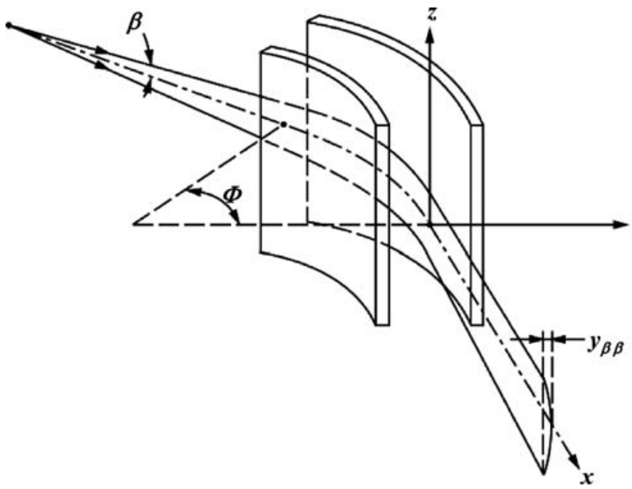

Fig. 4.9. Image aberration $y_{\beta\beta}$ of cylindrical condenser causes the image line to be slightly curved

this case, e.g. the α^2 aberration with the 127° sector field (Fig. 2.7), where $l_1 = l_2 = 0$, is found to be $y_{\alpha\alpha} = -1.33r_\mathrm{e}\alpha^2$, while $y_{\beta\beta} = -r_\mathrm{e}\beta^2$. For a 90° condenser (Fig. 2.6), (4.7) and (4.8) yield, in the case of the image at the exit boundary $y_{\alpha\alpha} = -3.27r_\mathrm{e}\alpha^2$, $y_{\beta\beta} = -0.81r_\mathrm{e}\beta^2$; in case of symmetric imaging $y_{\alpha\alpha} = -1.82r_\mathrm{e}\alpha^2$, $y_{\beta\beta} = -r_\mathrm{e}\beta^2$. In the case of symmetric imaging $y_{\beta\beta}$ is always $-r_\mathrm{e}\beta^2$, independent of ϕ. Since there is no focusing in the z direction , the $y_{\beta\beta}$ aberration means that the particles starting from a point source are focused in the image plane in a line which is slightly curved (Fig. 4.9). When the object is a slit extended in the z direction, these curved lines are superimposed. As the above examples show, the α^2 aberration is usually larger than the β^2 aberration, α and β being equal, and since the β^2 aberration has the same sign as the α^2 aberration, it does not matter.

In special cases, the α^2 aberration could be modified by choosing $c' \neq 0$, or by curving the entrance and/or exit faces. Conditions with $c' \neq 0$ are obtained when only the median equipotential surface is exactly cylindrical, while the electrode surfaces are slightly toroidal having opposite curvatures [35].

4.5 Uniform Magnetic Sector Fields [36–38]

The second-order angular aberrations of the image of a point source can be written as follows:

$$y_{\alpha\alpha} = r_{\mathrm{m}} \left(\mu_{\alpha\alpha}\alpha^2 + \mu_{\alpha u}\alpha u + \mu_{uu}u^2\right) + l_2 \left(\nu_{\alpha\alpha}\alpha^2 + \nu_{\alpha u}\alpha u + \nu_{uu}u^2\right) \tag{4.11}$$

$$y_{\beta\beta} = r_{\mathrm{m}} \left(\mu_{\beta\beta}\beta^2 + \mu_{\beta v}\beta v + \mu_{vv}v^2\right) + l_2 \left(\nu_{\beta\beta}\beta^2 + \nu_{\beta v}\beta v + \nu_{vv}v^2\right) \tag{4.12}$$

where, as in the case of electrostatic sector fields, u and v are the dimensionless radial and axial distances from the optic axis: $u = r/r_{\mathrm{m}} - 1 = \alpha l_1/r_{\mathrm{m}}$; $v = z/r_{\mathrm{m}} = \beta l_1/r_{\mathrm{m}}$. In order to influence the radial aberrations, the entrance and exit field boundaries can be curved (Fig. 4.10). The coefficients μ_{ik} and ν_{ik} are

$$\begin{aligned}
\mu_{\alpha\alpha} &= -\mu_\delta + \frac{1}{2}\mu_\alpha^2 \left(1 + t_2^2\right) \\
\mu_{\alpha u} &= \mu_\alpha\mu_u \left(1 + t_2^2\right) + \left(\mu_u - 1\right) t_1 \\
\mu_{uu} &= \frac{1}{2}\nu_u \left(\mu_1 + \mu_u t_2\right) + \frac{1}{2q_1c_1^3}\mu_\alpha \\
\nu_{\alpha\alpha} &= -\frac{1}{2} \left(\mu_2 + \nu_\alpha^2 t_2\right) + \frac{1}{2q_2c_2^3}\mu_\alpha^2 \\
\nu_{\alpha u} &= \nu_u \left(t_1 - \nu_\alpha t_2\right) + \frac{1}{q_2c_2^3}\mu_\alpha\mu_u
\end{aligned}$$

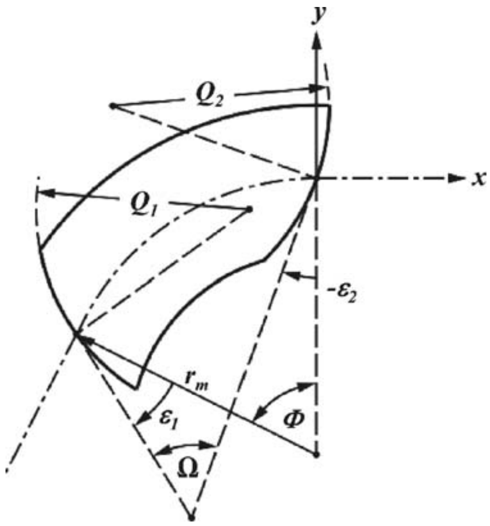

Fig. 4.10. Magnetic sector field with curved entrance and exit faces

$$
\begin{aligned}
\nu_{uu} &= -\frac{1}{2}\nu_u^2 t_2 + \frac{1}{2q_1c_1^3}\nu_\alpha + \frac{1}{2q_2c_2^3}\mu_u^2 \\
\mu_{\beta\beta} &= -\mu_\delta - \frac{1}{2}\left(1+t_2^2\right)\phi^2 \\
\mu_{\beta v} &= \left(1-\mu_u\right)t_1 - \left(1+t_2^2\right)\left(1-t_1\phi\right)\phi \\
\mu_{vv} &= -\mu_\delta t_1^2 + \frac{1}{2}\left[\left(1+t_1^2\right)\mu_u + \mu_\alpha t_1^3 - \left(1+t_2^2\right)\left(1-t_1\phi\right)^2\right] - \frac{1}{2q_1c_1^3}\mu_\alpha \\
\nu_{\beta\beta} &= -\nu_\delta + t_2^2\phi\left(1-\frac{1}{2}t_2\phi\right) - \frac{1}{2q_2c_2^3}\phi^2 \\
\nu_{\beta v} &= t_1\left(-\nu_u + t_2\right) + t_2^2\left(1-2t_1\phi\right) - t_2^3\phi\left(1-t_1\phi\right) - \frac{\phi}{q_2c_2^3}\left(1-t_1\phi\right) \\
\nu_{vv} &= -\nu_\delta t_1^2 - \frac{1}{2}\mu_1\left(1+t_1^2\right) + \frac{1}{2}\nu_\alpha\left(1+2t_1^2\right)t_1 - t_1t_2^2\left(1-t_1\phi\right) \\
&\quad - \frac{1}{2}t_2^3\left(1-t_1\phi\right)^2 - \frac{1}{2q_1c_1^3}\nu_\alpha - \frac{1}{2q_2c_2^3}\left(1-t_1\phi\right)^2
\end{aligned}
\tag{4.13}
$$

with the abbreviations

$$\mu_\alpha = \sin\phi, \quad \mu_\delta = \frac{1}{2}(1-\cos\phi), \quad \mu_u = \frac{\cos(\phi-\varepsilon_1)}{\cos\varepsilon_1},$$

$$\mu_1 = \frac{\sin(\phi-\varepsilon_1)}{\cos\varepsilon_1}, \quad \mu_2 = \frac{\sin(\phi-\varepsilon_2)}{\cos\varepsilon_2},$$

$$\nu_\alpha = \frac{\cos(\phi-\varepsilon_2)}{\cos\varepsilon_2}, \quad \nu_u = -\frac{\sin(\phi-\varepsilon_1-\varepsilon_2)}{\cos\varepsilon_1\cos\varepsilon_2},$$

$$\nu_\delta = \frac{1}{2}\left[\sin\phi + t_2(1-\cos\phi)\right],$$

$$t_1 = \tan\varepsilon_1, \quad c_1 = \cos\varepsilon_1, \quad q_1 = Q_1/r_\mathrm{m}(\text{entrance curvature})$$

$$t_2 = \tan\varepsilon_2, \quad c_2 = \cos\varepsilon_2, \quad q_2 = Q_2/r_\mathrm{m}(\text{exit curvature}).$$

As an example [39] for a 90° sector field with $\varepsilon_1 = \varepsilon_2 = 0$ and curved concentric entrance and exit boundaries, $Q_1 = Q_2 = r_\mathrm{m}$ (Fig. 4.11),

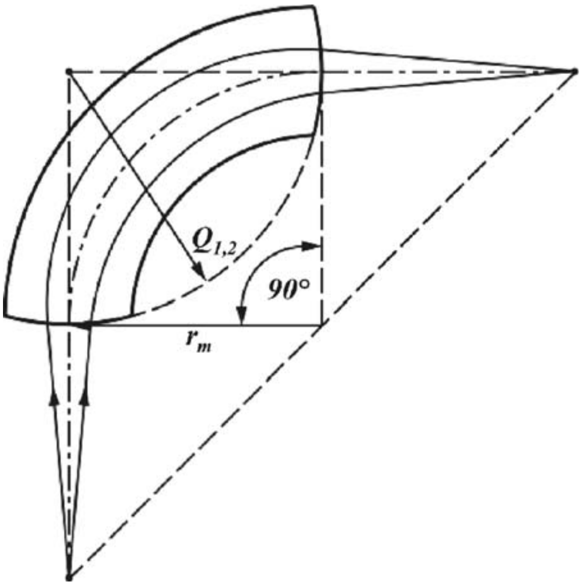

Fig. 4.11. Uniform magnetic sector field with zero α^2 aberration. The radius of curvature of the end faces equals r_m $(Q_1 = Q_2 = r_\mathrm{m})$

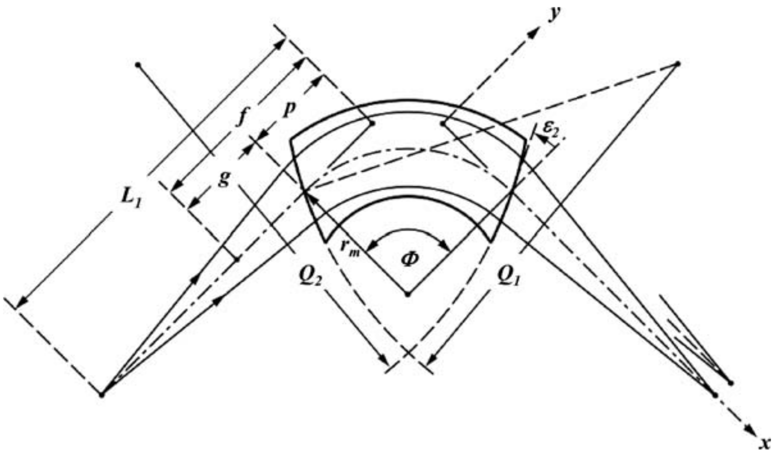

Fig. 4.12. Symmetric stigmatic imaging uniform magnetic sector field with corrected α^2 aberration. $\phi = 90°, \varepsilon_1 = \varepsilon_2 = 26.6°, f = 4/3r_{\mathrm{m}}, g = p = 2/3r_{\mathrm{m}}, L_1 = L_2 = 2f, Q_1 = Q_2 = 2.8r_{\mathrm{m}}$ (comp. Fig. 3.12)

the α^2 aberration becomes zero, using the above coefficients. The radial β^2 aberration, however, will be $y_{\beta\beta} = -\left(3 + \pi + \pi^2/4\right) r_{\mathrm{m}}\beta^2 = -8.61r_{\mathrm{m}}\beta^2$, so that a point source is imaged in a curved line (comp. Fig. 4.9).

For a stigmatically imaging 90° sector field with $\tan\varepsilon_1 = \tan\varepsilon_2 = 0.5$ (Fig. 3.12), the α^2 aberration turns out to be $y_{\alpha\alpha} = -4r_{\mathrm{m}}\alpha^2$, while the radial β^2 aberration is $y_{\beta\beta} = -9r_{\mathrm{m}}\beta^2$. By applying curvatures to the boundaries, the α^2 aberration can be made to vanish. This is the case with $Q_1 = Q_2 = 2.8r_{\mathrm{m}}$ (Fig. 4.12). The β^2 aberration, however, increases then to $y_{\beta\beta} = -13r_{\mathrm{m}}\beta^2$. The radial acceptance angle α can thus be made considerably larger than the axial angle β. In view of this, it is advantageous that the radial angle extends in the direction of the pole piece gap, while the axial angle is confined by the pole pieces.

4.6 Non-Uniform Magnetic Sector Fields [20–23, 40, 41]

The aberration coefficients for magnetic sector fields with conical pole faces and entrance and exit axes normal to the boundaries are, using these abbreviations:

$$\begin{aligned}
\mu_\alpha &= \frac{\sin\left(\sqrt{1-n}\phi\right)}{\sqrt{1-n}}, \quad \mu_u = \nu_\alpha = \cos\left(\sqrt{1-n}\phi\right),\\
\mu_\delta &= \frac{1-\cos\left(\sqrt{1-n}\phi\right)}{2\,(1-n)},\\
\mu_\beta &= \frac{\sin\sqrt{n}\phi}{\sqrt{n}}, \quad \mu_v = \cos\left(\sqrt{n}\phi\right):\\
\mu_{\alpha\alpha} &= \frac{1}{3}\mu_\delta\left[2n-(2n-3)\,\mu_u\right]\\
\mu_{\alpha u} &= \frac{1}{3}\mu_\alpha\left[2n-(2n-3)\,\mu_u\right]\\
\mu_{uu} &= \frac{1-n}{6}\left[4n\mu_\delta+(2n-3)\,\mu_\alpha^2\right]+\frac{1}{2q_1}\mu_\alpha\\
\nu_{\alpha\alpha} &= \frac{1}{6}\mu_\alpha\left[4n\,(1-\mu_u)-3\right]+\frac{1}{2q_2}\mu_\alpha^2\\
\nu_{\alpha u} &= \frac{4}{3}n\,(1-n)\left(\mu_\alpha^2-\mu_\delta\right)+\frac{1}{q_2}\mu_\alpha\mu_u\\
\nu_{uu} &= \frac{1}{3}n\,(1-n)\,\mu_\alpha\,(1+2\mu_u)+\frac{1}{2q_2}\mu_u^2+\frac{1}{2q_1}\mu_u\\
\mu_{\beta\beta} &= \frac{1}{5n-1}\left[-n^2\mu_\beta^2-\left(2n-\frac{1}{2}\right)(1-\mu_u)\right]-\frac{1}{2}\mu_\beta^2\\
\mu_{\beta v} &= \frac{2n^2}{5n-1}\left(\mu_\alpha-\mu_\beta\mu_v\right)-\mu_\beta\mu_v\\
\mu_{vv} &= \frac{n}{5n-1}\left[2n\mu_\beta^2-\left(3n-\frac{1}{2}\right)(1-\mu_u)\right]-\frac{1}{2q_1}\mu_\alpha+\frac{1}{2}\left(\mu_u-\mu_v^2\right)\\
\nu_{\beta\beta} &= \frac{1}{5n-1}\left[(1-n)\left(\frac{1}{2}-2n\right)\mu_\alpha-2n^2\mu_\beta\mu_v\right]-\frac{1}{2q_2}\mu_\beta^2\\
\nu_{\beta v} &= \frac{2n^2}{5n-1}\left(2n\mu_\beta^2+\mu_u-1\right)-\frac{1}{q_2}\mu_\beta\mu_v\\
\nu_{vv} &= \frac{n}{5n-1}\left[(1-n)\left(\frac{1}{2}-3n\right)\mu_\alpha+2n^2\mu_\beta\mu_v\right]\\
&\quad -\frac{1}{2q_1}\mu_u-\frac{1}{2q_2}\mu_v^2-\frac{1-n}{2}\mu_\alpha
\end{aligned} \tag{4.14}$$

Setting $n = 0$ yields the coefficients for the uniform magnetic sector field with normal entry and exit axes ($t_1 = t_2 = 0$).

With symmetric stigmatic imaging, in Table 4.1 values of the source and image distance l of the dispersion at the image position $y_{\gamma,\delta}$ and

Table 4.1. Aberrations of stigmatically imaging sector fields ($n = 1/2$) for various sector angles

ϕ	l/r_m	$y_{\delta,\gamma}/r_\mathrm{m}\,(\gamma+\delta)$	$y_{\alpha\alpha}/r_\mathrm{m}\alpha^2$	$y_{\beta\beta}/r_m\beta^2$
90°	2.28	2.0	4.13	−7.55
127.3°	1.41	2.0	1.26	−2.66
180°	0.70	2.0	−0.21	−1.05
254.6°	0	2.0	−0.67	−0.67

of the image aberrations $y_{\alpha\alpha}$ and $y_{\beta\beta}$ are listed for various sector fields with straight boundaries having various sector angles ϕ. One can see that a 180° sector field has rather low aberrations.

The aberrations of the stigmatically imaging fields of the wedge type (see Figs. 3.24, 3.25) have been computed numerically. For the 180° deflection field, the α^2 aberration is zero [25], while the β^2 aberration can be derived from published values [27] as $y_{\beta\beta} = 1.1\rho_\mathrm{m}\beta^2$, where ρ_m is the mean deflection radius of the central trajectory. Using ρ_m as scaling parameter makes it easier to compare with the other sector fields, where the deflection radius of the central trajectory r_m is used as a scaling parameter. For the 90° wedge type field, the α^2 aberration was found to be $y_{\alpha\alpha} = 4.5\rho_\mathrm{m}\alpha^2$ and the β^2 aberration $y_{\beta\beta} = 9.6\rho_\mathrm{m}\beta^2$. It should be noted that these values do not contain fringe field effects, which probably influence the values for the β^2 aberration.

5

Fringe Field Confinement

Summary. Examples for fringe field confinement of electric and magnetic sector fields are presented.

With electrostatic and magnetic sector fields, the field strength at the entrance and exit boundaries does not drop sharply from the value inside the gap to zero outside, but drops gradually. In order to confine this transition region in a controlled way, so-called “Herzog shunts” (also called “field clamps” in the literature) are usually applied [42]. They define an effective field boundary (“ersatzfeldgrenze”), where the field can be assumed to be cut off sharply as far as first-order optical properties are concerned. Second-order effects concerning image aberrations are not eliminated by Herzog shunts.

With electrostatic sector fields, Herzog shunts can be chosen in such a way that the “ersatzfeldgrenze” coincides with the geometric field boundary given by the deflection angle ϕ. An example is shown in Fig. 5.1. With curved field boundaries the shunts are to be shaped accordingly.

For the general case that the distance ξ should be zero, Fig. 5.2 shows the slot widths and distances of Herzog shunts in relation to the plate distances of electric sectors. For very narrow slots $d = 0.52\,k$.

In the case of magnetic sector fields the shunts have to be made out of mild steel like the pole pieces. It is not advisable to choose a geometry where the ersatzfeldgrenze coincides with the pole piece end faces because the Herzog shunt would be too close to the pole pieces causing a magnetic field strength higher across the distance d than in the gap, and thus enhancing the danger of saturation in the pole piece edges. In order to keep the field strength across the distance d lower than within the gap, the distance d should be larger than half the gap

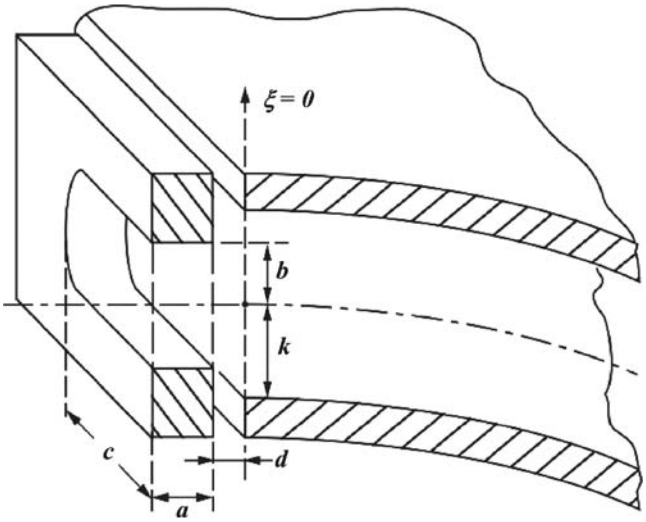

Fig. 5.1. "Herzog shunt" with electrostatic sector field. With $b = \frac{2}{3}k$, $d = \frac{1}{3}k$, $a = b$, $c \geq 5b$ the "ersatzfeldgrenze" coincides with the geometric end face given by ϕ. The distance ξ is zero

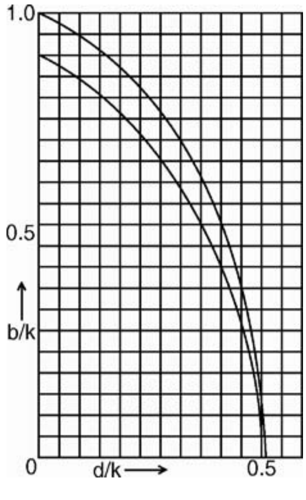

Fig. 5.2. With a certain choice of distance d and slot width $2b$ of Herzog shunts in relation to plate distance $2k$ of electric sectors the effective field length coincides with the real one. The curves show b as function of d for thick (*upper curve*) and thin (*lower curve*) Herzog shunts

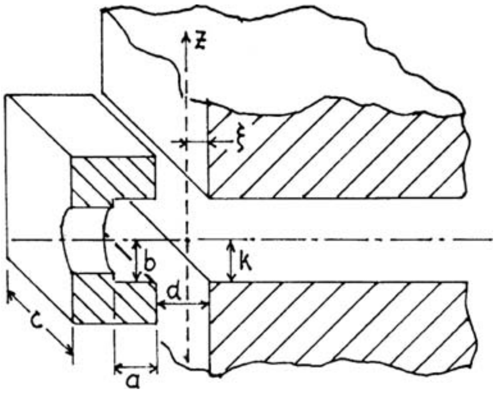

Fig. 5.3. "Herzog shunt" with magnetic sector field. With $b = k$, $d = 1.25k$, $a = b$, $c \geq 5b$, the distance $\xi = 0.5k$

width k. And in order to guide the stray field lines between the pole pieces on the shortest possible way through the shunt, thereby avoiding saturation effects at higher field strengths, a form with a horseshoe-like cross section as shown in Fig. 5.3 is preferable. With non-uniform fields in the gap the shunts should be shaped in such a way that the relative dimensions are the same at each cross section through the field boundary.

A

Applications

Summary. Various examples of applications are shown, such as combination of light optical with electrostatic lenses, electrostatic deflectors and energy analyzers, elimination of image aberrations of sector fields, and a combination of a lens with magnetic and electric sector fields to form a mass spectrometer.

A.1 Emission Lens Combined with Optical Mirror Objective Lens

Emission lenses are described schematically in Sect. 1.10. Figure A.1 shows an actual emission lens with three electrodes (comp. Fig. 1.34), which was designed and constructed for an electron emission microscope [43]. The particular conical shape of the electrodes was chosen in such a way that a light optical microscope objective lens of the reflecting type could be accommodated. It comprises two nearly concentric spherical mirror surfaces, a concave and a convex one, which can be used either for viewing the sample surface or to irradiate the sample with UV light for electron emission. The surface can also be imaged by electrons which are directed from above through the lens, decelerated to low energies, and scattered and diffracted from the surface.

Figure A.2 shows an equipotential plot [44] of the emission lens field for the condition that the emitted electrons, accelerated by 15 kV, image the surface to infinity. On the left-hand side the axial potential distribution is shown (comp. Fig. 1.34), consisting of a nearly uniform acceleration field followed by a decel–accel lens. The acceleration electrode and the end electrode are at the same potential, but because of the field penetration from the center electrode the electrons have attained only about two thirds of the final energy when they pass through the acceleration electrode. Thereafter they are decelerated to

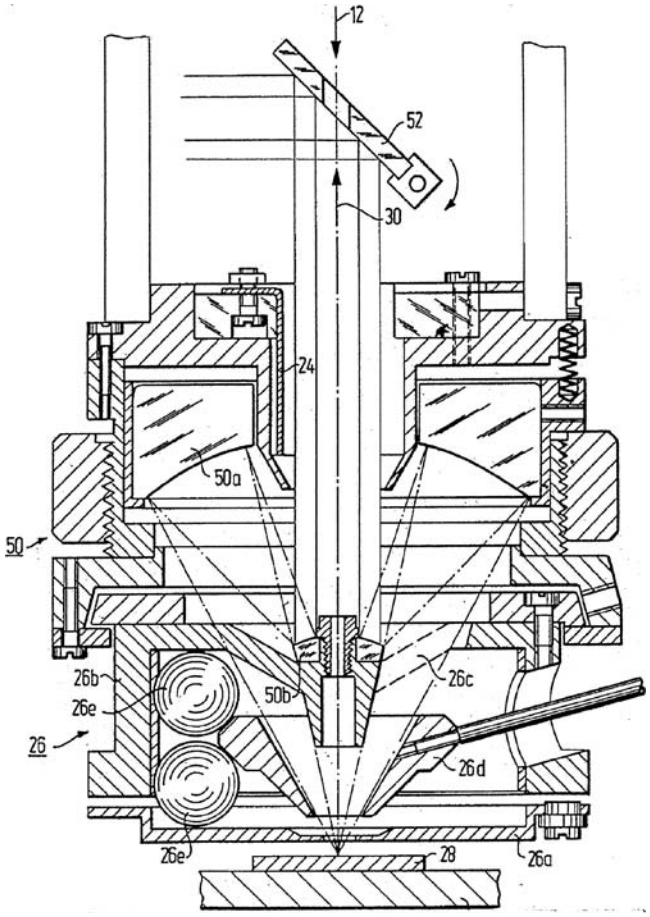

Fig. A.1. Emission lens combined with mirror objective. Acceleration from sample (28) to grounded first electrode (26a) through center electrode (26d) to grounded third electrode (26c). The center electrode is held between six 10 mm sapphire balls (26e) for centering and insulation. The spherical mirrors (50a, 50b) are adjustable relative to each other axially and laterally. For UV irradiation from above the mirror (52) for visual observation is swung out of the way. The sample surface can be imaged either with photoelectrons or with scattered and diffracted electrons arriving from the above (12)

about 2 keV within the center electrode and then accelerated to the final energy of 15 keV.

A.2 Combined Objective and Emission Lens

An electrostatic lens of similar design as the emission lens described above, also incorporating a mirror type microscope objective for

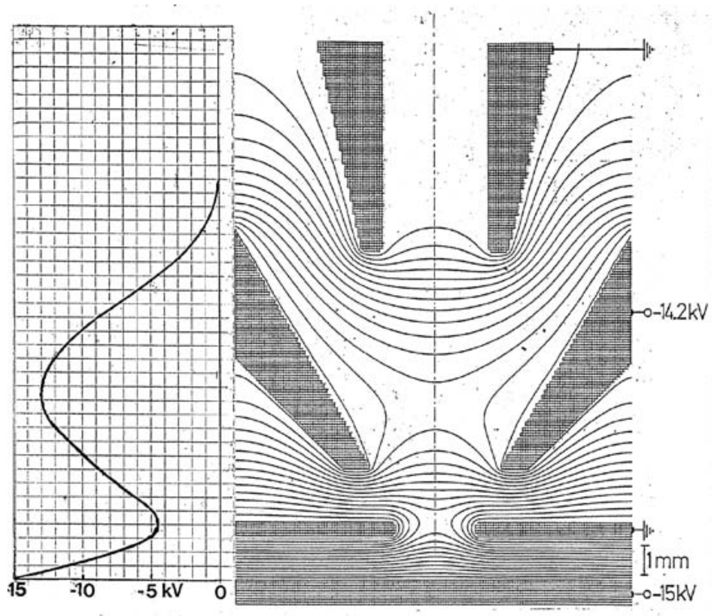

Fig. A.2. Field contour plot of emission lens imaging the surface to infinity. The equipotential lines are 1,000 V apart. The backfocal length is 11 mm. The plot to the left shows the axial potential distribution

viewing, is shown in Fig. A.3 [45]. It was designed for scanning secondary ion mass spectrometry (SIMS), a method of surface characterization, where a focused energetic primary ion beam scans the surface as in scanning electron microscopy (SEM). The surface emits secondary ions with low energy, which are subsequently accelerated and mass separated by a mass spectrometer. The surface can thus be imaged in the “light”, so to speak, of one chosen particular elemental or molecular mass. In this design, the secondary ions are accelerated backward through the lens which focuses the primary beam.

The advantage of this arrangement is that the focal length of the lens focusing the primary beam can be very short, facilitating a small spot size with optimal beam current. The secondary ion beam is deflected out of the primary beam axis above the lens arrangement. This is possible because the energy of the secondary beam is much lower than that of the primary beam. The conical shapes of the three lower electrodes offer minimal surfaces of exposure as “seen” from the analyzed sample area. This minimizes background signals and memory effects due to particles reflected and material sputtered from them.

There are two modes of operation possible: primary and secondary ions of equal or of opposite polarity. Figures A.4–A.10 show axial

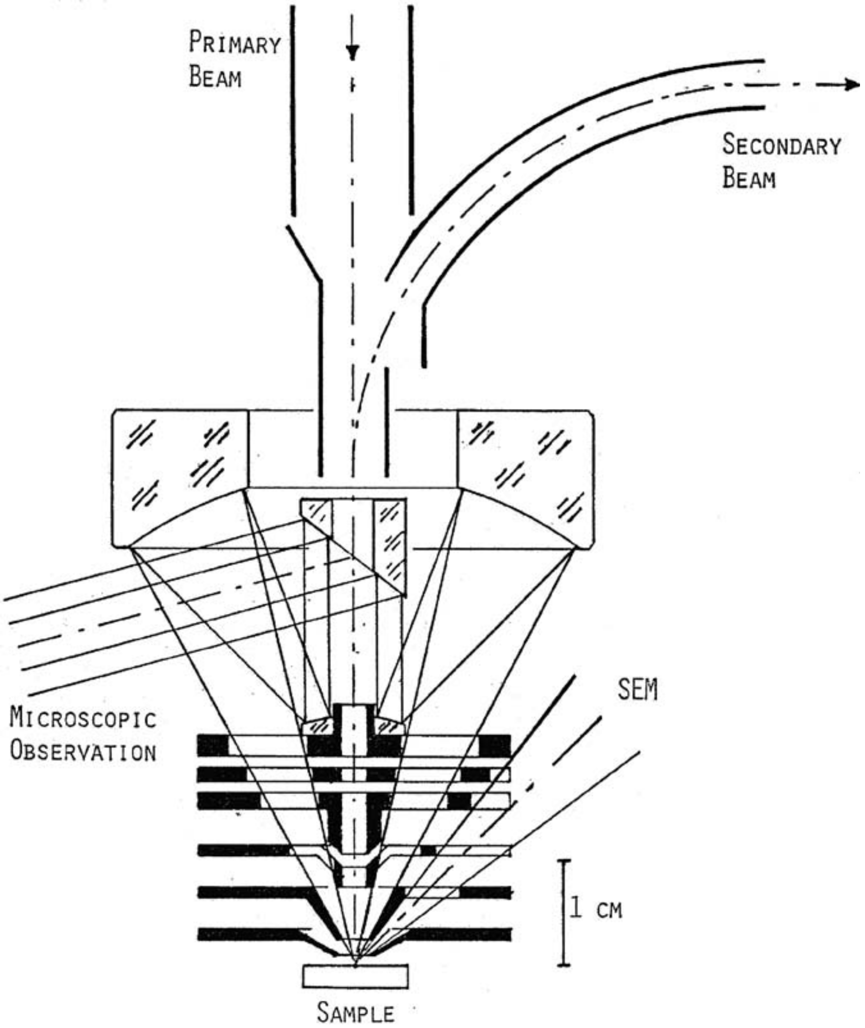

Fig. A.3. Combined electrostatic objective and emission lens with light microscope and provision for scanning electron microscopy with a high-energy electron beam (SEM)

potential distributions and ray tracings for these two modes. The conditions are chosen in such a way that a primary parallel beam enters with an energy of 3.3 keV, while the secondary beam leaves with an energy of 1 keV. In the case of equal polarity the primaries hit the surface with an energy of 2.3 keV, while in the case of opposite polarity the impact energy of the primaries is 4.3 keV. For the primary beams, Figs. A.6 and A.9, the spacings between the rays are chosen in such a

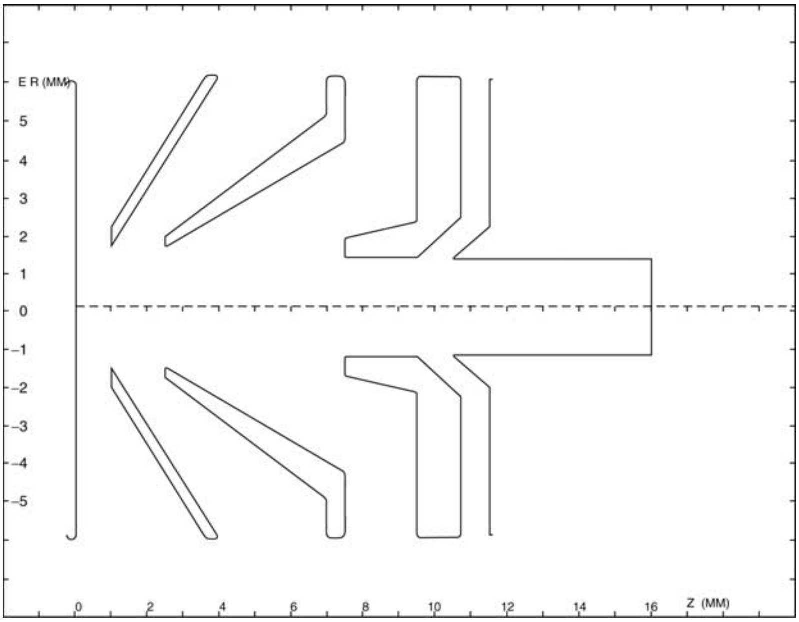

Fig. A.4. Geometry of the electrodes of the combined lens as used for the computer ray tracing

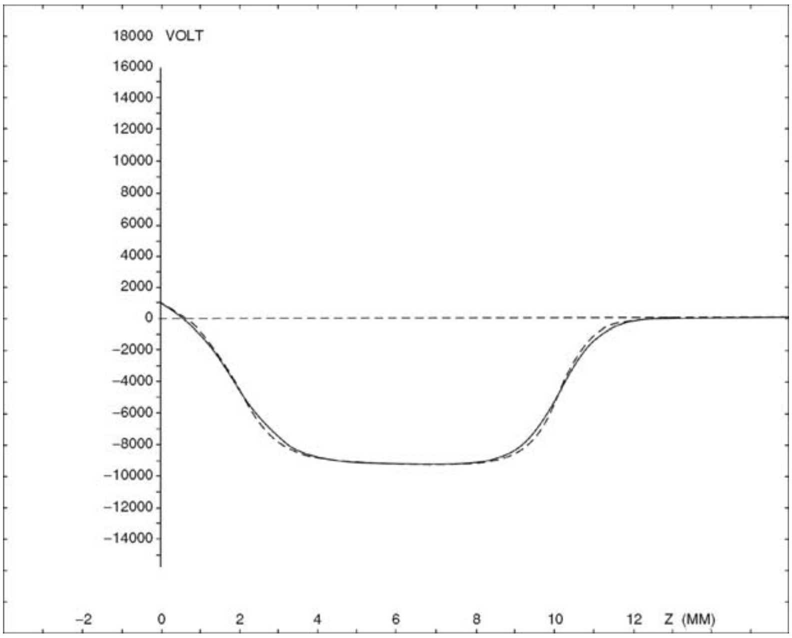

Fig. A.5. Axial potential distribution, case of equal charge polarity of primary and secondary particles

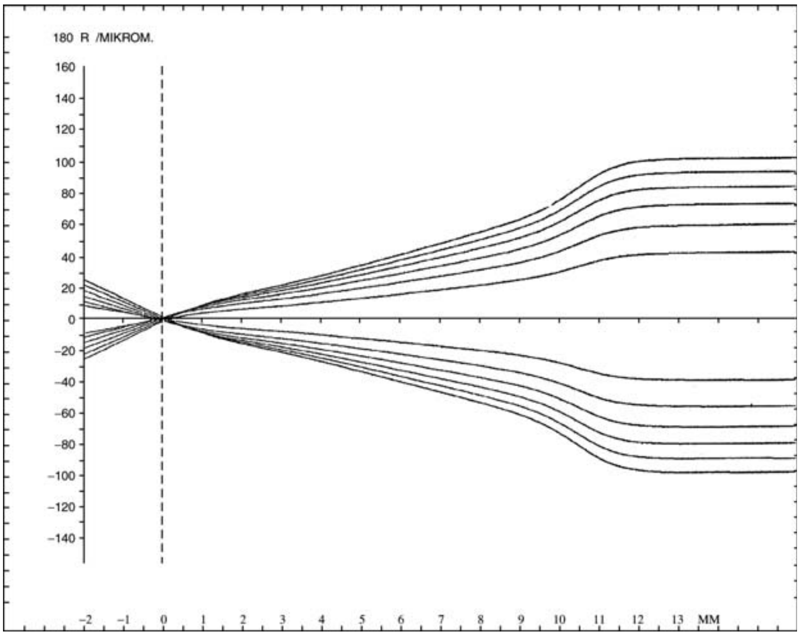

Fig. A.6. Focusing of the primary beam, case of equal charge polarity. Focal length 8 mm (radial scale different from axial one)

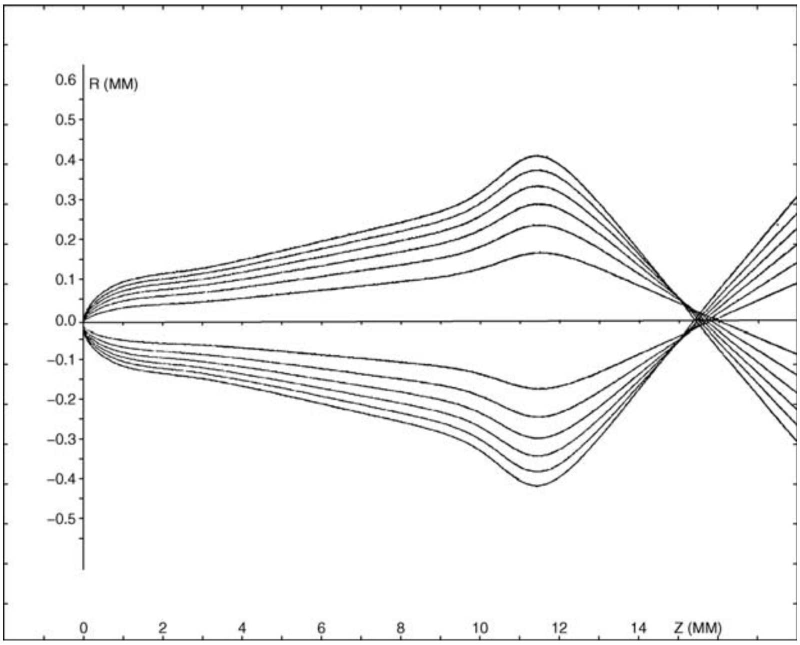

Fig. A.7. Focusing of the secondary beam, case of equal charge polarity

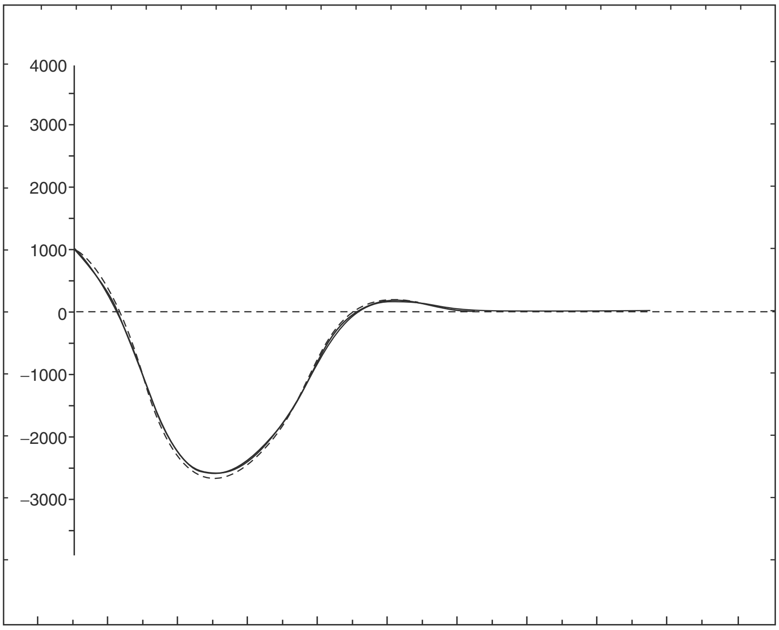

Fig. A.8. Axial potential distribution, case of opposite charge polarity of primary and secondary particles

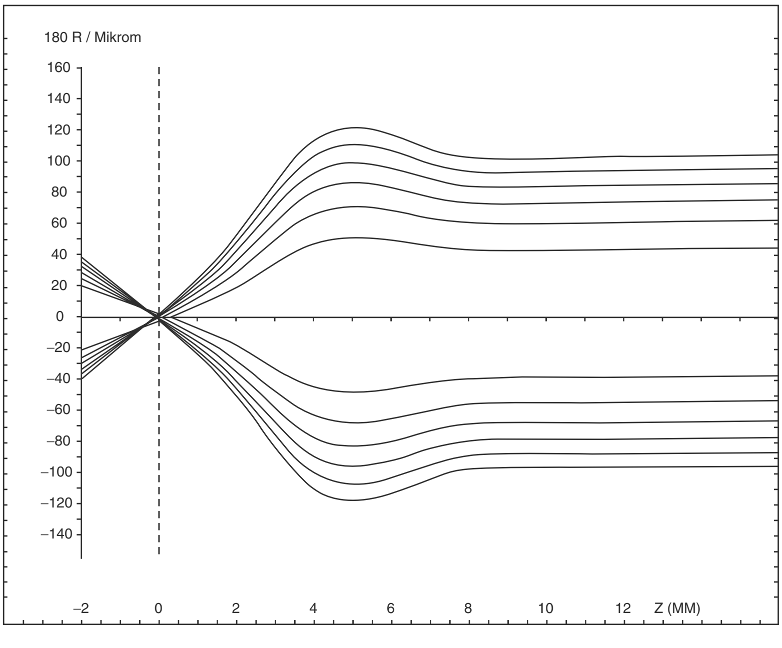

Fig. A.9. Focusing of the primary beam, case of opposite charge polarity. Focal length 5 mm

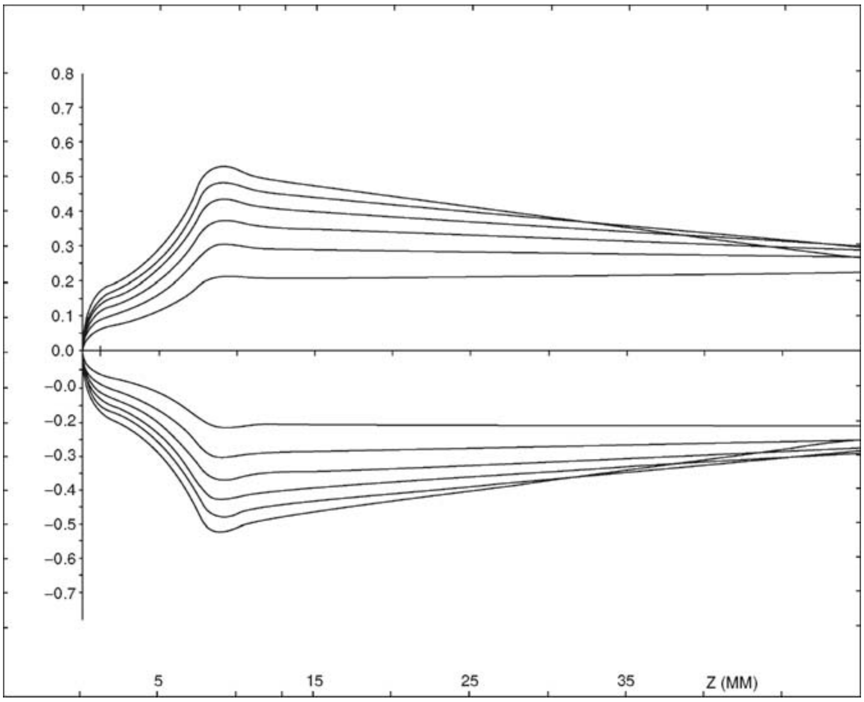

Fig. A.10. Focusing of the secondary beam, case of opposite charge polarity

way that the total beam with round cross section and uniform current density is subdivided into six portions with equal current.

The secondary beam rays shown (Figs. A.7 and A.10) are computed as starting with an initial energy of 5 eV into the half-space. The starting angles are chosen such that with a cosine emission distribution the total emission current is subdivided into six equal fractions. As secondaries not only ions can be used, but also electrons.

In the case of opposite charge polarity the secondary beam leaves the lens essentially parallel, while in the case of equal charge polarity the secondary beam forms a focus above the lens. Therefore, an einzel lens is positioned above this focus, which makes the secondary beam parallel. The effect of this einzel lens on the primary beam is very weak, because of its higher energy, and can be easily compensated by adjustment of the main lens electrode potential.

These solutions were found by trial and error, following analytical calculations with the transfer matrix method [46]. Other solutions are of course possible. The potentials applied to the electrodes scale linearly with the primary beam energy.

A.3 Dynamic Emittance Matching [47]

In a scanning microprobe with charged particles, where secondary charged particles are used to characterize the sample surface, it is important that these secondaries are transferred to the analyzer, e.g. a mass spectrometer, with optimal efficiency. An analyzer, such as a mass spectrometer with a certain mass resolution, has a certain acceptance, defined as area of the entrance slit times the solid angle accepted by the analyzer.

In order to make the sensitivity as high as possible it is important to transfer as many as possible of the secondaries into the acceptance of the analyzer.

The emittance of the secondaries is defined as the emitting area times the solid angle filled by the secondaries after acceleration. With suitable transfer optics the secondary beam emittance can be matched with the analyzer acceptance such that the largest possible fraction of the secondaries is accepted by the analyzer. With a scanning primary beam it is obvious that the instantaneous emittance of the emitting spot is much smaller than the emittance of the whole scanned area. By matching the instantaneous emittance with the analyzer acceptance a huge advantage in overall transmission of the secondaries can be realized, resulting in a corresponding gain of sensitivity.

How this can be done is shown schematically in Fig. A.11 [48]. The transfer optics images the emitting spot to the position of the entrance slit. A deflector positioned in the back-focal plane of the transfer optics, where the secondary ion beam crosses the axis, is activated in synchronism with the scanning of the primary beam, so that behind the deflector the secondary beam stays steady on axis. This “unscanning“ of the secondary beam is done in the direction normal to the drawing plane, too.

Another advantage of dynamic emittance matching is that the field of view (diameter d_1 in Fig. A.11) is independent of the analyzer acceptance.

A.4 Energy Analyzer for Parallel Beam with Coinciding Entrance and Exit Axes

Electrostatic energy analyzers such as cylindrical or spherical sector fields have a curved optic axis. With certain applications, however, a straight optic axis is desirable or even necessary.

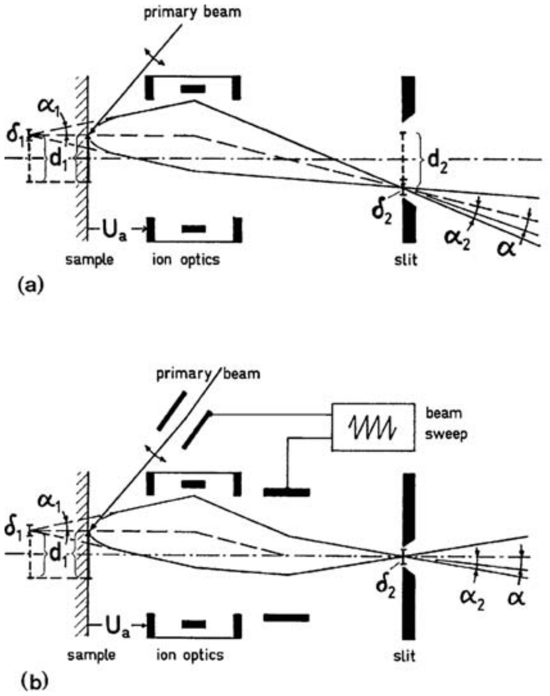

Fig. A.11. Schematic diagram of secondary ion transfer from sample to mass spectrometer, (**a**) static, (**b**) with "dynamic emittance matching". δ_1, emitting spot diameter; $\alpha_1 = \sqrt{V_1/U_a}$, maximal aperture angle of ions with initial energy eV_1 accelerated by voltage U_a; δ_2, diameter of image of δ_1 including aberration due to acceleration field [49]; d_2, diameter of image of d_1; α_2, maximal aperture angle of image δ_2

In the following, such a device is described [50]. It comprises four equal cylindrical sector fields, the first two of which deflect the beam in opposite directions, while the second equally constructed pair brings the beam back so that the exit axis coincides with the entrance axis (Fig. A.12). Between the two pairs the beam is energy dispersed so that a slit can be placed there transmitting only a certain energy bandwidth out of a beam arriving with different energies. The condition for optimal performance is that the incoming parallel beam has a focus at the position of the slit. In other words, the second sector field has to image the focus of the first sector field to the slit.

The geometry of the fringe field confinement is chosen in such a way that the effective condenser length coincides with the real one (see Chap. 5). Herzog shunts as shown in Fig. 5.1, however, are applied only at the entrance and exit of the assembly. Between the first and second

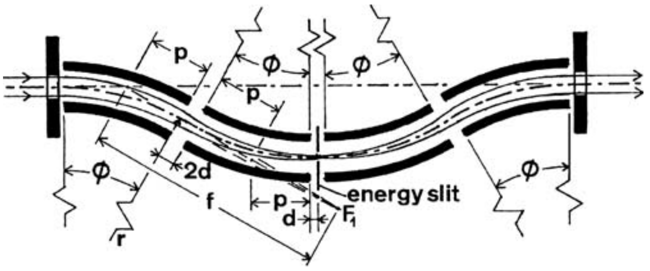

Fig. A.12. Energy analyzer consisting of four equal cylindrical sector fields, with coinciding entrance and exit axes

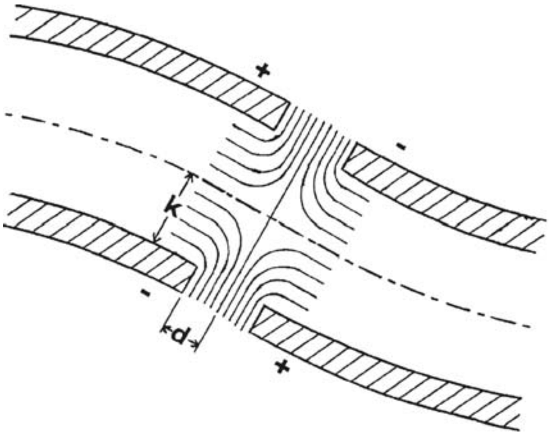

Fig. A.13. Equipotential distribution between the first and second sector field

sector fields it is not necessary to place a Herzog shunt if the distance is chosen correctly. In Fig. A.13 the equipotential distribution between these two sector fields is sketched. There is a planar equipotential surface in the middle between the sector fields, which is equivalent to a thin diaphragm with a narrow slot. Therefore, the ratio $d/k = 0.52$ (see Fig 5.2). Between the second and the third sector fields a thin diaphragm with the narrow energy slit is placed. Therefore, the ratio d/k is again 0.52.

Now, we can apply (2.24) for the imaging of the focus of the first sector field, F_1, where the incoming parallel beam would be focused in the absence of the second sector field, to the position of the energy slit. The focus F_1 is the virtual object for the second sector field. Thus, as one can see from Fig. A.12, the object distance of (2.24) becomes

$$
\begin{aligned}
-L_1 &= f - 2p - 2d, \text{ and we calculate} \\
L_2 &= \frac{2\,(p+d) - f}{2\,(p+d)/f - 2}
\end{aligned}
\tag{A.1}
$$

This image distance has to be equal to $p+d$, so that the image is focused at the distance $p+d$ from the exit principal plane of the second sector field to the position of the energy slit. Thus, we have the condition

$$p + d = \frac{2\,(p+d) - f}{2\,(p+d)/f - 2}.$$

It can be written as

$$(p+d)^2 - 2f\,(p+d) + f^2/2 = 0.$$

This can be solved for $(p+d)$ with the result

$$p + d = f\frac{\sqrt{2} \pm 1}{\sqrt{2}}.$$

By substituting $\mathrm{d} = 0.52\,\mathrm{k}$ we have

$$d = 0.52\,k = f\frac{\sqrt{2} \pm 1}{\sqrt{2}} - p,$$

and with (2.20) and (2.23)

$$\frac{\sqrt{2} \pm 1}{2\,\sin\left(\sqrt{2}\phi\right)} - \frac{1}{\sqrt{2}}\tan\left(\frac{\phi}{\sqrt{2}}\right) = 0.52\,k. \tag{A.2}$$

Solutions for this condition are easily found by trial and error. In practice, reasonable values of k/r are assumed and different values of ϕ are tried until the correct one is found. As the first term of (A.2) implies, there are two solutions, one with the plus sign and one with the minus sign.

Solutions with the minus sign are

$$
\begin{aligned}
k/r &= 0.1 \rightarrow \phi = 29.0^\circ \\
k/r &= 0.08 \rightarrow \phi = 29.5^\circ \\
k/r &= 0.06 \rightarrow \phi = 30.1^\circ
\end{aligned}
$$

In Fig. A.12 the solution with $\phi = 30^\circ$, $k/r = 0.063$ is sketched.

The corresponding solutions with the plus sign are

$$\begin{aligned} k/r &= 0.1 \rightarrow \phi = 92.4^\circ \\ k/r &= 0.08 \rightarrow \phi = 93.0^\circ \\ k/r &= 0.06 \rightarrow \phi = 93.6^\circ \end{aligned}$$

Choosing the more convenient sector angle $\phi = 90^\circ$ would result in a gap spacing of $2k = 0.35\,r$. This is too large. Therefore, one can drop the condition that the energy slit be placed at the distance d behind the second sector field. Instead a Herzog shunt, as at the entrance of the first sector field, can be placed there and the energy slit at the distance where the image of F_1 is formed. This distance can be calculated with (A.1), (2.20) and (2.23) and results, with $k = 0.1\,r$, as $L_2 = 1.56\,r$; $L_2 - p = 0.13\,r$. Such an assembly is sketched in Fig. A.14. There occurs an intermediate focus within the first sector field (at a 63.6° deflection angle), which is then imaged to the energy slit.

For the imaging ratio of some distant object to the energy slit the value of the combined focal length f^* of the first two sector fields must be known. It can be obtained from the well known formula for two lenses in series

$$\frac{1}{f^*} = \frac{1}{f_1} + \frac{1}{f_2} - \frac{D}{f_1 f_2},$$

where D is the distance between the lenses. In our case, the distance between the two principal planes has to be taken, $2\,(p + d)$, and

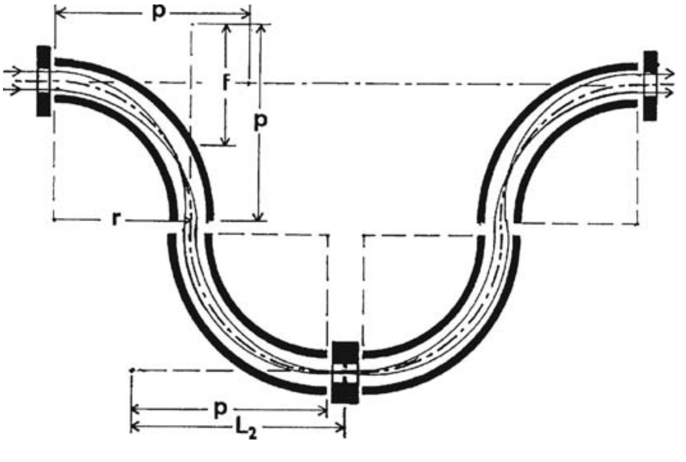

Fig. A.14. Energy analyzer consisting of four equal cylindrical sector fields with coinciding entrance and exit axes

$f_1 = f_2 = f$. Thus we have

$$\frac{r}{f^*} = 2\frac{r}{f} - 2\frac{p+d}{f^2}r = 2\frac{r}{f}\left(1 - \frac{p+d}{f}\right). \tag{A.3}$$

In the case of $\phi = 30°$ (Fig A.12) we obtain $f^* = 0.74\,r$, and with $\phi = 90°$ (A.3) yields $f^* = -0.67\,r$. The minus sign in this case does not mean that the combination acts as a diverging lens, but stems from the fact that an intermediate image is formed. For the imaging ratio from a distant object to the energy slit only the absolute value $|f| = 0.67\,r$ plays a role.

The energy dispersion of the two cases can be obtained by applying (2.18) to the second sector field. Charged particles entering the first sector field on the optic axis with energy $eV_0\,(1+\delta)$ will be deflected from the deflection center by the angle $\alpha_1 = -\lambda\delta$. The minus sign applies because of the opposite deflection in the two sector fields. This is the entrance angle α_1 in (2.18); the object distance is $L_1 = 2\,(p+d)$. We thus have

$$y_\delta = L_1\,(-\lambda\delta) + L_2\,[(1 - L_1/f)\,(-\lambda\delta) + \lambda\delta] = L_1\,(L_2/f - 1)\,\lambda\delta. \tag{A.4}$$

Now we consider the two cases $\phi = 30°$ and $\phi = 90°$. For the first case, with $L_2 = p + d$ and $k = 0.063\,r$, (A.4) yields

$$y_\delta/r = -0.43\,\lambda\delta = -0.21\,\delta, \tag{A.5}$$

and for the second case, with $k = 0.1\,r$ and $L_2 = 1.56\,r$, (A.4) yields

$$y_\delta/r = 2.23\,\lambda\delta = 1.26\,\delta. \tag{A.6}$$

The negative sign of the first case shows that the energy dispersion of the first sector field is predominant, partly counteracted by the second sector field. The positive sign of the second case indicates that in this case the energy dispersion of the second sector field is predominant. It is also much larger than in the first case, which is a consequence of the much larger sector angle ϕ.

Thus, in order to achieve a certain energy resolution, the 90° version can be scaled down, meaning a smaller radius r, as compared to the 30° version. The latter assembly, however, is slimmer. So, depending on the requirements of energy resolution and geometry, one of the two versions can be chosen. Such an energy analyzer can of course be designed not only for a parallel beam, but also for a diverging or converging beam. The parameters must then be calculated accordingly.

A.5 Elimination of Transverse Image Aberrations of Sector Fields

As described in Chap. 4, electric and magnetic sector fields form images with transverse aberrations. When such fields are not used for their dispersive properties but as mere deflectors, these aberrations can be eliminated as shown in Figs. A.15 and A.16 [43].

If the beam crossover is formed in the middle of the sector field, the second half of it cancels the aberrations, so that the virtual crossover as seen from the exit of the sector is aberration-free, and a subsequent lens will form an image of the virtual crossover free of transverse aberrations.

If a magnetic sector field is used for mass separation, a slit is placed at the crossover in the middle of the sector. An image formed by a subsequent lens will have no energy dispersion. Even the different isotopes of an element will be reunited by the lens when the separating slit is made wide enough to let them pass.

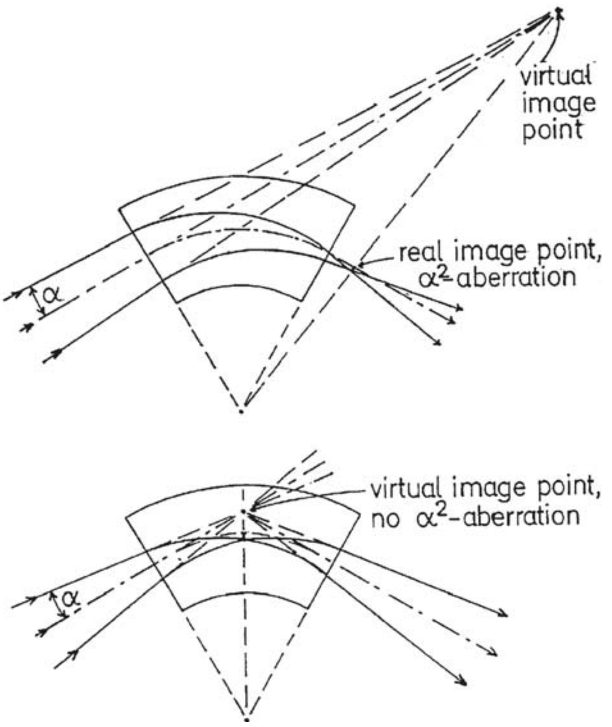

Fig. A.15. Elimination of α^2 aberration of electric or magnetic sector fields. Shown are cases where Barber's construction can be applied (also in Fig. A.16)

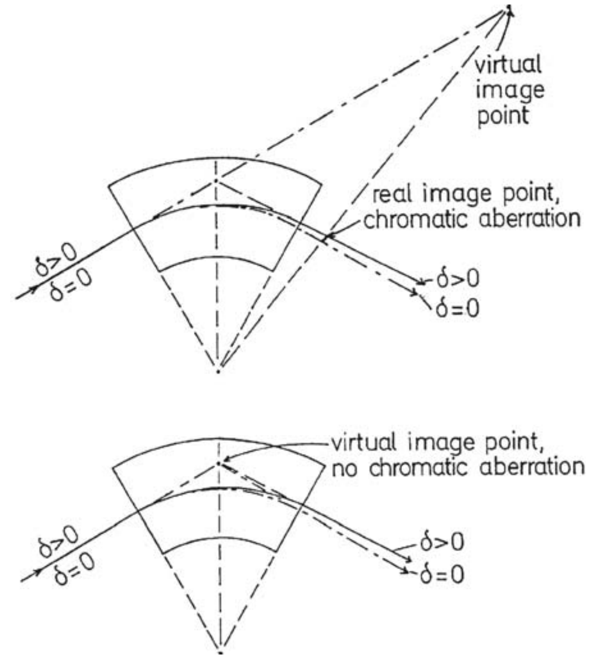

Fig. A.16. Elimination of transverse chromatic aberration of electric or magnetic sector fields

A.6 Energy-Focusing Mass Spectrometers

The simplest mass spectrometer, also the oldest historically, is a magnetic sector field. Since a magnetic field disperses not only with respect to mass but also with respect to energy (see (3.4)), its mass resolving power is limited by the energy spread of the ions to be separated. The limitation is reached, when the relative energy spread $\Delta V/V = \delta$ of the ions becomes as large as the relative mass separation $\Delta M/M = \gamma$ of a neighbouring mass, so that the two different masses can pass the exit slit.

This situation can be resolved by the addition of an electrostatic sector field which is applied in such a way that it cancels the energy dispersion of the magnetic field. An example of such a "double-focusing" (= angle and energy focusing) mass spectrometer is described in the following [51]. Figure A.17 shows a uniform magnetic sector followed by a cylindrical condenser sector with opposite deflection, both with a sector angle of $\phi = \phi_{\mathrm{e}} = 30°$ and equal radii $r = r_{\mathrm{e}} = 12\,cm$.

In order to find the distance of energy focusing, in the figure designated as L_{e}'', from the exit principal plane, we apply (2.18) to the

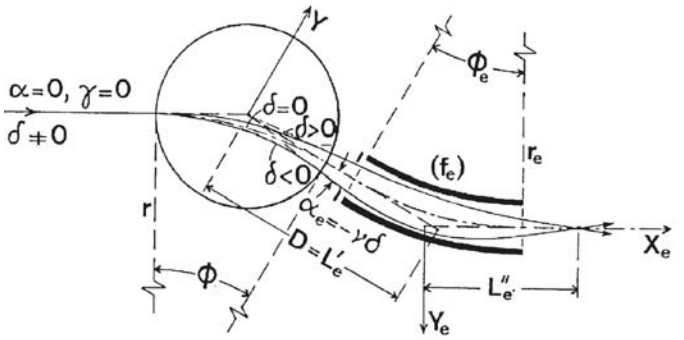

Fig. A.17. Energy focusing in a "double-focusing" mass spectrometer

electric sector field. The object distance L_1 (L'_e in the drawing) is D, the distance from the exit principal plane of the magnetic sector to the entrance principal plane of the electric sector. The entrance angle $\alpha_1 = -\nu\delta$, the energy dispersion of the magnetic sector – the minus sign because of the opposite deflection – and the exit ordinate y_e (Y_e in the drawing) must be zero for energy focusing.

Thus we have

$$D\ (-\nu\delta) + L''_\mathrm{e}\,[(1 - L_1/f_\mathrm{e})\,(-\nu\delta) + \lambda\delta] = 0.$$

From this we obtain

$$L''_\mathrm{e} = \frac{D}{D/f_\mathrm{e} + \lambda/\nu - 1}. \tag{A.7}$$

The distance D is chosen $D = 0.59r$. The other terms result with (2.20), (2.21) and (3.7): $f_\mathrm{e} = 1.05r$; $\lambda = 0.48$; $\nu = 0.25$. With these figures we obtain $L''_\mathrm{e} = 0.40\,r$.

The mass separating slit is placed at the distance L''_e. The angular focus, i.e. the image of the entrance slit, must coincide with the energy focus. Calculating backwards from the exit slit, using (2.24) and (3.8) for the two sector fields yields a negative object distance $L' = -3.25\,r$ (Fig. A.18). This means that the lens action of the two sector fields is too weak to form a real image at the exit slit of an entrance slit placed somewhere in front of the magnetic field. An einzel lens is therefore placed in front of the magnetic field, which can be tuned to image the entrance slit to the exit slit. In the direction normal to the deflection plane, the einzel lens also focuses the beam, so that no loss due to cutoff occurs in that direction between the einzel lens and the detector placed behind the exit slit.

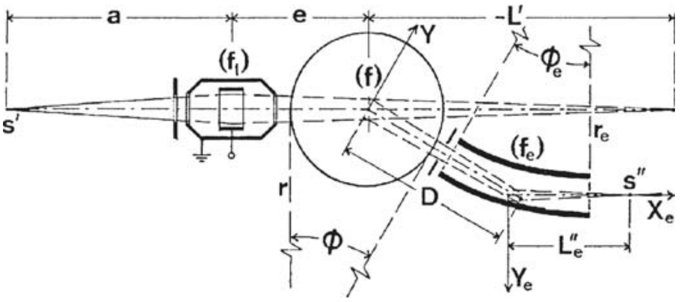

Fig. A.18. Angle focusing with the aid of an einzel lens placed in front of the magnetic sector field

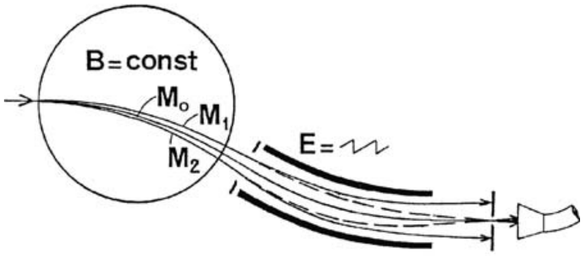

Fig. A.19. Mass scanning with constant magnetic field by ramping the electric field

Most double-focusing mass spectrometers are built with the sequence ion source – electric sector–magnetic sector–detector. The reversed sector field sequence applied here has the advantage that the mass separation occurs relatively far from the detector, thereby minimizing the background signals caused by scattered ions. Another advantage of the reversed field sequence is, that for a limited relative mass range, electric peak scanning or switching with the electric sector field is possible (Fig. A.19). Most of the elemental isotopes can therefore be scanned or switched with constant magnetic field by ramping or stepping the deflection voltage of the cylindrical condenser. Magnetic scanning is usually much slower, which is a disadvantage with certain applications.

References

1. E. Ruska, Z. Phys. **83**, 684 (1933)
2. H. Liebl, Optik **76**, 170 (1987); **83**, 129 (1989); **85**, 87 (1990)
3. V.K. Zworykin et al., *Electron Optics and the Electron Microscope* (Wiley, New York, 1945)
4. C.J. Davisson, C.I. Calbick, Phys. Rev. **38**, 585 (1931); **42**, 580 (1932)
5. H. Liebl, Optik **53**, 69 (1979); **80**, 4 (1988)
6. F.H. Read, A. Adams, J.R. Soto-Montiel, J. Phys. E Sci. Instrum. **4**, 625 (1970)
7. D. DiChio, S.V. Natali, C.E. Kuyatt, Rev. Sci. Instrum. **45**, 559 (1974)
8. E. Harting, F.H. Read, *Electrostatic Lenses* (Elsevier, Amsterdam, 1960)
9. G.F. Rempfer, J. Appl. Phys. **57**, 2385 (1985)
10. R. Herzog, Z. Phys. **89**, 447 (1934)
11. H. Matsuda, Int. J. Mass Spectrom. Ion Phys. **18**, 367 (1975)
12. E. Brüche, W. Henneberg, D.R. Patent 651,008, 1935
13. E.M. Purcell, Phys. Rev. **54**, 818 (1938)
14. H. Ewald, H. Liebl, Z. Naturforsch. **10a**, 872 (1955)
15. H. Liebl, Z. Naturforsch. **14a**, 843 (1959)
16. W.P. Poschenrieder, Int. J. Mass Spectrom. Ion Phys. **9**, 357 (1972)
17. G.-H. Oetjen, W.P. Poschenrieder, Int. J. Mass Spectrom. Ion Phys. **16**, 353 (1975)
18. M. Cotte, Ann. Physique **10**, 333 (1938)
19. R.F.K. Herzog, Acta Phys. Austriaca **4**, 413 (1950)
20. H.A.Tasman, A.J. Boerboom, Z. Naturforsch. **14a**, 121 (1959)
21. A.J. Boerboom, H.A. Tasman, H. Wachsmuth, Z. Naturforsch. **14a**, 816 (1959)
22. H. Wachsmuth, A.J. Boerboom, H.A. Tasman, Z. Naturforsch. **14a**, 818 (1959)
23. H.A. Tasman, A.J. Boerboom, H. Wachsmuth, Z. Naturforsch. **14a**, 822 (1959); **17a**, 362 (1962)
24. H.O.W. Richardson, Proc. Phys. Soc. (Lond.) **59**, 791 (1947)
25. J.S. O'Connell, Rev. Sci. Instrum. **32**, 1314 (1961)
26. H. Liebl, J. Appl. Phys. **38**, 5277 (1967)
27. F.G. Ruedenauer, Int. J. Mass. Spectrom. Ion Phys. **4**, 181 (1970); **4**, 195 (1970)
28. H. Ewald, H. Liebl, Z. Naturforsch. **12a**, 28 (1957)
29. H. Wollnik, Nucl. Instrum. Methods **34**, 213 (1965)
30. H. Wollnik, E. Ewald, Nucl. Instrum. Methods **36**, 93 (1965)
31. H. Wollnik, Nucl. Instrum. Methods **52**, 250 (1967); **59**, 277 (1968)

32. H. Matsuda, Nucl. Instrum. Methods **91**, 637 (1971)
33. H. Liebl, Nucl. Instrum. Methods Phys. Res. A **292**, 537 (1990)
34. H. Wollnik, T. Matsuo, H. Matsuda, Nucl. Instrum. Methods **102**, 13 (1972)
35. H. Liebl. Int. J. Mass. Spectrom. Ion Phys. **22**, 203 (1976)
36. L.A. König, H. Hintenberger, Z. Naturforsch. **10a**, 877 (1955); **12a**, 377 (1957)
37. H. Hintenberger, L.A. König, Z. Naturforsch. **11a**, 1039 (1956); **12a**, 140 (1957)
38. H. Liebl, H. Ewald, Z. Naturforsch. **12a**, 538 (1957)
39. R. Persson, Ark. Fys. **3**, 31 (1951)
40. H. Wollnik, Nucl. Instrum. Methods **53**, 197 (1967)
41. H. Matsuda, H. Wollnik, Nucl. Instrum. Methods **77**, 40 (1970); **77**, 283 (1970)
42. R. Herzog, Phys. Z. **41**, 18 (1940)
43. H. Liebl, B. Senftinger, Ultramicroscopy **36**, 91 (1991)
44. D.A. Dahl, J.E. Delmore, *Program SIMION*, Idaho Natural Engineering Laboratory
45. H. Liebl, H. Weiss, Scanning Electron Microsc. **3**, 793 (1986)
46. H. Liebl, Int. J. Mass. Spectrom. Ion Phys. **46**, 511 (1983)
47. H. Liebl, U.S. Patent 3,517,191, filed 11 Oct 1965
48. H. Liebl, Adv. Opt. Electron Microsc. **11**, 101 (1989)
49. H. Liebl, Optik **80**, 4 (1988)
50. H. Liebl, B.V. King, *Secondary Ion Mass Spectometry SIMS VIII*, ed. by A. Benninghoven et al. (Wiley, New York, 1992), p. 215
51. H. Liebl, Nucl. Instrum. Methods Phys. Res. A **258**, 323 (1987)

Index

About the Author

Helmut Liebl – born in 1927 in Bavaria – studied physics at the Technical University of Munich, and was awarded a diploma in 1953 and a doctorate in 1956. After three years as Wissenschaftlicher Assistent at the Technical University of Munich, he joined the Geophysics Corp. of America (GCA), Bedford, Mass., in 1959. In 1964 he became Senior Scientist at the Hasler Research Center of Applied Research Laboratories (ARL), Goleta, California. In 1968 he returned to Germany, where he worked with the Surface Physics Division of the Max Planck Institute for Plasma Physics in Garching/Munich until his retirement.

Starting with his doctoral thesis, his ongoing work was theoretically and experimentally mostly in the field of ion optics and its application to mass spectrometry.

While working with ARL he designed and built the first scanning ion microprobe mass analyzer with a lateral resolution of less than two microns [26]. He is author and co-author of over 80 scientific papers and 20 patents.